Nonpremixed Flame in a Counterflow Under Electric Fields

Dissertation by

Dae Geun Park

In Partial Fulfillment of the Requirements

For the Degree of

Doctor of Philosophy

King Abdullah University of Science and Technology

Thuwal, Kingdom of Saudi Arabia

The dissertation of Dae Geun Park is approved by the examination committee.

Committee Chairperson William L. Roberts

Committee Member Hong G. Im

Committee Member Mani Sarathy

Committee Member Derek Dunn-Rankin

Committee Member Suk Ho Chung

Committee Member Min Suk Cha

ABSTRACT

Nonpremixed flame in a counterflow under electric field

Dae Geun Park

Electrically assisted combustion has been studied in order to control or improve flame characteristics, and emphasizing efficiency and emission regulation. Many phenomenological observations have been reported on the positive impact of electric fields on flame, however there is a lack of detailed physical mechanisms for interpreting these. To clarify the effects of electric fields on flame, I have investigated flame structure, soot formation, and flow field with ionic wind electrical current responses in nonpremixed counterflow flames. The effects of direct current (DC) electric field on flame movement and flow field was also demonstrated in premixed Bunsen flames.

When a DC electric field was applied to a lower nozzle, the flames moved toward the cathode side due to Lorentz force action on the positive ions, soot particles simultaneously disappeared completely and laser diagnostics was used to identify the results from the soot particles. To understand the effects of an electric field on flames, flow visualization was performed by Mie scattering to check the ionic wind effect, which is considered to play an important role in electric field assisted combustion. Results showed a bidirectional ionic wind, with a double-stagnant flow configuration, which blew from the flame (ionic source) toward both the cathode and the anode. This implies

that the electric field affects strain rate and the axial location of stoichiometry, important factors in maintaining nonpremixed counterflow flames; thus, soot formation of the counterflow flame can also be affected by the electric field. In a test of premixed Bunsen flames having parallel electrodes, flame movement toward the cathode and bidirectional ionic wind were observed. Using PIV measurement it was found that a created radial velocity caused by positive ions (i.e. toward a cathode), was much faster than the velocity toward the anode. Even in a study of alternating current (AC) electric fields, bidirectional ionic wind could be observed, regardless of applied frequencies. Therefore, the effect of ionic wind cannot be considered negligible under both DC and AC electric fields. Detailed explanations for electrical current, flame behavior, and flow characteristics under various conditions are discussed herein.

ACKNOWLEDGEMENTS

I wish to express my gratitude to my friends and my professors at KAUST. With their help, my education, experience, and my attitudes have been greatly expanded. I know that my years here will be among the most memorable of my life. My two mentors and supervisors, Professor Suk Ho Chung and Professor Min Suk Cha have been particularly important to my academic career. Professor Chung, who permitted me to study and conduct research at KAUST, has offered invaluable advice and support throughout my studies here. Under his guidance, my methods and my studies in combustion research have been greatly enhanced. I also offer my sincere gratitude to Professor Cha. As a member of his research group I was guided from first to last, with a scientific approach to my work and presentation skills. He has also been an understanding and perceptive mentor in my personal life; his influence on my philosophy--as well as my research--has been tremendous. I cannot fully express my appreciation to Professors Chung and Cha; they will always have my utmost gratitude and respect.

I would also like to thank my committee members, Professor William L. Roberts, Professor Hong G. Im, Professor Mani Sarathy, and Professor Derek Dunn-Rankin; their time and efforts in my behalf are greatly appreciated.

Yuan Xiong and Jie Han came to KAUST at almost same time as I. They helped me adapt to new circumstances, and collaborated in my English studies and research; their friendship and cooperation has been an invaluable addition to my academic life. My thanks also to Tran Manh Vu who shared his time to discuss research and life at our

former university (PKNU) in South Korea. I was very pleased to meet him again here at KAUST and to continue our friendship.

My appreciation extends to my friends and colleagues, Wonsik Song, Yujeong Kim, Hyunwoo Park, Ahmad Hamdan, Manoj Kumar Reddy, Deanna Lacoste, Xuming Zhang, Kristians Cernevics, Ossama Mannaa, Saeed Al-Noman, Mohamed Anwar Ismail, Hafiz Muhammad Fahid Amin, Wang Yu, and Hatsari Mitsudharmadi, all of whom helped me so much during the past five years. The support staff at CCRC—especially Issam Alkhesho and Chongchong Li—were most helpful in the purchase and setup of experimental devices.

To my parents and parents-in-law I offer my lifelong gratitude for their support and encouragement and for their constant positive reinforcement. Finally, without the love and sacrifice of my wife and best friend Suyeon Kang, I could not have succeeded. Words cannot express my gratitude to her and my thanks for our two sons Junwoo Park and dda-dda (2^{nd} baby nickname).

TABLE OF CONTENTS

LIST OF FIGURES

LIST OF TABLES

Chapter 1

INTRODUCTION

1.1 Motivation and necessity for research

In the last several decades, environmental impact, including global warming, has emerged as a serious issue worldwide [1], making technical development of effective emission control and efficient use of resources of central concern for combustion systems. Although renewable energy such as solar, water, and wind, has been widely investigated [2-5], it is not expected that a combustion paradigm using fossil fuels can be achieved expeditiously. This is because the most widely used conventional systems, such as power plants, internal combustion engines, and rockets, are developed and operated based on the combustion of fossil fuels. For these reasons, intensive research and study of new technologies based on combustion like biofuels [6], syngas combustion [7], advanced engine combustion [8], and plasma or electrically assisted combustion [9-12] is still being conducted to improve combustion characteristics.

Electrically assisted combustion has been extensively investigated, with the focus on controlling the properties and behavior of both premixed and non-premixed flames; Weinberg and his colleagues [13-23] conducted substantial research in this area in the

1960's. The utilization of electric fields for combustion has been realized, resulting in many phenomenological observations, mainly concerning soot emission [24-40], flame propagation speed [41-53], and flame stability [54-65] in various configurations of burner setups, such as coflow, counterflow, Mckenna burners, constant volume combustion chambers, etc. Recent advances in measurement and modeling have revealed more details about the characteristics of ion chemistry and the relationships of flame and flow behavior under the influence of electric fields. As a result, the nature of ionic winds [17, 21, 66-74], and the characteristics of ion currents with bias voltage and its applications [75-81], can now be understood in detail; and extended numerical simulations with detailed ion chemistry and additional body force are possible by solving the electric potential [56, 82-86]. Even though there have been many phenomenological results showing reduced soot emission, enhanced propagation speed, and improved flame stability using electric fields, there are still gaps between the observations and the physicochemical mechanism behind them, due to the complicated kinetic and transport coupling between electric fields and flames.

For these reasons, electrically assisted combustion should be continuously studied in order to understand the fundamental physicochemical mechanisms which explain the existing phenomena of interest and the supporting design-based technical approaches for real applications. To cope with this necessity, the effects of electric fields on nonpremixed flames are investigated in this thesis.

A canonical counterflow burner was selected as a platform for this study, based on its well-defined geometry and in-depth understanding of fundamental aspects of flames.

When external voltage is applied, a gap between the nozzles can reasonably be expected in a counterflow burner with a grounded counterpart and a uniform electric field; another reason for well-defined experimental data in modeling research. Both direct current (DC) and alternating current (AC) were considered as sources of the electric field.

1.2 Interactions between flame and electric fields

Ionization processes for a generation of electrically charged species, such as positive and negative ions and electrons, can be categorized as follows: (a) ionization by collision, (b) electron transfer, (c) ionization by transfer of excitation energy, and (d) chemi-ionization such as equations (1.1) to (1.6) [12] :

(a) Ionization by collision

$$A + B \rightarrow A^+ + B + e^- \quad (1.1)$$

$$A + e^- \rightarrow A^+ + e^- + e^- \quad (1.2)$$

(b) Electron transfer

$$A + B \rightarrow A^+ + B^- \quad (1.3)$$

(c) Ionization by transfer of excitation energy

$$A + B^* \rightarrow A^+ + B + e^- \quad (1.4)$$

(d) Chemi-ionization

$$A + B \rightarrow C^+ + D + e^- \quad (1.5)$$

$$A + B \rightarrow C^+ + D^- \quad (1.6)$$

Among the processes above, the chemi-ionization process is a well-known ionization source of hydrocarbon flames, which produces positive ions (H_3O^+, $C_3H_3^+$, CH_3^+, CHO^+), negative ions (O_2^-, OH^-, O^-, CHO_2^-, CHO_3^-, CO_3^-), and electrons [87-89]. Calcote discovered that one of the most important reactions of chemi-ionization is an initiating step, as described in Eq.1.7 [90].

$$CH + O \rightarrow CHO^+ + e^- \quad (1.7)$$

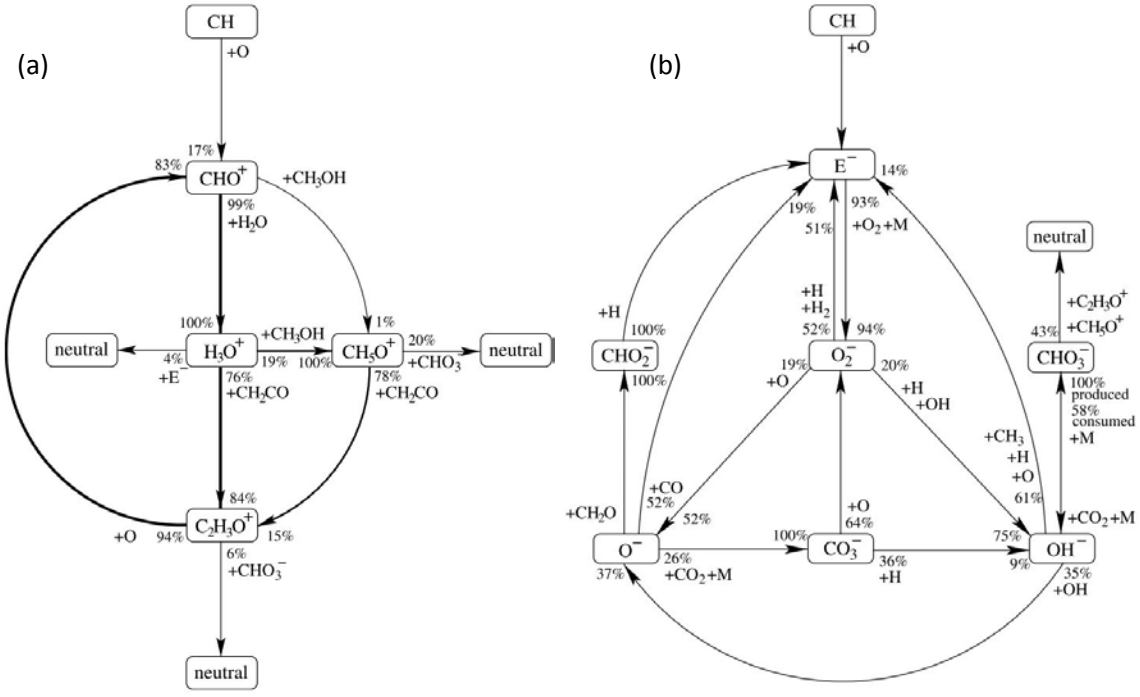

Figure 1.1 Global reaction flows for (a) positive and (b) negative ions from Prager *et al*. [91].

To illustrate an overview of the chemi-ionization reaction, global reaction flows for positive and negative charges were quoted from a previous work by Prager *et al.* [91] in Figs 1.1a and b, respectively. A detailed transport model and an elementary reaction mechanism were implemented to provide a chemical kinetic model for the chemi-ionization process occurring in a flame zone. Even though H_3O^+ is known to be the most abundant positive ion in a hydrocarbon flame, the CHO^+ ion is its precursor. Meanwhile, in the chemical pathway of the negative charge in Fig. 1.1 (b), an electron, born during the initiation step in Eq. 1.7, is described as an essential part of the entire process, combining with O_2 to form O_2^-. Thus, it can be speculated that neither hydrogen flame (H_2), nor carbon monoxide flame (CO), can produce ions, since CH is not an intermediate species during the oxidation of these species.

When an electric field is applied to a flame, its various effects on the flame can be hypothesized: 1) a modified transport caused by ionic wind [42, 74], 2) a chemical kinetic effect via ions affected by the electric field [50, 53], and 3) a thermal effect due to deposited energy from the electric field [92]. The microscopic, physical phenomenon (mostly understood and accepted) occurring in a flame with an electric field is that a movement of charged species is caused by the Lorentz force, and eventually this microscopic physics leads to a modification in a bulk flow motion called *ionic wind*. As a result, the positive ions move toward a cathode (lower potential electrode), while the negative ions are transported toward an anode (higher potential electrode), with a drift velocity expressed as μE, where μ is ion mobility and E is a local field intensity. In this process, a momentum transfer from energized charged species to neutral molecules

occurs, so that ionic wind can be generated. The chemical kinetic and thermal effects must be supported by rigorous research to prove their existence and effectiveness.

In the reaction zone, a charge balance is valid, so that $n_+ = n_- + n_e$, where n is a number density and +, –, and e is positive ions, negative ions, and electrons, respectively. Therefore, positive ions always outnumber negative ions in the reaction zone of hydrocarbon flame. When external electric fields are applied to the flames, they tend to move toward the cathode side due to the Lorentz force. The effects of the electric field on flame behaviors has been studied with various types of flame, including the effects of ionic wind [16, 17, 21, 57, 66, 68-72, 74-76, 82, 83, 85, 93-100]. Because of abundant positive ions in the hydrocarbon flame, it has been speculated that positive ions play a more important role in the interaction between a flame and an electric field than do negative ions. Recently however, some literature has reported that negative ions cannot be neglected in an explanation of the effect of electric field on a flame; it can also be a significant factor for increasing number density of negative ions due to electron attachment [68, 69]. Experimental evidence for the significant role of negative ions will be discussed in the present study.

1.3 Utilization of electric fields on various flames

Various flames, such as premixed or nonpremixed flames and laminar or turbulent flames, have been investigated in different burner configurations using DC or AC electric fields. The results have been improved flame characteristics such as reduction in soot

emission, enhanced flame propagation speeds, and enlarged flame stability limits. The detailed phenomenological results will be discussed in the following.

1.3.1 Reduced soot emission

Soot formation in a diffusion flame mode is inevitable, caused by a pyrolysis of the fuel component and soot emission from the combustion system; it implies pollution of the atmosphere as well as a loss of combustion efficiency. Soot emission in diesel engines is a typical example of the source of regulated particulate matter; and after-treatment technology, such as diesel particulate filters (DPF), is the most viable solution for the present, even though combustion control can help to reduce the amount of emissions. In this regard, development of a new technique to reduce soot formation in flames is not only of interest in fundamental research but it is also expected to extend a choice of soot control methods for practical applications.

It has been reported that soot formation processes could be affected by applying electric fields or electrical discharges, resulting in effective suppression of soot formation in much of the literature. Research activity in soot control using electric fields is summarized in Table 1.1.

Table 1.1 Literature studies for sooting flame with electric fields

	DC	AC
Nonpremixed flame	Place and Weinberg [35, 36] Hardesty and Weinberg [37] Xie *et al.* [33] Kono *et al.* [26, 27] Ohisa *et al.* [29] Vatazhin *et al.* [31]	Saito *et al.* [30, 38] Cha *et al.* [25] Xie *et al.* [33] Kono *et al.* [26, 27] Ohisa *et al.* [29]
Premixed flame	Wang *et al.* [32] Zake *et al.* [39] Eugene *et al.* [40]	

Cha *et al.*[25] reported a novel idea for controlling soot formation in a coflow nonpremixed jet flame using a dielectric barrier discharge (DBD), as illustrated in Fig. 1.2. Based on the yellow luminosity in a jet flame, caused by a thermal radiation from soot particles, Fig. 1.2 clearly shows the significant removal of soot particles with an increase in applied voltage. In this study, two regimes were divided by measuring electric power: 1) electrostatic regime for $V_a \leq 12.0$ kV and 2) plasma regime for $V_a > 12.0$kV, where V_a is applied voltage. A decrease in flame length and an intensity of yellow luminosity with increased voltage was observed. In the electrostatic regime, soot particles were deposited into an electrode or they leaked out due to the electrostatic collection of charged particles. Interestingly, no soot particles formed in the plasma regime; electron impact reactions might have an important role in the formation of PAHs—there were no PAHs formations in the plasma regime.

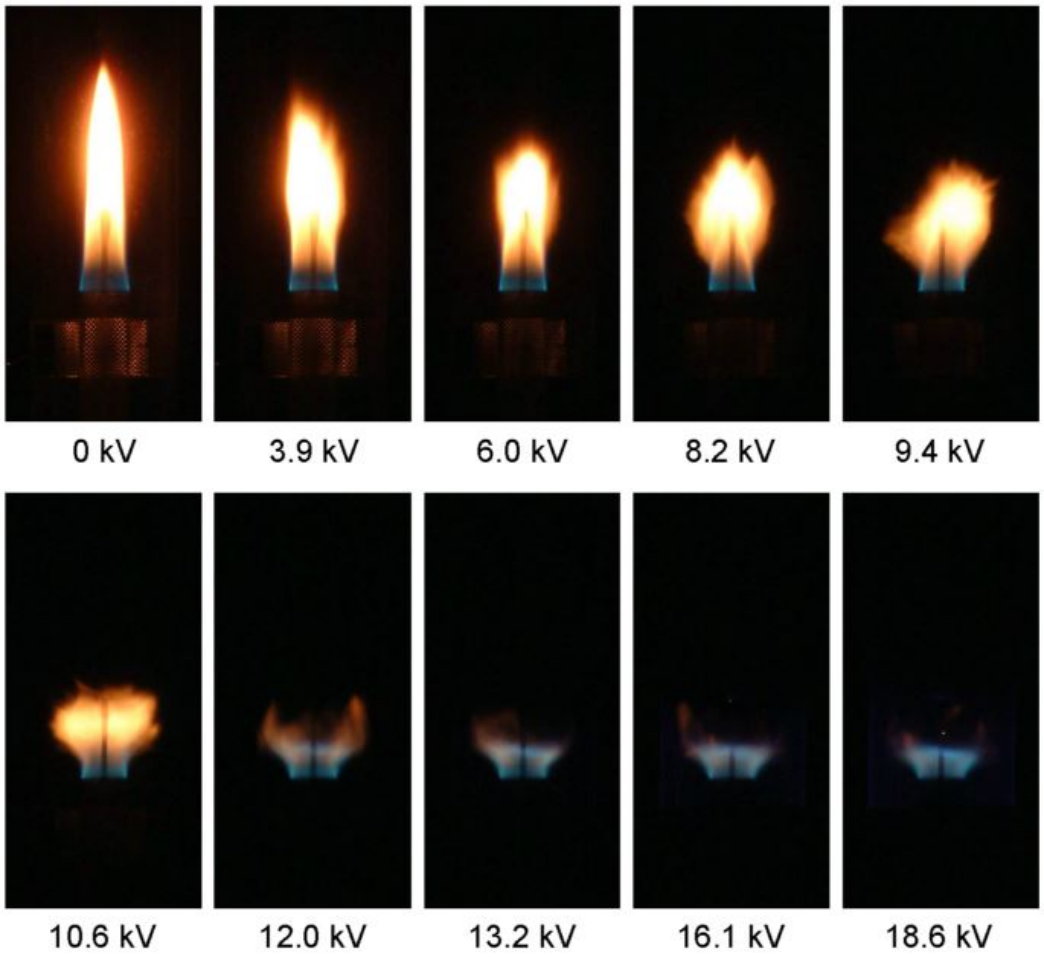

Figure 1.2 Behavior of sooting flame in coflow jet with applied voltages from Cha *et. al*. [25].

Place and Weinberg [35, 36] and Hardesty and Weinberg [37] analyzed the size of soot particles in hydrocarbon flames with a DC electric field using a transmission electron microscopy (TEM). The size of the soot particles decreased with increased applied voltage as compared to those with no electric field. It was reported that soot particles were positively and negatively charged; then the charged particles were moved toward the respective electrodes (depending on polarity by Lorentz forces), resulting in

soot deposition on the electrode surfaces. As a result, particle size was decreased due to the reduced residence time of soot particles in the pyrolysis zone.

Kono *et al.* [27] investigated a variation in the yellow luminosity of acetylene premixed and nonpremixed flames, applying DC and AC electric fields in a counterflow and a jet burner. The luminosity increased or decreased depending on the flow rate of a fuel in nonpremixed flames and on an equivalence ratio and a flow rate of a mixture in the premixed flames. Xie *et. al* [33] measured the intensity of flame luminosity and spatially resolved soot volume fraction using an intensified CCD camera with a 450nm-filter (bandwidth 100nm), and a laser scattering and extinction method, respectively. They demonstrated that soot volume fraction decreased at a high voltage, whereas it was increased at low voltage. A solid understanding of the fundamentals is required to explain the detailed physicochemical mechanisms which support such observations.

Using the same fuel (acetylene), as in the work of Kono *et al.* [27], Saito *et al.* [30, 38] determined that soot emissions decreased consistently with increased electric fields in both positive and negative applied voltages with nonpremixed jet flames.They explained that ionic wind, blowing to a low potential electrode, enhanced the mixing of fuel with surrounding air, resulting in soot reduction caused by air entrainment promoted by the ionic wind. These results were controversial to the work of Kono *et al.* [27], and Xie *et al.* [33]; and a detailed explaination for those discrepancies among the studies is still unclear. In this regard, soot formation and oxidation characteristics in a DC for counterflow nonpremixed ethylene flames was investigated to clarify the effect of DC. Detailed results are discussed in Chapters 3 and 4.

1.3.2 Enhanced flame propagation speed

Flame propagation speed is a typical parameter with which to characterize a premixed flame, it is also important for predicting the rate of fuel consumption in a combustor. Flame propagation speed is affected by the laminar burning velocity of a given mixture, flow strain, curvature of a flame front, heat loss, and a mixture fraction gradient in a laminar flame. For this reason, it is difficult to control this basic flame characteristic parameter for a given combustor geometry, and without this control the mixture composition is changed. For several decades, the feasibility of applying electric fields has been investigated to find a technical method which can control flame propagation speed. Table 1.2 presents a list of previous work on DC and AC fields.

Marcum and Ganguly reported the effects of pulsed and continuous DC electric fields on premixed-air conical flames [43]. A wrinkled laminar flame was found under the electric fields, resulting in a substantial increase in flame propagation speed. Based on their hypothesis, that thermal-diffusive instability should be responsible for the flame wrinkling observed when the global Lewis number is less than unity, they further speculated that the applied electric field could modify transport properties, leading to increased mass diffusivities and thereby lowering the Lewis number. The modification of the mass transport could be attributed to ionic wind caused by positive ions in a flame, which blew toward a low electric potential electrode (nozzle), as stated in their hypothesis.

Table 1.2 Literature studies for propagating flame with electric fields

DC	AC
Guenault and Wheeler [48, 49] (CVCC & tube) Bowser and Weinberg [14] (Flat flame) Marcum and Ganguly [43] (Bunsen flame) Jaggers and Von Engel [50] Van den Boom *et al.* [53]	Won *et al.*[46, 47] (lifted flame) Kim *et al.*[51] (wire flame) Lim *et al.*[52] (wire flame) Cha and Lee [42] (CVCC) Jaggers and Von Engel [50]

Won *et al.* investigated the propagation speeds of edge flames in a coflow jet configuration applying DC and AC high voltage to a jet nozzle [47]. Flame displacement speeds were corrected with respect to cold flow velocity (estimated by the jet theory using a similarity solution), so that edge flame propagation speeds could be reported. As a result, enhancement of the propagation speed was discovered in both DC and AC electric fields; and they suggested that the combined effects of ionic wind, chemical kinetics, and transport properties could be responsible for the observation. There was no clear evidence to support specific physicochemical mechanisms.

Jaggers and Von Engel suggested the importance of chemical kinetic effects caused by electric fields. They studied methane-air and ethylene-air premixed flames in a vertical convection free tube using DC and AC electric fields on burning velocity. Increased burning velocity could also be observed in all types of electric fields. The results were explained by the effect of chemical kinetics due to the higher vibrational

states of molecules and radicals during collisions. However, there were no findings to support the hypothesis of increasing reaction rates with electric fields.

In a study from Cha and Lee [42] on outwardly propagating flame in a constant-volume combustion chamber (CVCC), propagation speeds were found to increase with the application of AC electric fields. A flame surface in methane/air mixtures had a cracked structure, as compared to a surface without electric fields (Fig. 1.3). They proposed a possible mechanism to explain the electrically-induced instability: a hydrodynamic instability due to ionic wind and thermo-diffusive instability through the modification of mass diffusivity.

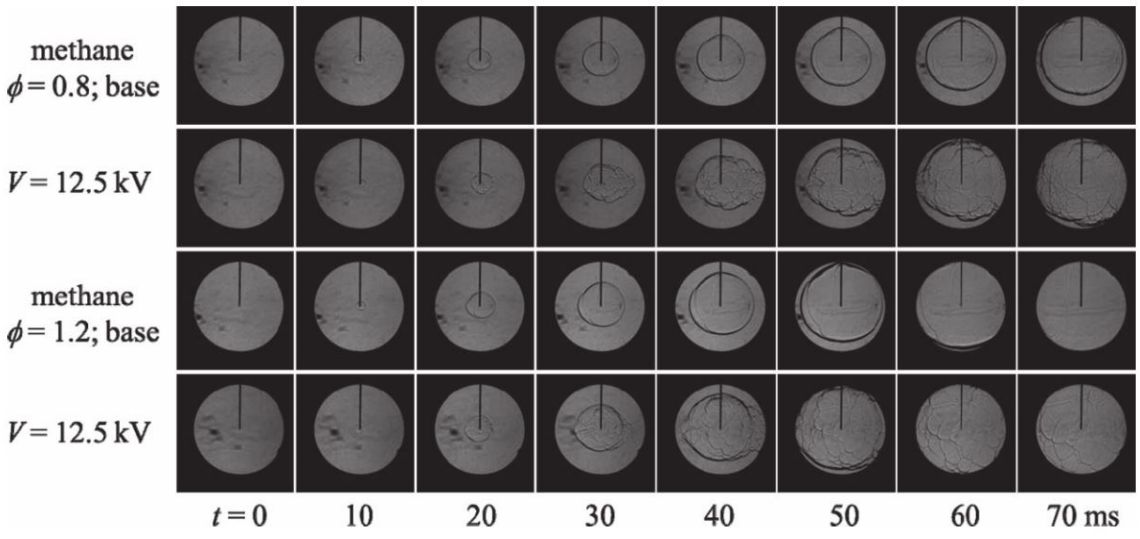

Figure 1.3 Effects of electric fields on propagation speed in CVCC by Cha *et al.* [42].

Studies of enhanced flame propagation speeds with an electric field can be found in much of the literature; however there is a lack of clarification for the phenomena. To understand the mechanisms that supporting these results, each effect--including ionic wind, ion chemistry and transport properties-- should be studied at a fundamental level.

1.3.3 Flame stabilization

Flame instabilities caused by heat loss, thermal expansion, and preferential diffusion can lead to deterioration in combustion efficiency and safety issues in the combustion system [101]. To minimize flame instabilities and broaden the limits to stable operation, approaches to control flame instabilities using electric fields have been studied extensively for both nonpremixed and premixed flames, as summarized in Table 1.3.

Table 1.3 Literature studies for stabilized flame with electric fields

	DC	AC
Nonpremixed flame	Memdouh *et al.* [56] Calcote and Pease [60] Noorani and Holmes [61]	Kim *et al.* [62] Lee *et al.* [59] Ryu *et al.* [63]
Premixed flame	Ata *et al.* [64]	Kim *et al.* [65, 68]

In nonpremixed laminar jet flames, stability of the flames under an AC electric field was investigated by Kim *et al.* [62], emphasizing the extension of blowout and blowoff limits. A stable flame regime was significantly extended in terms of its jet velocity, demonstrating the decreased velocity range of lifted flames with greater applied voltage, as shown in Fig. 1.3. Memdouh *et al.* [56] performed a direct numerical simulation to investigate flame stability, applying DC electric fields in nonpremixed laminar jet flames. They found that enhanced flame stability could be attributed to ionic wind, which relocated the base of a lifted flame toward a nozzle upstream. Because no model is available for the chemical kinetic and thermal effects of electric fields on a flame (partly due to lack of scientifically sound evidence to support those two effects), a modeling approach implementing ion chemistry and electric body force is one of the more feasible methods in a numerical study.

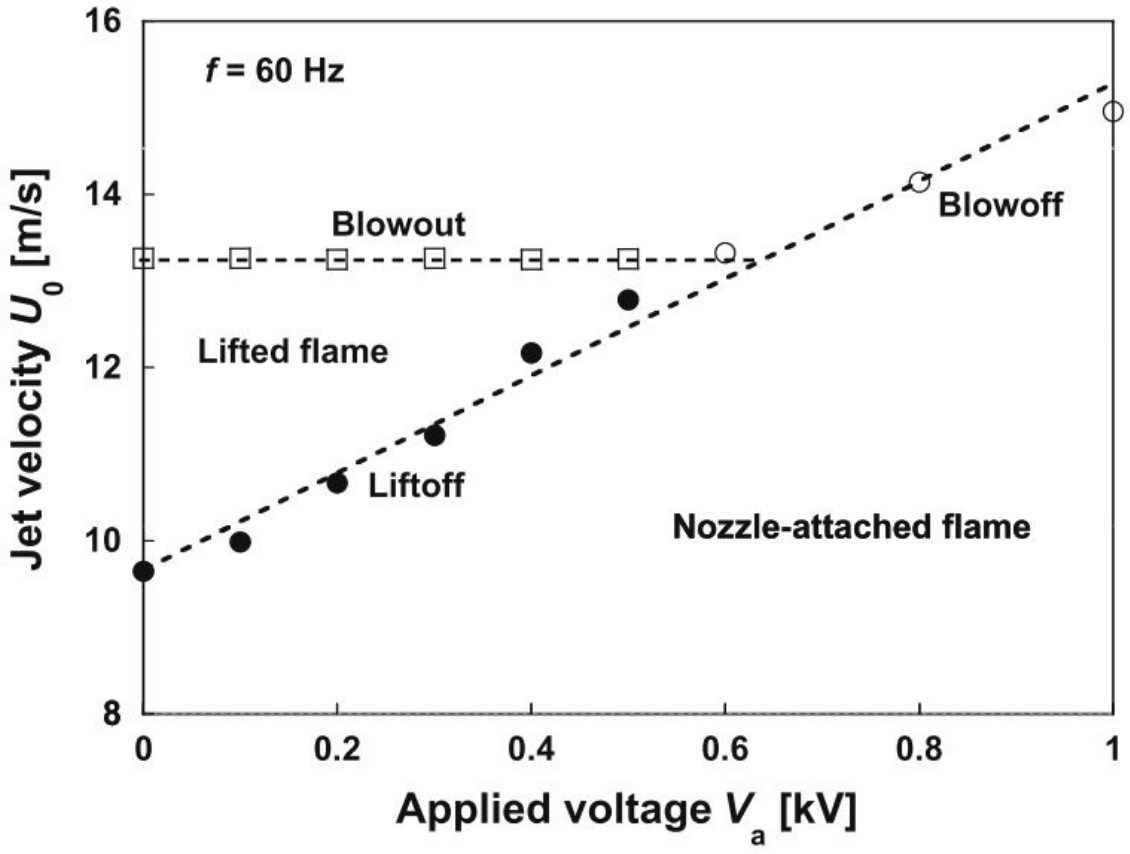

Figure 1.4 Map of flame stabilization for AC electric field by Kim *et al.* [62].

Ata *et al.* investigated the effects of a DC electric field on blowoff characteristics of bluff-body stabilized conical premixed flames [64]. As a result, the blowoff limit increased as the applied voltage increased. They suggested that flame stability, using an electric field, could be attributed to the ionic wind. However, in the studies of Kim *et. al.* [65, 68], of a laminar premixed Bunsen flame using an AC electric field bi-ionic competition between positively and negatively charged ions tended to move in opposite directions in an electric field. This finding could have an important role in a low frequency regime (f_{ac}< 60Hz), and the flame stabilization characteristics deteriorated as a

result of ionic wind. The authors attributed the improved stabilization for a high frequency regime ($f_{ac} \geq 60$Hz), to a chemical effect.

Most related studies show that enhanced flame stability exhibits extended stability limits in terms of jet velocity and/or a mixture composition; while few studies have reported deteriorated flame stability. Recalling that an electric field might cause hydrodynamic instability or thermo-mass diffusivity instability, resulting in wrinkled or cracked flame structures (discussed in section 1.3.2), an electric field can also be a source for other instabilities. To clearly understand the fundamental effects of electric fields on flame stability, an in-depth, organized approach to collecting key evidence is necessary.

Although many phenomenological results favor the positive impact of an electric field on flames exhibiting reduced soot emission, increased flame propagation speed and enhanced flame stability, detailed and solid mechanisms have not yet been presented to explain these observations. Basic research on flames with electric fields should be conducted persistently. The present study is part of a fundamental examination providing detailed experimental indicators to move forward; it will advance reference data for the validation of a predictive model.

1.4 Counterflow Flames

Why is it necessary to study combustion with one dimensional flame in a counterflow burner? To understand the concept of 1D flame with a counterflow burner, Fig. 1.6 presents the concept of the counterflow flame, showing practical flame and

counterflow flame. In practical combustion systems, turbulent flames with highly wrinkled flame surfaces, resulting from turbulent transport, are usually employed; their characteristics are difficult to analyze. To model a flamelet in a turbulent flame, a quasi-one dimensional counterflow flame has been designed, as shown in Fig.7 [102]. The counterflow geometry also provides easy access to well-developed numerical tools with relatively inexpensive grid, but with extensive chemical mechanisms. Thus, laminar nonpremixed or premixed counterflow flames have been extensively investigated in terms of flame structure [103-105], flame extinction [106-108], soot formation [109-111], flame propagation [112-114], and much more.

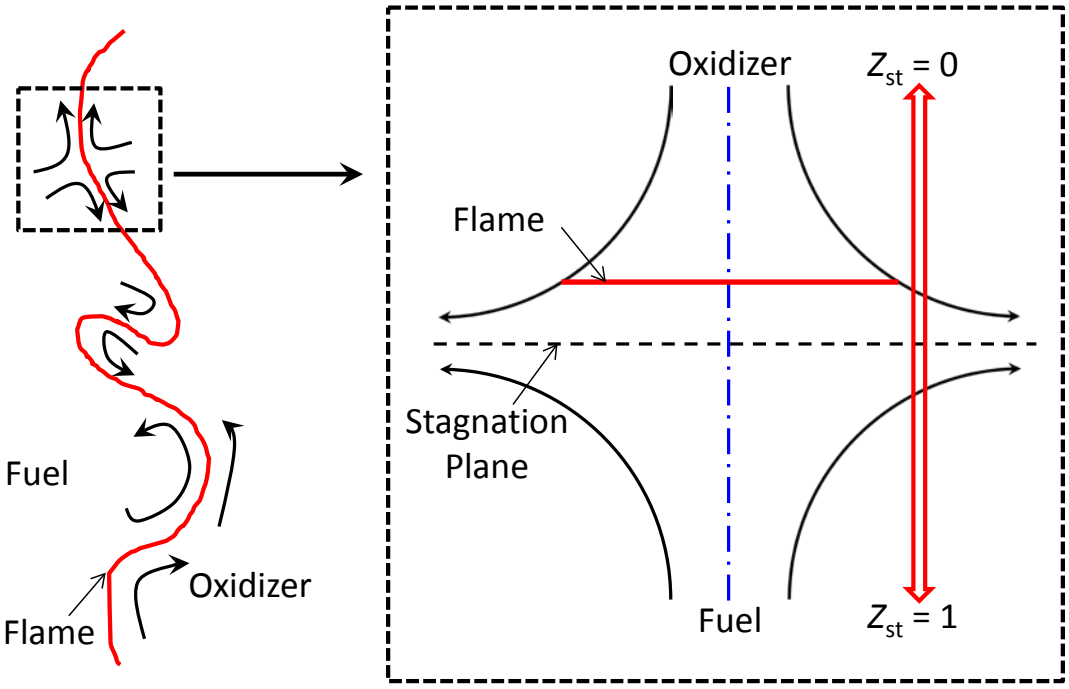

Figure 1.5 Concept of 1D nonpremixed counterflow flame.

Figure 1.6 Typical nonpremixed counterflow flame.

In the present study, nonpremixed counterflow flames were used to clarify the effects of electric fields on flame structure, flow fields, and the dynamic behavior of flame zones. Some advantages of using a counterflow burner for the present study are shown below,

1) Uniform electric fields.

2) Easy control of a flame position between two nozzles (electrodes).

3) Much existing comparison data and easy access to predictive tools.

1.5 Objective

As stated in the previous sections, there are many examples of electric field assisted combustion which could influence positive impacts on combustion characteristics such as soot emission, flame propagation speeds, and flame stabilities. However, detailed physicochemical mechanisms to explain the phenomenological observations have not as yet been fully available.

In this study, flame and flow characteristics were investigated in detail using external DC and AC electric fields in counterflow nonpremixed flame to propose a scientifically sound mechanism for the first order impact of electric field on a flame. To investigate and clarify the effects of an electric field, various measuring methods were employed such as laser based diagnostics, voltage current measurements, and high speed imaging. The main objectives of this study are as follows:

1) When soot zones exist in a counterflow nonpremixed flame, sooting flames are divided into two types, a soot formation and oxidation flame (SFO), and a soot formation flame (SF). The position of the flame can be manipulated by adjusting the initial concentrations of fuel or oxidizer. Therefore, it is of interest to investigate the difference in sooting characteristics in these two distinctive types of flame under electric fields. A DC was considered as a source of external electric fields.

2) Ions in a reaction zone of a flame generate a bulk flow motion referred to as *ionic wind* when these are exposed to external electric field. Because the

majority of ions are positive, ionic wind has been mistakenly assumed to be unidirectional, toward a lower electrical potential side. More thorough understanding of the effects of electric fields on a flame could be obtained by clarifying the role of negative ions in generating ionic wind. The characteristics of a flame, a flow field, and a response of electric current were examined in both counterflow nonpremixed flames and premixed Bunsen flames.

3) Ionic wind has also been perceived to play an important role in many phenomenological observations with electric fields in flames; however there is a lack of systematic quantification of ionic wind in interpreting the dynamic response of a flame to an electric field. To clarify the effects of electric fields, the various responses of nonpremixed flames--such as the flame's dynamic responses and the generation of bidirectional ionic wind--have been investigated here in relation to applied voltage and frequency of the alternating current (AC) in a counterflow burner.

1.6 Dissertation Outline

The organization of this dissertation is as follows:

Chapter 2: Experimental setup

The counterflow burner, electric field system, and laser diagnostics are summarized.

Chapter 3: Flame structure under an electric field

The flame structure and soot formation in nonpremixed counterflow flame were investigated with a DC electric field. The material within this chapter was published as: D. G. Park, B. C. Choi, M. S. Cha, and S. H. Chung, "Soot reduction under DC electric fields in counterflow non-premixed laminar ethylene flames", *Combustion Science and Technology*, Vol. 186, pp 644-656, 2014.

Chapter 4: Behaviors of flow, flame and electrical current under a DC electric field

The characteristics of the flame, flow and electric current under a DC electric field were reported, emphasizing bidirectional ionic wind. The material within this chapter was submitted and revised as: D. G. Park, S. H. Chung, and M. S. Cha, "Bidirectional ionic wind in nonpremixed counterflow flames with DC electric fields", *Combustion and Flame*, revision submitted, 2016.

Chapter 5: Study of DC electric field on flame and flow in premixed Bunsen flame

Flame movement and bidirectional ionic wind with a DC electric field were revealed in a premixed Bunsen flame having two parallel electrodes. The material within this chapter has been prepared for submission as: D. G. Park, S. H. Chung, and M. S. Cha, "Visualization of ionic wind in premixed bunsen flame with DC electric field", to *The Journal of Visualization*.

Chapter 6: Dynamic responses of flames to AC electric field

The dynamic responses of flames to an AC electric field were investigated with bidirectional ionic wind in nonpremixed counterflow flames. The material within this chapter was submitted and revised as: D. G. Park, S. H. Chung, and M. S. Cha, “Dynamic and electric current responses of counterflow nonpremixed flames to AC electric field”, 36th Proceedings of the Combustion Institute, submitted, 2016.

Chapter 7: Conclusion

A summary of the dissertation was made and future work is also discussed.

Chapter 2

EXPERIMENTAL SETUP

The experimental apparatus consisted of a counter burner, flow controllers, a power supply system and measurement instruments as shown in Fig. 2.1.

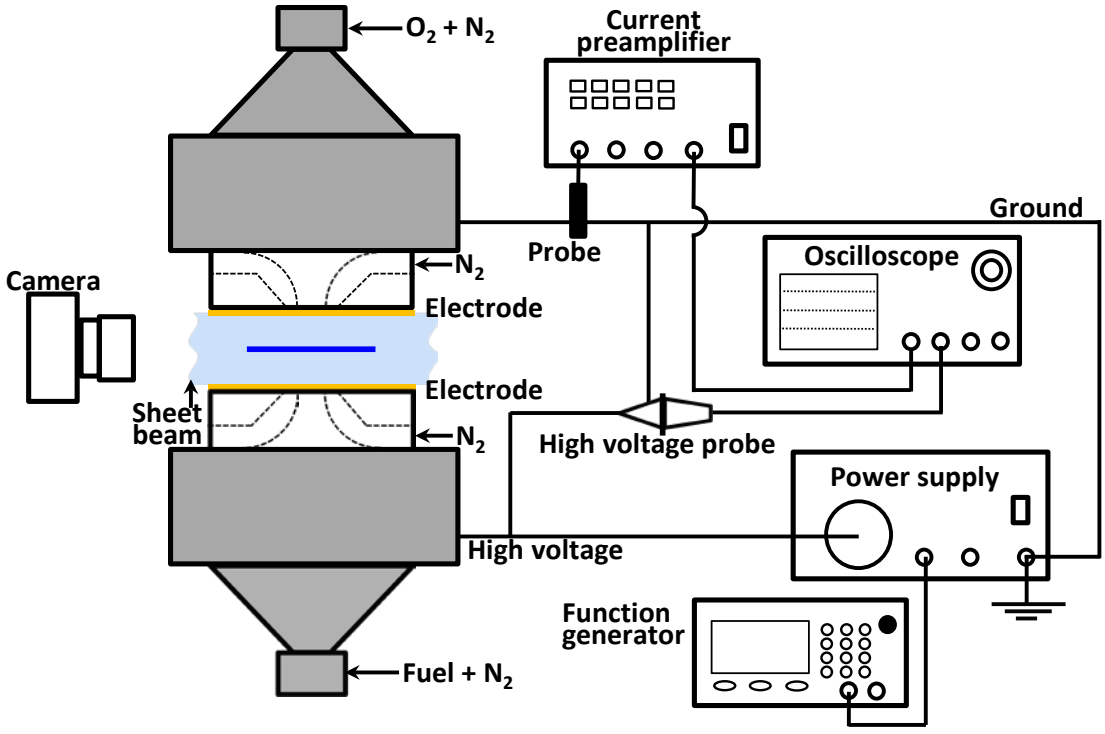

Figure 2.1 Overall experimental setup.

2.1 Counterflow burner

A counterflow configuration holds several advantages for a fundamental investigation of flames with electric fields. First, a quasi-one-dimensional electric field can be realized when two opposing nozzles are employed as electrodes for a high voltage and ground, respectively, so that uniform field intensity in any gap between the nozzles can be reasonably achieved. Second, unlike a burner-stabilized flat flame, the relative location of a flame with respect to electrodes can be easily controlled by adjusting a stoichiometric mixture fraction of the supplied mixture (explained in detail in Chapter 4). Another merit of a counterflow configuration is that (based on long history of research using counterflow burners), there are many previous works available for comparison and well-established experimental and numerical methods can be adopted or easily modified to implement detailed ion-chemistry and its interaction with an electric field. The present study has importance not only for fundamental understanding of the impact of an electric field on a flame, it is also a scientifically sound validation data for predictive tools.

Figure 2.2 shows the counterflow burner setup used in the present study. The counterflow burner was composed of two confronting nozzles with an exit diameter of 10 mm. Inside each nozzle a divergent-convergent section (a contraction ratio of a cross-sectional area is 1/64), was prepared to ensure a near-uniform velocity profile at the exit of the nozzle. The separation distance, L, between the exits of the nozzles could be varied from millimeters to centimeters. To electrically isolate each nozzle, the upper nozzle was fixed to an acrylic frame (non-conductive), and the lower nozzle was mounted on four posts made of acetal resin (non-conductive). The lower nozzle was placed on a three-

dimensional translational stage to adjust its position, so that each axis of symmetry for the nozzle could be aligned and the separation distance easily controlled.

The two main jets to form a nonpremixed flame (fuel and oxidizer streams), were supplied from the lower and upper nozzles respectively, and both jets were diluted with nitrogen to control the initial mass fractions of fuel and oxygen. A nitrogen sheath flow surrounded each main jet to prevent external disturbances and the formation of a secondary outer diffusion flame with ambient air. The velocity of the nitrogen sheath was controlled to be the same as that of the main jet. All flow rates of fuel, oxygen, diluting nitrogen, and sheath nitrogen were maintained using mass flow controllers (MKS, 1179A). Cooling water was supplied to the nozzles to maintain consistent inlet gas temperatures. A chiller (Thermo Scientific, LESLAB Thermo Flex 900), with a closed loop circulation of water was used for the supply of the cooling water. The temperature of the cooling water in the reservoir was set at 16 °C. Table 2.1 shows tested gaseous fuels and their purities, including oxygen.

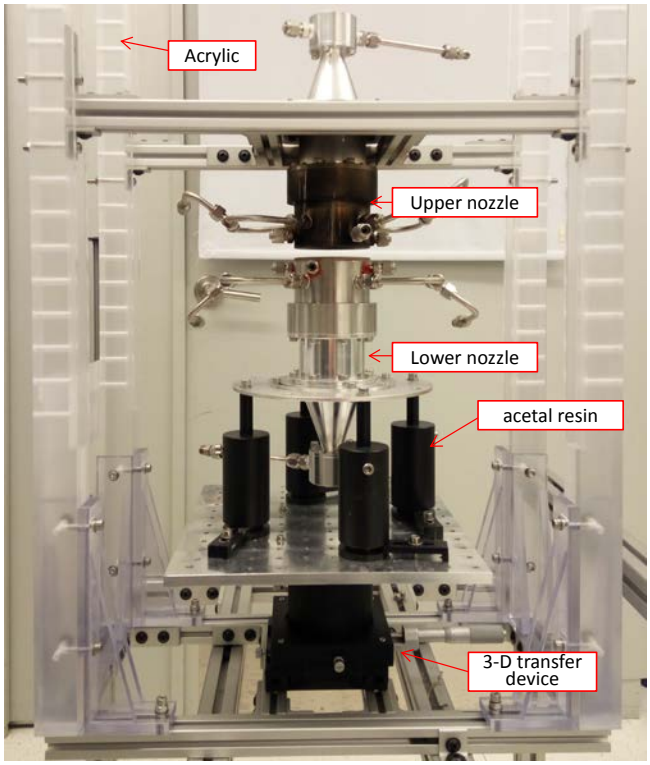

Figure 2.2 Counterflow burner setup including non-conductive frames and posts and three-dimensional translational stage.

Table 2.1 Purities of gases

Gas	Purity [%]
Methane (CH4)	99.995
Ethane (C_2H_6)	99.5
Ethylene (C_2H_4)	99.995
Propane (C_3H_8)	99.5
n-butane (C_4H_{10})	99.95
Oxygen (O_2)	99.999

2.2 Electric field setup

A power supply unit (Trek, 30/20A or 10/10B-HS), was used to apply DC and AC electrical potential. The power supply was a signal amplifier, able to amplify any arbitrary input signals up to 30 or 10 kV with a maximum current of 20 or 10 mA for 30/20A and 10/10B-HS power supply units, respectively. In the present study, a function generator (NF, WF1973) was employed as an input source to the power supply to produce DC and AC, depending on input waveforms. Note that sinusoidal waveforms were used for the generation of high voltage AC. A high voltage (V_{dc} or V_{ac}), generated from the power supply, was applied to the lower (fuel) nozzle, while the upper (oxidizer) nozzle was grounded.

To generate reasonably uniform electric fields in the gap between the nozzles, a perforated plate was placed at the exit of each nozzle. Hole density of the plate was 364/cm^2, with a hole diameter of 200 μm, used for investigating flame structure. A greater hole was necessary for flow field visualization studies to facilitate particle seeding; thus a plate with an 800-μm hole diameter, having a 79/cm^2 hole density was used (Fig. 2.3).

To characterize the response of a flame with an external electric field, a measurement of current, along with applied voltage, was essential. A current preamplifier (Stanford research system, SR570), was installed between the upper nozzle and the ground to precisely measure the electric current, while a 1000:1 voltage probe (Tektronix, P6015A) was connected to the lower nozzle to measure applied voltage; both current and voltage were monitored by an oscilloscope (Tektronix, MSO 2024).

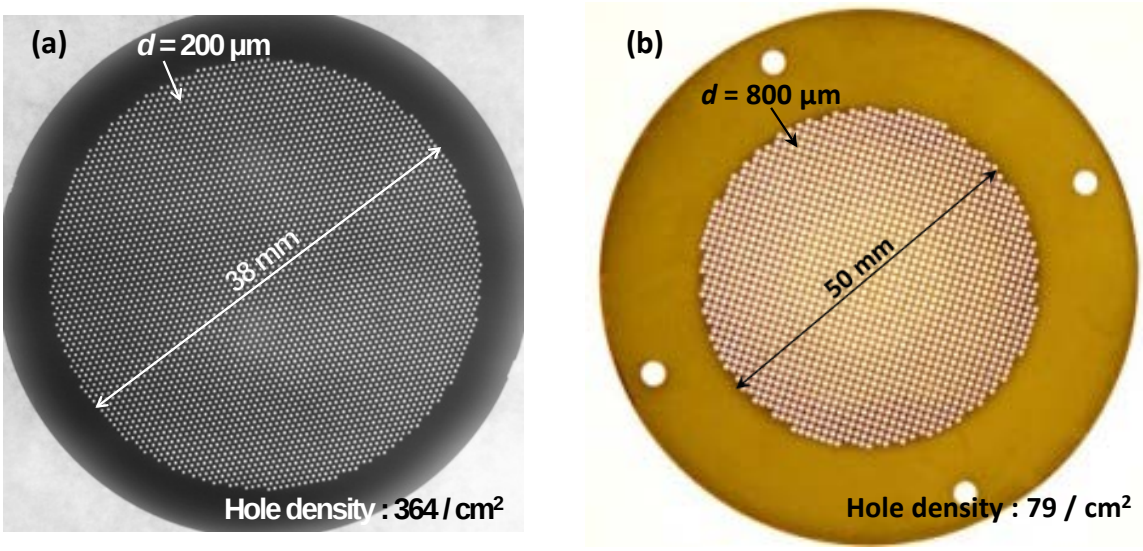

Figure 2.3 Perforated plates for electrodes at nozzle exits; for (a) flame structure and (b) flow field visualization study.

2.3 Laser diagnostics

Planar laser-induced fluorescence (PLIF), planar laser-induced incandescence (PLII), Mie scattering, and particle image velocimetry (PIV), were adopted to investigate flame structure represented by the distributions of OH radicals, PAHs, and soot particles, and to visualize and quantify a flow field. In order to make sheet beams to obtain 2D images, a cylindrical lens (f = 300 mm), and a convex lens (f = 1000 mm), were used for laser diagnostics systems (Fig. 2.4). The cylindrical and convex lens plays a major role in spreading the light in one direction and focusing the laser beam, respectively, to form a laser sheet of thin thickness for an area of interest.

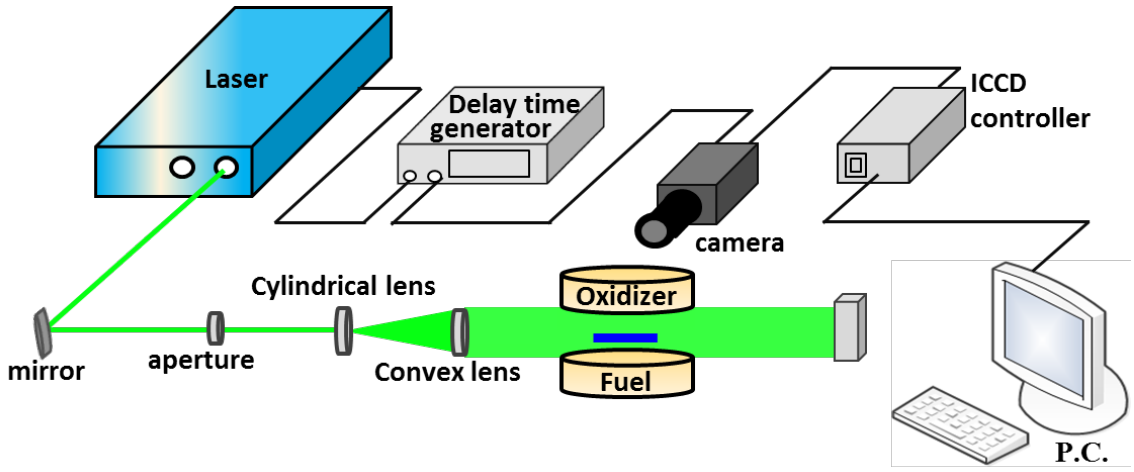

Figure 2.4 Schematic diagrams of laser diagnostics.

2.3.1 Planar Laser-Induced Fluorescence (PLIF)

A planar laser-induced fluorescence (PLIF) technique was adopted to visualize OH radicals and polycyclic aromatic hydrocarbons (PAHs). To construct the PLIF setup, a second harmonic (532 nm) of Nd:YAG laser (Continuum, PL9100), was used as the pumping source for a dye laser (Continuum, ND6000), with rhodamine 6G diluted by methanol. The output laser in the visible range was converted to ultra violet (UV) via a frequency doubler (Continuum, UVT). To excite OH radicals, $Q_1(6)$ line of the $A^2\sum^+ \leftarrow X^2\Pi$ transition at 282.96 nm was selected and a fluorescent signal was captured using a ICCD camera (PI, PI-Max3 1024i) with optical filters (UG-11 and WG-305), to eliminate flame luminosity and elastic scattering of the incident laser.

A slightly detuned wavelength of the laser (to 283.00 nm from the excitation line of the OH radical), was used to visualize PAHs. PAHs, which can be detected in sooting

flames as precursors of soot particles, are known to show broadband absorption and light emission [115]. The fluorescent emission spectra of PAHs are also known to depend upon the size of the PAHs. Lee *et al.* [116] conducted a comprehensive measurement of PAHs in a counterflow diffusion flame with narrow band-pass filters (FWHM = 10 nm), to differentiate the relative size of the PAHs changing a central wavelength of the filter from 330 to 500 nm. They reported that, as the detection wavelength increased, the corresponding fluorescent signal of PAHs moved closer to the sooting zone, indicating larger molecular sizes of the longer wavelength fluorescence emitted by the PAHs. For the present study, a detection wavelength centered at 450 nm was selected to obtain discernible separation from the sooting zone, which was also measured by PLII, to achieve reasonable signal-to-noise ratio (S/N).

2.3.2 Planar Laser-Induced Incandescence (PLII)

Planar laser-induced incandescence (PLII) was adopted to measure the qualitative soot volume fraction. A blackbody radiation from soot particles was heated by a high powered pulsed laser. Therefore, the PLII involved heating the soot particles to approximately 4000K above the surrounding gas temperature by the absorption of laser energy. The subsequent blackbody radiation corresponds to the elevated soot particle temperature [117].

Since PLII signals are the result of blackbody radiation from soot particles, they depend upon the characteristics of the laser and the properties of the particles, including

its specific heat capacity and mass. Thus the results of the PLII can be changed according to the experimental conditions. Generally, the intensity of the PLII signal increases with incident laser intensity before the soot particles reach the vaporization temperature [118]. In order to obtain precise results of the PLII signal, it is necessary to find the most suitable intensity of the laser.

The qualitative measurement of soot volume fraction was performed using the PLII measurement to investigate soot volume fraction with a DC electric field. The second harmonic (532 nm) of a Nd:YAG laser (Spectra-Physics, Pro-290-10EH), was used as the light source to heat the soot particles. Although the base wavelength of 1064nm for Nd:YAG laser can be used in PLII measurements, the wavelength 532 nm was chosen for a visible safety range. A narrow band-pass filter (centered at 410 nm, full width at half maximum, FWHM = 10 nm), was installed in front of the ICCD Camera to minimize the noise from scattering and fluorescence signals. In preliminary testing, laser intensity was selected at around 30mJ/pulse of the maximum PLII intensity condition. From ten repetitions, the two dimensional images for the PLII signal presented an average picture.

2.3.3 Mie scattering

Mie scattering is well known elastic scattering, meaning that a wavelength of incident light and of scattered light are not changed, and the scattering behavior (non-dimensional size parameter, *x*) is determined by the following equation (2.1).

$$x = \frac{2\pi r}{\lambda} \tag{2.1}$$

Where λ is wavelength and r is the radius of a scattering particle. A scattering from relatively minute particles (i.e. $x << 0.1$), is referred to as Rayleigh scattering. For particle sizes larger than a wave length, or similar to the wave length (i.e. $x > 1$ or $x \approx 1$), Mie scattering predominates. Figure 2.5 shows scattering strengths from different particle sizes for Rayleigh and Mie scattering. The signal from scattering is apparent, with large sized particles in the direction of incident light (forward scattering), which is much stronger than Rayleigh scattering. The Mie scattering method is appropriate for flow visualization of small particles.

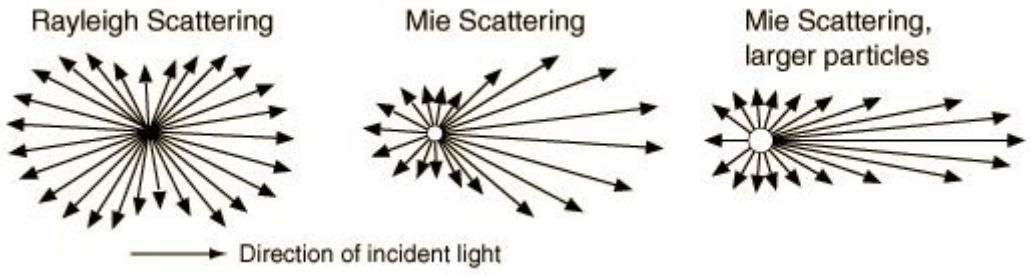

Figure 2.5 Scattering strength from different particle sizes [119].

In this study, the Mie scattering method was adopted to visualize the flow field with an electric field. This process uses a sheet beam produced by a continuous wave Ar-ion laser (Spectra-Physics, Stabilite 2017, 488 nm) to illuminate seeded titanium dioxide (TiO_2) particles (~ 0.2 μm). The optimized size of the particles should be considered, so that there is no change in flow properties and the scattering signal should be visible in the measuring camera [120]. The TiO_2 particle is suitable for visualization in reacting flows

in general; electrically non-conductive material was supplied through the main fuel and oxidizer nozzles. Seeders (LaVision, VZ-seeder) were used and rocked from side to side to maintain a number density of the particles in the area of interest. In order to supply the seeding particles to a reaction zone, a small quartz tube (0.8 mm i.d. and 1.5 mm o.d.) was inserted, with nitrogen as a carrier flow (0.17 cm^3/s), when necessary. A high speed (Photron, Fastcam-2 and SA-4), and digital cameras (Nikon, D700 with a macro lens), captured the flame and the scattering image at a right angle to the direction of the laser sheet.

2.3.4 Particle Image Velocimetry (PIV)

In particle image velocimetry (PIV), flow velocity is inferred from the motion of the tracer particles. Velocity is measured as a displacement D (X; t', t'') of the tracer particles in a finite time interval $\Delta t = t'' - t'$,

$$\mathrm{D}\,(\mathrm{X};\mathrm{t}',\mathrm{t}'') = \int_{t'}^{t''} v[X(t),t]dt \qquad (2.2)$$

where $v[X(t)]$ is the velocity of the tracer particles. For ideal tracer particles, the tracer velocity v is equal to the local flow velocity. Mie scattering is used to allocate the location of tracer particles at any given instant, and then freeze particle motion at the given time. A pulsed laser with a very short pulse duration (e.g. Nd:YAG with ~10 ns pulse width) is generally used to irradiate the seeding particles. A system with dual Nd:YAG lasers facilitates the principle of PIV by freely adjusting the time interval between two independent laser pulses. Depending on the interest range of flow velocity,

the time interval should be controlled by considering a size within the measuring window. Finally, the direction and amplitude of the particle displacement are calculated based on a cross-correlation method using two images having the same scattered particles but in different instants, with a known time interval [121].

A commercial PIV system (LaVision, 2D-FlowMaster) was adopted to measure related flow fields. To obtain two images with a controlled time interval, a dual-pulse Nd:YAG laser (532nm, the second harmonic of Nd:YAG), and a synchronized dual-frame CCD camera (LAVISION, Imager pro X) were used. Compact light sheet optics (f = 50mm) having a combination of plano-convex and plano-concave cylindrical lenses were installed in front of a laser output to form a vertical sheet. The CCD camera was equipped with narrow band filter (LaVision, BP 532-3), which detects laser light at 532 nm with bandwidth of 3 nm. The time interval, Δt, between two images, was fixed at 500 μs, which is the suitable time interval to quantify a velocity in a range of O (10) cm/s. The images were acquired though ten repetitious measurements, and the average velocity vector, having x and y components, was calculated using commercial software (La Vision, DAVIS 8.0).

Chapter 3

FLAME STRUCTURE UNDER ELECTRIC FIELD

3.1 Background

Nonpremixed flames in a counterflow burner provide distinct contrasting flame configurations in sooting characteristics due to the relative location of the flame with respect to the stagnation plane. Typical counterflow nonpremixed flames are shown in Fig. 3.1. Because a soot zone always exists on the fuel side of a nonpremixed flame, when a flame is located on the fuel side (Fig 3.1a), soot particles are transported through the flame zone toward the stagnation plane, resulting in oxidation of the soot particles. This type of flame is called a soot formation/oxidation (SFO) flame [104]. On the other hand, when a flame stabilizes on the oxidizer side (Fig. 3.1b), a soot zone appears between the flame and the stagnation plane; thus the soot particles move away from the reaction zone without being oxidized. Eventually, the particles will leak through the particle stagnation plane. For this reason, this type of flame is referred to as a *soot formation flame* (SF) [104]; and the differences in the flame behavior and sooting characteristics of these two distinct types of flame under electric fields should be investigated.

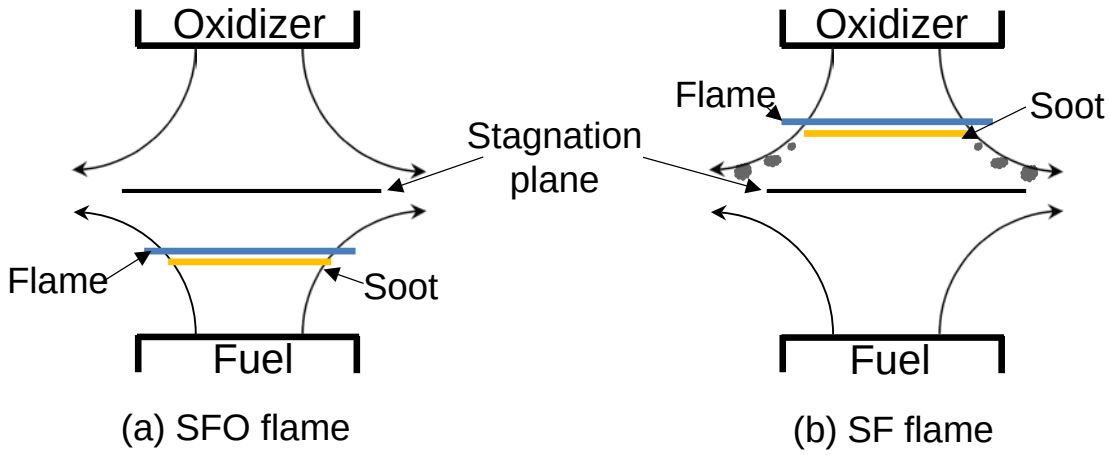

Figure 3.1 Typical counterflow nonpremixed flames; (a) soot formation oxidation flame (SFO), and (b) soot formation flame (SF).

With this motivation, soot formation of ethylene/oxygen nonpremixed flames diluted with nitrogen in a counterflow burner was studied experimentally by applying a DC electric field. The detailed characteristics of the flames and soot for SFO and SF conditions are discussed in this chapter.

3.2 Experimental condition

Ethylene and oxygen diluted with nitrogen was used for this study of flame structure under a DC electric field. The C_2H_4/N_2 mixture was ejected from the lower nozzle and the O_2/N_2 mixture was supplied through the upper nozzle. To represent SFO flames, initial mole fractions of ethylene and oxygen at the exits of the nozzles of (X_{C2H4}, X_{O2}) = (0.25, 1.0) were chosen. The reactant condition of (X_{C2H4}, X_{O2}) = (1.0, 0.25) for

the SF flames was used for comparison with the SFO flames. Regardless of the composition of the mixture, the nozzle exit velocity, U_0, was fixed at 20 cm/s to maintain a constant strain rate throughout the experiment. To mitigate the shear between the central jet and the shield flow, the velocity of the shield nitrogen was matched with that of the corresponding central jets, i.e., 20 cm/s. The separation distance, *L*, between the two exits of the nozzles was fixed at 11 mm. A DC electric field in a range of –5 kV$<V_{dc}<$ 5 kV was applied. Uniform electric was generated in the gap between two nozzles by using a perforated plate (Fig. 2.3a).

3.3 Results and discussion

3.3.1 Effect of DC electric fields on flame behavior

The visible variation in flame characteristics was observed first. Fig. 3.2 shows typical flame images taken with a digital camera (Nikon, D700) at selected applied voltages. As shown in Fig. 3.2(a) of the representative SFO flame, in the case with no applied voltage (V_{dc} = 0), yellow luminosity, caused by black body radiation from the soot particles, appeared on the fuel side. No significant difference was detected for small increases in applied voltage up to ± 0.2 kV. However, at V_{dc} = − 2 kV, a significant reduction in yellow luminosity was identified, as well as a drastic change in the flame location toward the lower nozzle. The flame showed an unstable fluctuating behavior with a positive applied voltage (V_{dc} = 2 kV).

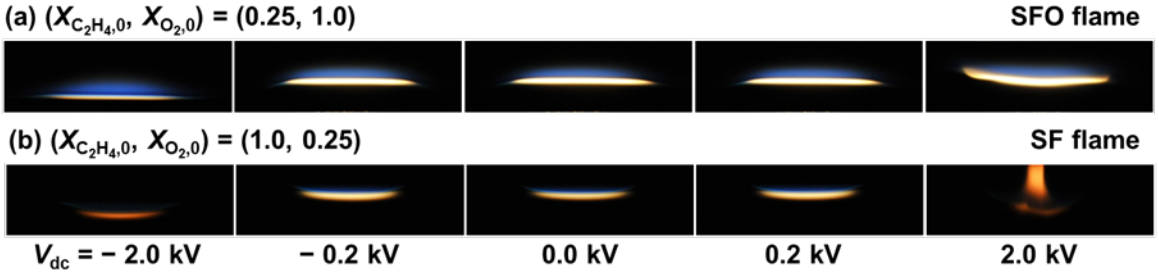

Figure 3.2 Photographs of typical flames with selected applied DC voltages: (a) SFO configuration (X_{C2H4}, X_{O2}) = (0.25, 1.0), (b) SF configuration (X_{C2H4}, X_{O2}) = (1.0, 0.25). The heights of the photographs indicate the gap between the two nozzles, i.e., 11 mm.

The SF flames show relatively weaker yellow luminosity compared to the SFO flames (Fig. 3.2b). This is partly because most of the soot particles leaked out along the streamlines without passing through the hot reactive zone. Similar to the SFO case, a significant change was observed in the luminosity and location of the flame for V_{dc} = −2 kV, while negligible variations were found for –0.2 kV <V_{dc}< 0.2 kV. Unstable fluctuating flame behavior was observed for V_{dc} = 2 kV.

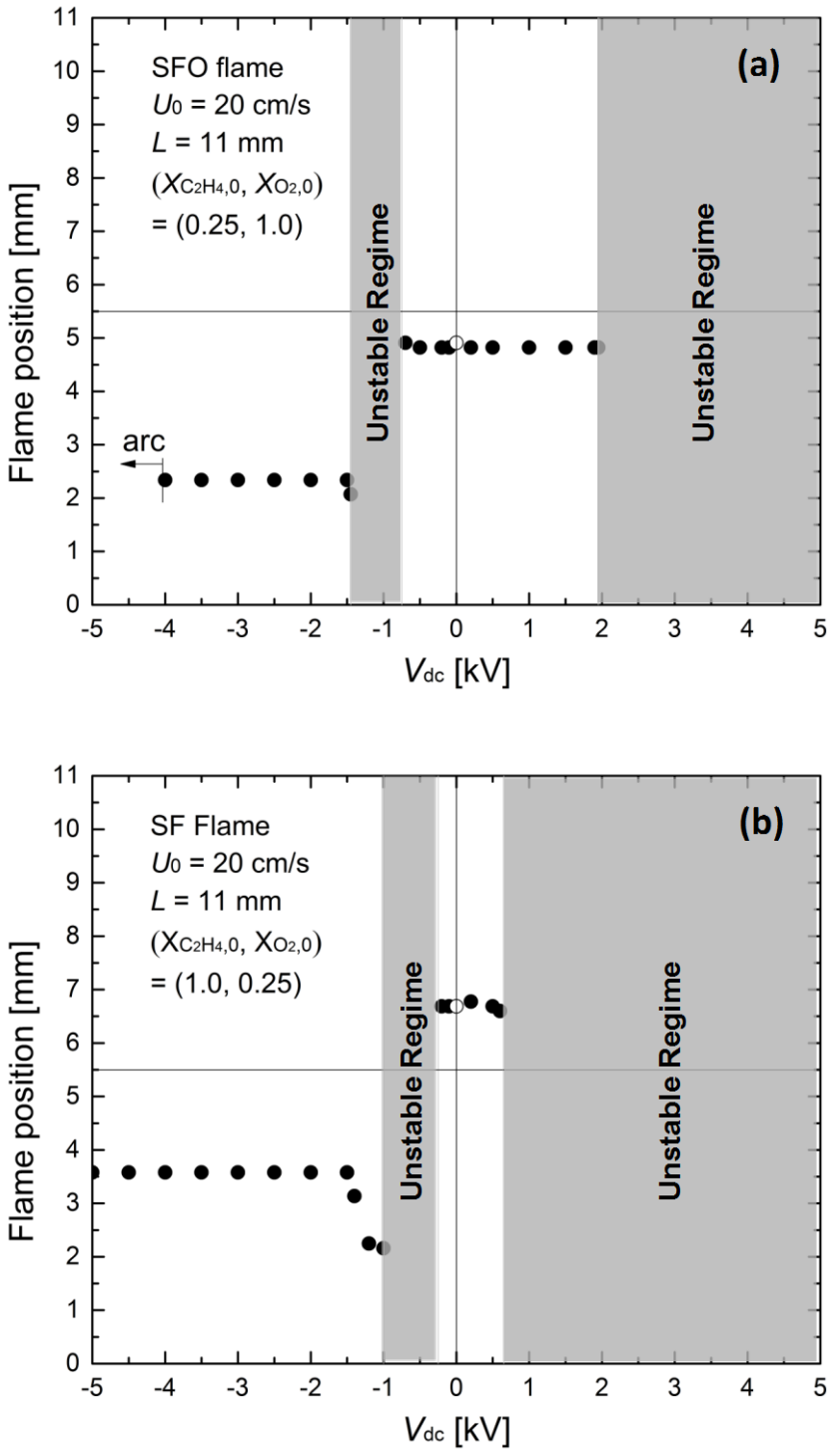

Figure 3.3 Variations in flame position with applied voltages: (a) SFO configuration (X_{C2H4}, X_{O2}) = (0.25, 1.0), (b) SF configuration (X_{C2H4}, X_{O2}) = (1.0, 0.25). The exit of the lower (fuel) nozzle was at 0 mm, while the upper (oxidizer) nozzle was 11 mm.

Figure 3.3 shows plots of the flame positions with the applied voltages for the corresponding flame configurations shown in Fig. 3.2. The position of the flame was defined as the axial location between the blue and yellow luminous zone along the centerline, measured from the lower nozzle. For an increasingly negative applied voltage, the flame shows negligible changes in its position until it suddenly enters an unstable regime ($-1.45 < V_{dc} < -0.8$ kV and $-1.0 < V_{dc} < -0.25$ kV, for the SFO and SF conditions, respectively). The flame then restabilizes at its new position (2.3 and 3.6 mm for the SFO and SF conditions, respectively), at a higher applied voltage.

It should be noted that in the SFO flame, an electrical arc was encountered beyond $V_{dc} = -4$ kV. For the positive applied voltages however, no significant changes in the flame positions were observed before the flames became unstable. Eventually an electrical arc occurred at voltages greater than 5 kV.

Ions exist through chemi-ionization processes in a reaction zone on the order of 10^9 - 10^{12} /cm3 [12]. Moreover, it has been reported that a significant number of PAHs and soot particles also could be positively charged [28]. These charged species are selectively accelerated by the Lorentz force qE, where q is the electric charge of the particle and E is the electric field intensity. Due to a random molecular collision with a collision frequency f, the accelerated ions are expected to transfer most of their energy to neutral particles. This process can generate unidirectional bulk flow motion, referred to as *ionic wind*. When DC voltage was applied at the fuel nozzle (lower) in this experiment, the ionic wind could interact with the pre-existing flow field, and the well-proven counterflow pattern could be destroyed. Therefore, the diffusion flame position, determined by the

initial mass fraction of each reactant, the location of the stagnation plane, and the strain rate, will be affected by the electric fields. In Chapter 4 the solution will be presented.

For an increasingly negative applied voltage, the position of the flames restabilized on the fuel side (negative potential), where they demonstrated negligible differences in their position above a critical voltage. These downshifts of the flame positions are in accordance with the direction of the Lorentz force acting on the positive charges. This can be understood based on the fact that electrons must be present to balance the electric neutrality in the flame; therefore there are more positive than negative ions. Regardless of V_{dc} after restabilization, the constant flame positions are a result of an ion current limitation above the critical voltage [69]. Similar to the saturation of the ion current along with the external voltage, the ionic wind can also be limited by the rate of ion generation in the reaction zone.

For the positive applied voltage however, the flames became unstable and fluctuated irregularly and non-axisymmetrically. Because this is difficult to explain for the unstable flame, the current discussion is limited to stable flames with negative voltages.

3.3.2 Flame structure and soot formation under DC electric fields

Because dramatic changes were also observed in the yellow luminosity from soot particles after applying negative voltages (Fig. 3.2), the soot characteristics (including the PAH and OH radical distributions), were investigated using laser-based diagnostics.

Figure 3.4 shows the qualitative distributions of the soot particles, PAHs and OH radicals. The images in the upper row correspond to the baseline flames with no electric field, including the SF flame (Fig. 3.4a), and SFO flame (Fig. 3.4b). Mixture conditions are the same as in Figs. 3.2: (X_{C2H4}, X_{O2}) = (1.0, 0.25) for the SF flame and (X_{C2H4}, X_{O2})= (0.25, 1.0) for the SFO flame. The PLII signal, which represents the soot volume fraction, is depicted on the left side of each image with respect to the centerline of the burner, while the PAH and OH PLIF images are shown on the right side.

In the baseline flame under SF conditions (Fig. 3.4a), because the main reaction zone of the OH radicals is located on the oxidizer side, soot particles and PAHs leak out radially along the streamlines of the counterflow geometry, as expected in a typical SF flame. However, the SFO flame (Fig. 3.4b), contains a vast distribution of OH radicals and a relatively small amount of soot particles due to the oxidative structure of the flame. The soot particles are fully oxidized within the reaction zone, and the level of PAHs is significantly smaller than that of the SF flame.

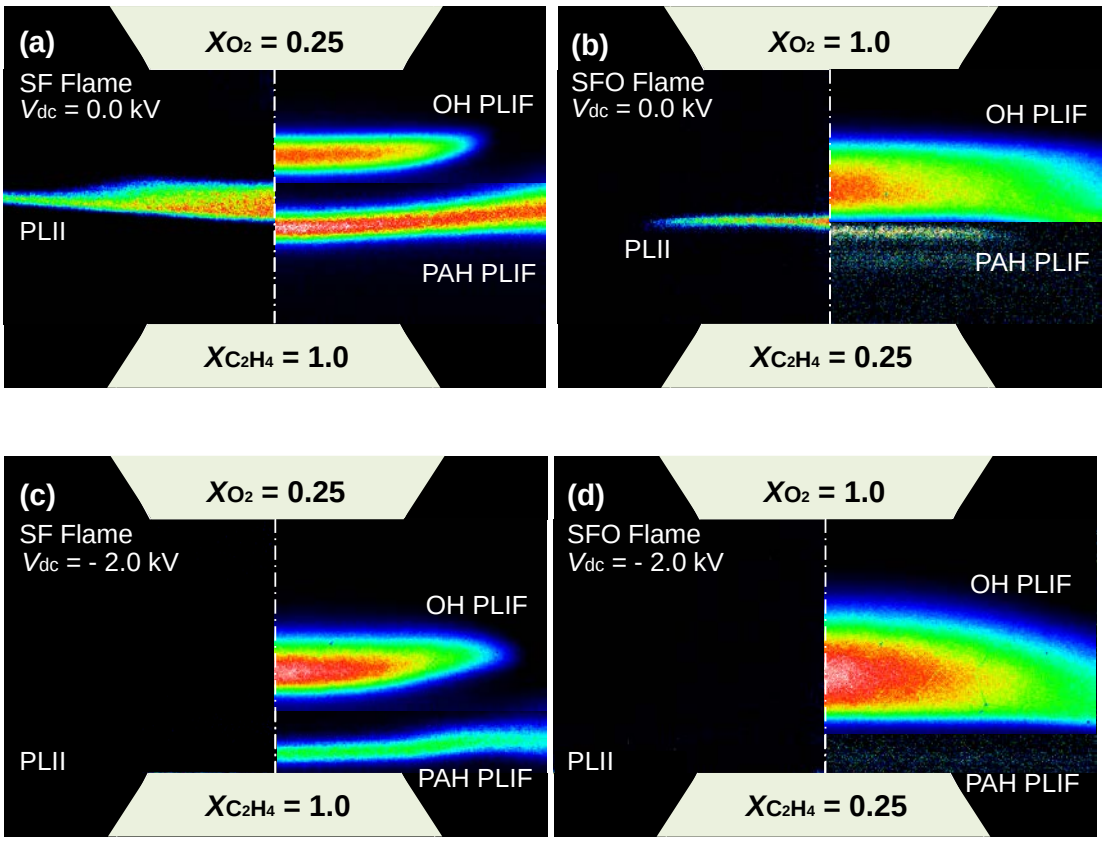

Figure 3.4 Images of soot volume fraction, PAHs, and OH radicals measured by the PLII and PLIF techniques: (a) the baseline SF flame, (X_{C2H4}, X_{O2})= (1.0, 0.25), without electrical potential, (b) the baseline SFO flame, (X_{C2H4}, X_{O2}) = (0.25, 1.0), without electrical potential, (c) SF flame at V_{dc} = – 2.0 kV; (d) SFO flame at V_{dc} = – 2.0 kV.

Interestingly, the soot particles were drastically reduced in both flames by applying V_{dc} = − 2.0 kV, as shown in the lower two images. The PLII signal could not be identified, and PAH had a much weaker PLIF intensity, as well as a significant modification in its spatial distribution toward the fuel nozzle. The OH PLIF intensity became stronger and wider when it was subjected to the DC electric field. The PAH

distribution for the SF flame at V_{dc} = − 2.0 kV should be emphasized. As shown in Fig. 3.4c, PAH is still leaking from the reaction zone, indicating a valid SF configuration of the flame. This implies that the location of the stagnation plane relative to the flame may be similar to the baseline case without the electric fields. In this regard, the new location for the stagnation plane is expected to be near the exit of the fuel nozzle.

To understand the detailed variation of PAH distribution with the electric field, the intensity of the PAH PLIF, along with the centerline of the burner, is plotted in Fig. 3.5 for SF flames with selected values of V_{dc}. The origin on the x-axis indicates the exit of the fuel nozzle. As previously discussed, because the unstable regime was found to be in the range of $-1.0 < V_{dc} < -0.25$ kV, two isolated groups of data could be identified. For a small value of V_{dc} = ± 0.2 kV, the PAH PLIF does not significantly change location, while the intensity slightly increases at V_{dc} = – 0.2 kV and decreases at V_{dc} = 0.2 kV from the baseline flame at V_{dc} = 0. Then, after restabilizing at more negative voltages, the locations of the PAHs change abruptly to only 1 mm from the fuel nozzle. The peak intensities are less than half of those for the baseline flame, which demonstrates the insensitivity to V_{dc}. A detailed discussion of a viable hypothesis will be presented here. It should be noted that in the SFO flame, only an insignificant amount of the PAH PLIF signal could be measured for all tested values of V_{dc}; thus, no PAH PLIF characteristics for SFO flames could be discussed in this study.

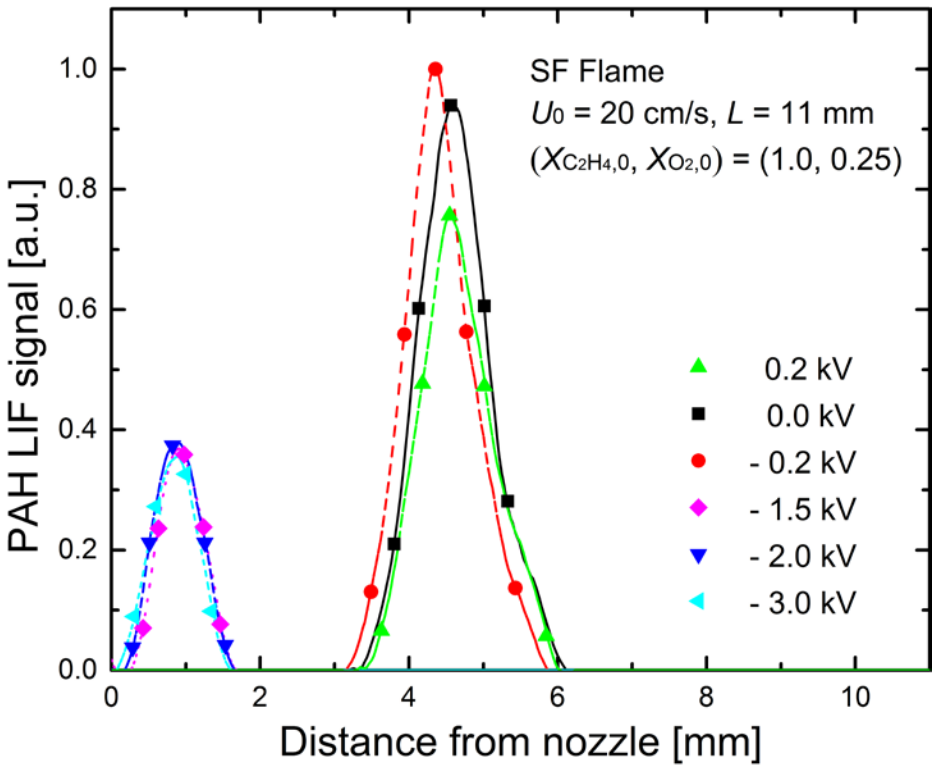

Figure 3.5 Axial profiles of the PAH PLIF signal along the centerline of the burner for SF flames, (X_{C2H4}, X_{O2}) = (1.0, 0.25), at various applied voltages.

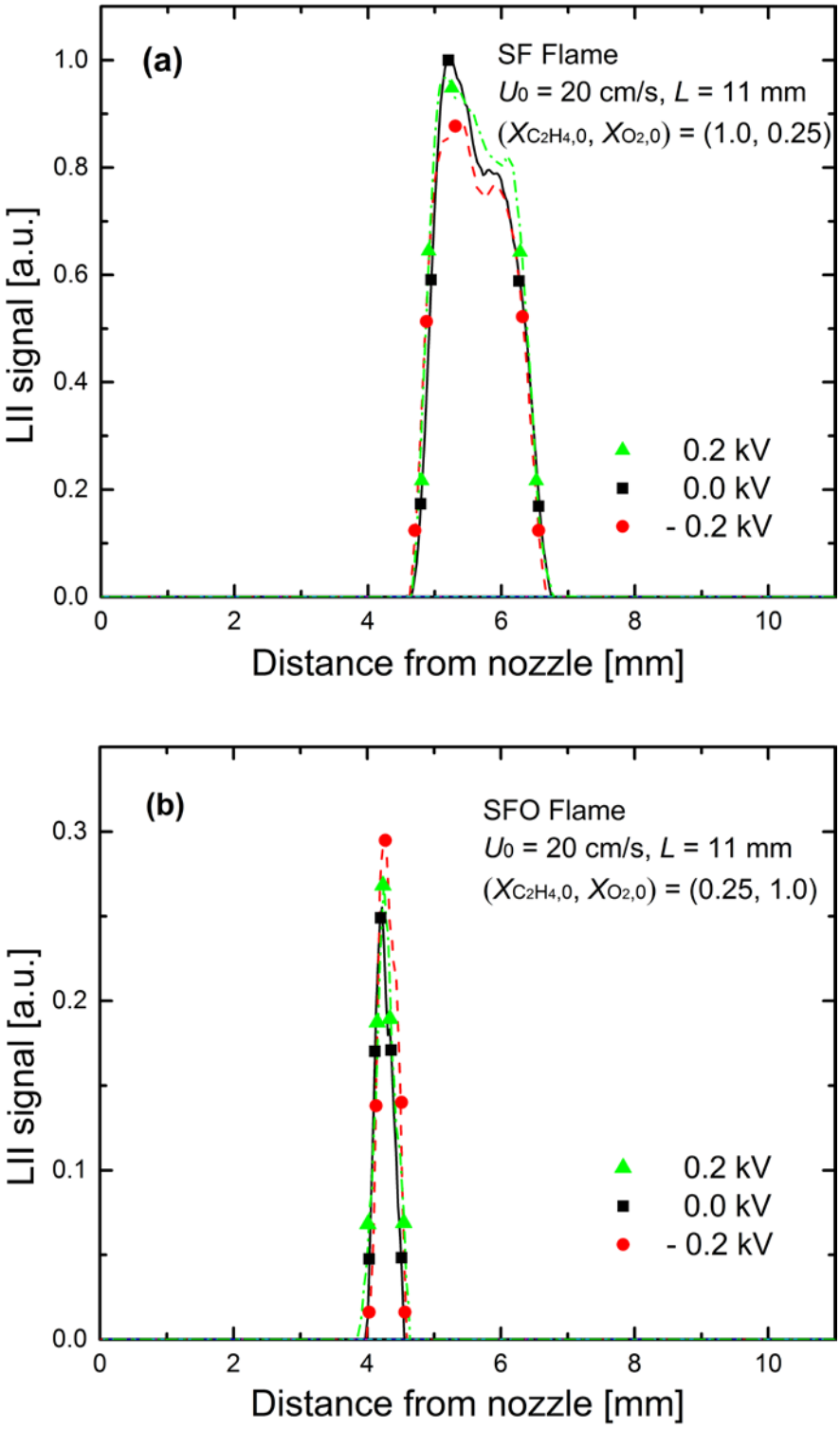

Figure 3.6 Axial profiles of the PLII signal along the centerline of the burner for various applied voltages: (a) SF (X_{C2H4}, X_{O2}) = (1.0, 0.25); (b) SFO flames, (X_{C2H4}, X_{O2}) = (0.25, 1.0).

Figure 3.6 shows the axial distribution of the PLII signal, which represents the soot volume fraction along with the centerline of the burner for SF (a) and SFO (b) flames. The distribution of soot particles for the baseline SF flame is closer to the oxidizer side than to the baseline SFO flame due to the difference in the mixture fractions. Similar to the PAH characteristics with the electric fields, for V_{dc} = ± 0.2 kV, the distribution of soot particles is relatively insensitive to V_{dc} for both the SF and SFO flames. However, no significant PLII signal could be obtained for $-3.0 < V_{dc} < -1.5$ kV, indicating that soot formation was efficiently suppressed using the DC electric fields.

3.3.3 Sooting limits under DC electric fields

To further identify the sooting characteristics with DC electric fields, the sooting limits of ethylene diffusion flames at V_{dc} = 0 kV and V_{dc} = – 2 kV were compared. By varying the ethylene (oxygen) mole fraction and fixing the mole fraction of oxygen (ethylene) at 1.0, we measured the LII signal and plotted the maximum LII intensity along the centerline in Fig. 3.7a (Fig. 3.7b).

When the oxygen mole fraction was increased at X_{C2H4} = 1.0, the flame temperature increased. Overall soot formation (fuel → C_2H_4→ PAH → soot nuclei), and oxidation processes were influenced by flame temperature. Hydrogen abstraction/acetylene addition mechanisms (HACA), which are closely related to PAH growth, are especially known to be enhanced at higher flame temperatures [122, 123]. Consequently, the PAH and soot volume fraction rose with the increase of the oxygen mole fraction. Moreover, when the ethylene mole fraction was increased at X_{O2} = 1.0, not only did flame

temperature increase, but C_2H_2 and PAH concentration was also enhanced due to the increase of fuel concentration [104]. As a result, soot volume fractions gradually rose as the ethylene mole fraction increased.

The trend of LII in normal flames without electric fields suddenly increases at certain values of ethylene and oxygen mole fraction (Fig. 3.7a and 3.7b, respectively). Using two different linear relations, as schematically depicted in figure [124], the sooting limit can be determined in terms of the ethylene (oxygen) mole fraction for X_{O2} = 1.0 (X_{C2H4} = 1.0). The sooting limit was found to be X_{C2H4} = 0.236 (X_{O2} = 0.206) for a given X_{O2} = 1.0 (X_{C2H4} = 1.0), which agrees with the results of a Hwang *et al.* [125].

For flames at V_{dc} = – 2.0 kV, however, no such obvious change in PLII intensity was observed, which implies no significant soot formation at V_{dc} = – 2.0 kV, as confirmed previously. Though the PLII could not be measured for X_{C2H4}> 0.5 (X_{O2}> 0.5) due to the formation of an electrical arc between the nozzles, it was concluded that the DC electric fields could effectively control the sooting characteristics in the counterflow diffusion flames.

Because the formation of PAHs and soot particles depend heavily on temperature, residence time in a hot environment, and on fuel mole fraction [109], the modified flow field through the ionic wind may be an unfavorable environment for soot to form and grow. The reduction in the distance from the fuel nozzle (lower), to the flame, indicates increased heat loss to the nozzle and decreased residence time for fuel to be decomposed and form PAHs. The ionic wind blowing from the reaction zone may dissipate heat energy and lead to decreased temperature. The previously mentioned alteration of the stagnation plane also leads to a modified strain rate in the reaction zone; this factor

should also be accounted for. Nevertheless, it is difficult to determine an exact explanation for the results. To understand the results of soot reduction under DC electric fields, the flow visualization is investigated in the next chapter (Chapter 4).

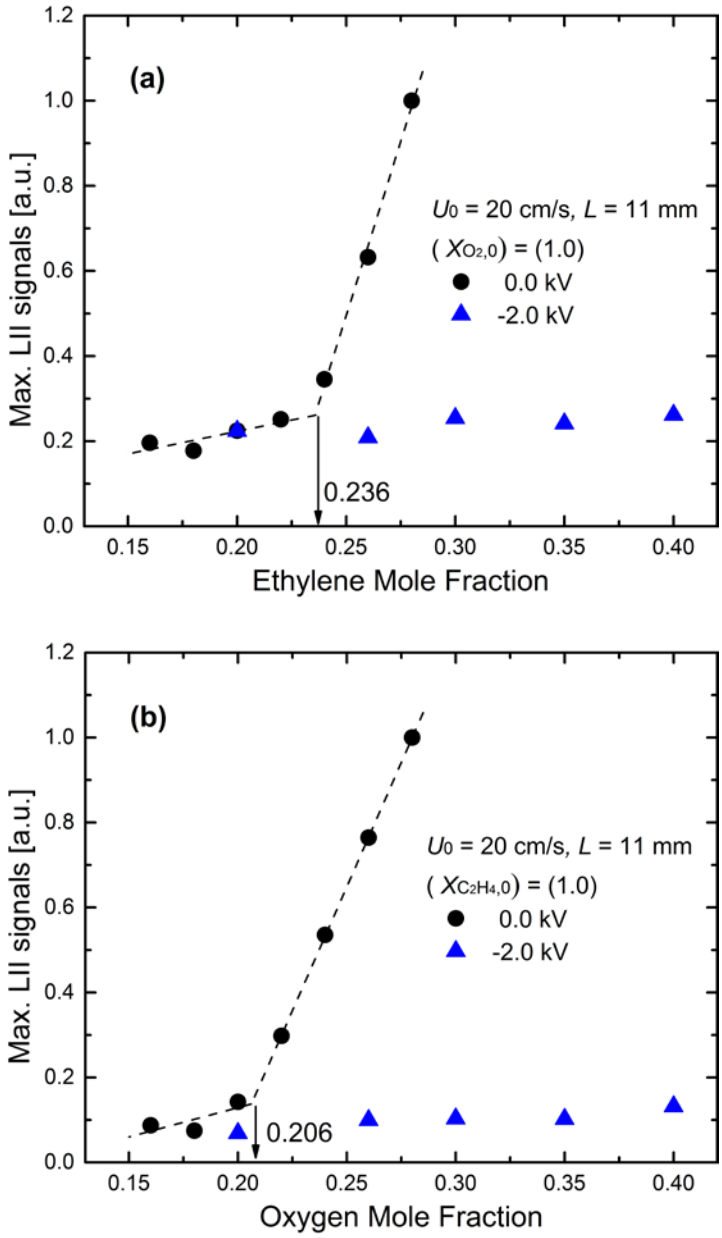

Figure 3.7 Comparison of the sooting limits of ethylene in a counterflow configuration at V_{dc} = –2.0 kV and without electric fields: (a) ethylene mole fraction for a given oxygen mole fraction at X_{O2}= 1.0, (b) oxygen mole fraction for a given ethylene mole fraction at X_{C2H4} = 1.0.

3.4 Summary

The effect of DC electric fields on nonpremixed ethylene flames in a counterflow burner was studied experimentally. For negative electric fields applied on the fuel nozzle (lower nozzle), the flames moved and restabilized toward the nozzle after demonstrating some instability; while unstable fluctuating flames were observed at positive voltages. This displacement of the flame position can be explained by the Lorentz force acting on positive ions in the flames. In addition, after restabilization with the negative voltages, a reduced luminosity from typical bright yellow flames caused by soot particles was identified. The results of the PLII and PLIF measurements of soot particles and PAHs demonstrated that no PLII signal could be detected, indicating that soot particles were reduced significantly by applying negative voltages. Moreover, at V_{dc} = – 2 kV, no noticeable sooting limit of ethylene was found by varying the ethylene (oxygen) mole fraction with respect to a fixed oxygen (ethylene) mole fraction of 1.0 in the counterflow configuration. Modification of the ionic wind-driven flow field reduced soot particles by affecting the flow residence time, the temperature field, and the strain rate, which are important factors for the formation and growth of soot.

Chapter 4

FLOW CHARACTERIZATION UNDER A DC ELECTRIC FIELD

4.1 Background

One of the most pronounced effects of an electric field on flames is the observable bulk flow motion, ionic wind, which has been demonstrated under microgravity conditions [66]. When an external electric field, E, is applied to a flame, the Lorentz force acts on the charged particles, causing them to accelerate. This triggers a directional drift velocity of the charged particles, expressed as μE, where μ is ion mobility. Thus, positive ions migrate toward the cathode (lower potential electrode) following electric field lines, while electrons and negative ions move in the opposite direction (anode, higher potential electrode).

This movement of charged particles in a hydrocarbon flame creates an electric current [79]. When the field intensity increases, the current shows a near-parabolic increase, up to a moderate external field (sub-saturated regime), and over a certain field

intensity; it demonstrates a saturated value depending on the rate of ion generation (saturated regime). During this dynamic response of charged particles due to external fields, a momentum transfer from charged particles to neutral molecules generates ionic wind.

In reaction zones, positive ions are in excess of negative ions; negative charge carriers include both negative ions and electrons; thus the total number of negative charges should be equal to that of positive charges. Because the mass of electrons is negligible, so is their contribution to momentum transfer and their effect on ionic wind. For this reason, positive charges are considered to be chiefly responsible for the momentum transfer that results in unidirectional ionic wind toward a cathode. However, when a low-frequency alternating current (AC) electric field was applied in a recent study [68], momentum transfer by negative ions resulted in a bi-ionic wind effect, indicating that momentum transfer by a relatively small number of negative ions contributes to the blowoff behavior of premixed Bunsen flames.

In summary, both positive and negative ions can contribute to the generation of ionic wind in opposite directions towards a cathode and anode, respectively. This bidirectional ionic wind may produce visible effects on a flow field if the flow velocity near the flame is reasonably smaller than the flow velocity which is the result of ionic wind. A flow stagnation plane in a counterflow burner provides a suitably low-velocity environment to observe this bidirectional ionic wind.

In Chapter 3 the sooting characteristics of ethylene nonpremixed flame in a counterflow burner with a direct current (DC) were presented. It was shown that soot

formation was effectively suppressed, regardless of initial fuel and oxygen mixture fractions. Although the visualization of polycyclic aromatic hydrocarbons (PAHs), and OH radicals with a laser-induced fluorescence technique supported an observed reduction in soot particles, it was still necessary to find the underlying physicochemical mechanism. Because a nonpremixed flame in a counterflow burner is sensitive to flow and concentration fields [109, 125], an ionic wind and the consequent modification of the flow field should have an important role in the change in the flame structure and should be further investigated.

Thus, flow-field modulations and electric current responses of nonpremixed counterflow flames were experimentally investigated by applying a direct current (DC). To amplify the effect of ionic wind, the nonpremixed flames were stabilized with various fuels near the stagnation plane so that the axial flow velocity was minimal in the reaction zone. Here the flow of bidirectional ionic wind was visualized to establish connections with measured flame positions and electric current.

4.2 Experimental conditions

The counterflow burner had two opposing nozzles (top and bottom), each with an inner diameter of 1 cm, and two separation distances, L = 1 and 1.5 cm were tested. Detailed velocity conditions (mean velocities (U_j) at the nozzle exit), can be found in Table 5.1 for various tested strain rates. Fuels tested included methane (CH_4), ethane (C_2H_6), propane (C_3H_8), and n-butane (C_4H_{10}) with oxygen (O_2) as an oxidizer.

Electrically conductive perforated plates (79/cm^2 hole density, 0.8-mm hole diameter) with 8.0-cm diameters were placed at nozzle exits to serve as electrodes, as shown in Fig. 2.3b, ensuring that reasonably uniform electric fields were maintained in the region between the nozzles.

The Mie scattering method was used to visualize the flow field. This process uses a sheet beam from a continuous wave produced by an Ar-ion laser to illuminate seeded TiO_2 particles (~ 0.2 μm). The TiO_2 particles were supplied through the main fuel and oxidizer nozzles, or a small quartz tube was inserted to supply the particles into a reaction zone, which will be detailed later. A digital camera with a macro lens captured flame and scattering images. Particle image velocimetry was adopted to measure the flow field and--when necessary--a small quartz tube (0.8 mm i.d. and 1.5 mm o.d.) supplied seed particles close to the reaction zone with a nitrogen carrier flow (33 cm/s).

Table 4.1 shows experimental conditions for various fuels, maintaining a stoichiometric mixture fraction, Z_{st}, defined as $1/(1 + \nu Y_f/Y_o)$, where ν is the stoichiometric oxygen-to-fuel mass ratio and Y_f and Y_o represent mass fractions of fuel and oxygen, respectively [126, 127]. This satisfies the theoretical flame position at the stagnation plane of a counterflow, when the Lewis number effect and the density difference in fuel and air are neglected. In addition, the behavior of a methane flame was studied when the flame was located away from the stagnation plane for $Z_{st} = 0.07$.

Each fuel was diluted with nitrogen to the level required to maintain flame temperature at approximately 2250 K; this value was calculated from the Chemkin-Pro OPPDIF [128] simulation using the USC Mechanism 2.0 [129].

Table 4.1 Experimental conditions for experiment on a DC electric field

Z_{st}	Fuel	L [cm]	U_j [cm/s]	σ [s^{-1}]	Stoichiometric mixture composition (Fuel / O_2 / N_2)	Initial mole fractions: Fuel (X_F)	Initial mole fractions: Oxygen (X_{O2})
0.5	Methane (CH_4)	1	20	40	1 / 2.0 / 5.3	0.222	0.527
	Ethane (C_2H_6)	1	20	40	1 / 3.5 / 8.7	0.147	0.548
	Propane (C_3H_8)	1	10	20	1 / 5.0 / 12	0.111	0.566
			20	40			
			40	80			
		1.5	15	20			
			30	40			
			60	80			
	N-butane (n-C_4H_{10})	1	20	40	1 / 6.5 / 15	0.089	0.574
0.07	Methane (CH_4)	1	20	40	1 / 2.0 / 5.3	1.000	0.274

4.3 Results and discussion

4.3.1 Preliminary test

Flow visualization often requires seeding tracer particles. However, their dynamics can be affected by electric fields, which is an operational principle of an electrostatic precipitator. Therefore, flame behavior and electric current response were compared with and without seeding particles. Photos of propane flames are compared in Fig. 4.1 at V_{dc}= 2.4, 0, and –2.4 kV without (a) and with (b) seeding particles. The height of each image corresponds to the 1-cm separation distance. At V_{dc} = 0 without seeding, the flame (luminous blue zone), was located near the center between the fuel and oxidizer nozzles, which was expected when Z_{st} = 0.5. However, at V_{dc} = 2.4 or –2.4 kV was applied to the lower nozzle, the flame repositioned toward the cathode or the anode, respectively. This result is consistent with previous similar observations (Chapter 3), and with other literature on counterflow flames [94, 95].

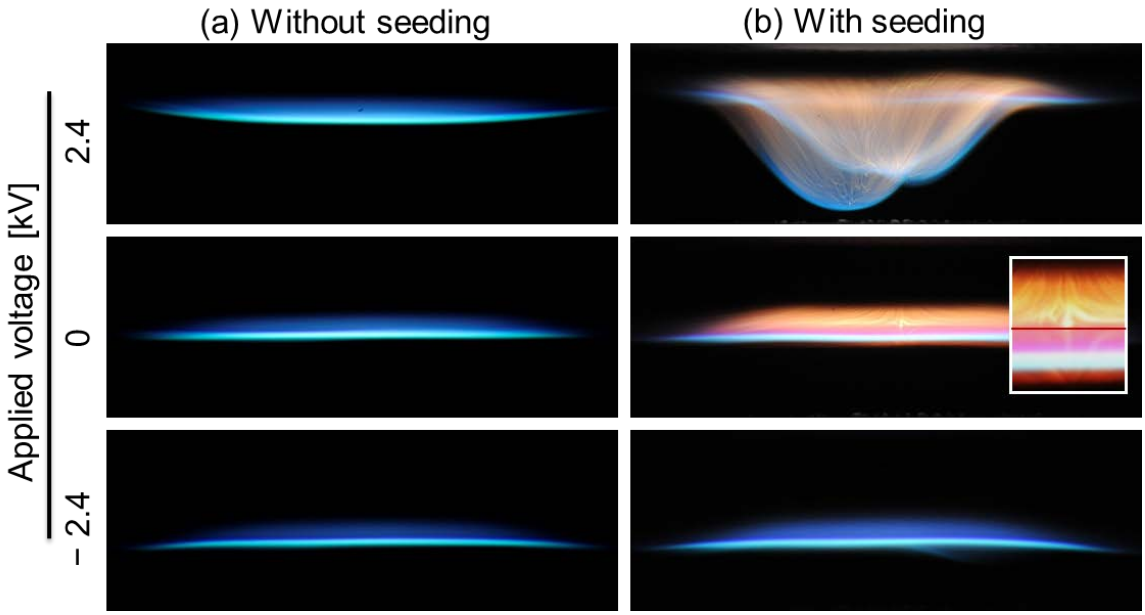

Figure 4.1 Typical flame images of propane flames with Z_{st} = 0.5at V_{dc} = 0, 2.4 and −2.4 kV (a) without and (b) with seeding particles.

When seed particles were added into both streams (Fig. 4.1b), flame size and position of the luminous blue region at V_{dc} = 0 remained similar to streams without seeding. However, with seeding, a luminous yellow region became apparent, which probably represents thermal radiation from seed particles passing through a high temperature reaction zone. The inset shows a closeup of the stagnation plane (marked as a horizontal red line), where seeding particles can be seen radiating from both sides. This photo also indicates that the luminous blue region of the CH chemiluminescence is located slightly toward the fuel nozzle, which is reasonable since both C and H enter the system by way of fuel elements.

The flame with seeding particles at V_{dc} = –2.4 kV also shows negligible differences in terms of flame size or position, while no luminous yellow region is observed. The potential that there will be no seeding particles in this high-temperature reaction zone is discussed in detail in section 4.3.2. Note the instability of the flame with seed particles at V_{dc} = 2.4 kV, showing a highly curved and fluctuating nature, indicating that the interaction between seed particles and the electric field significantly affects the flame.

Figure 4.2 illustrates the relationship between the electric current and applied voltage, emphasizing the difference in the current at high voltage in the presence and absence of seeding particles. Electric current density (I_d) represents the total measured current divided by the projected flame area to a horizontal plane based on the blue luminosity. The area of a circle with a measured diameter of a blue flame was used as the projected flame area.

When the applied voltage was small, in the range of $-1.2 < V_{dc} < 1.3$ kV, the current density increased with increasing voltage for both positive and negative V_{dc} cases. The response in this range was reasonably parabolic; no differences were observed in the presence or absence of seeding particles. This is consistent with a typical electric current in the sub-saturated regime, which (theoretically) depends on the square of electric field intensity [69].

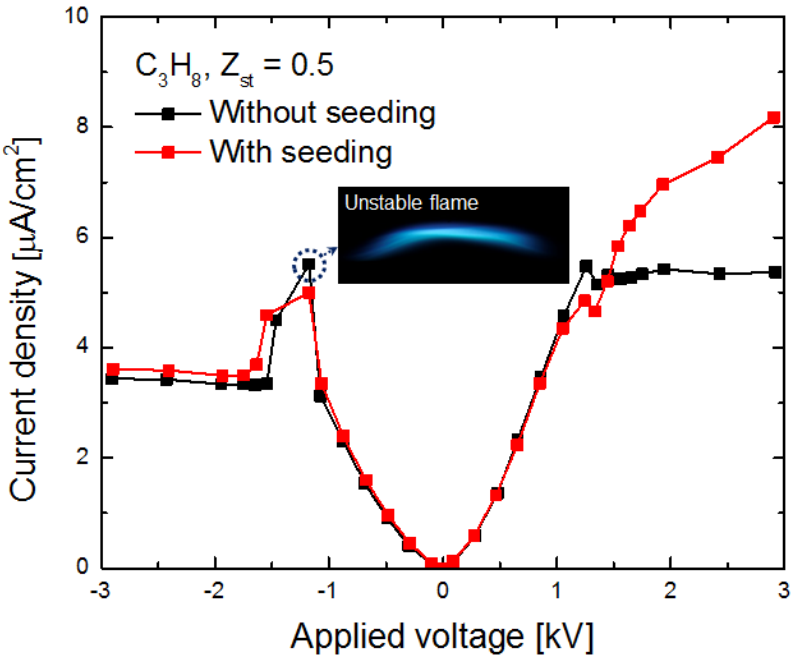

Figure 4.2 Response of current density along the variation of applied voltage with and without seeding particles. Inset indicates unstable flame at V_{dc} = –1.18 kV.

When the electric current equals the generation rate of positive ions (or the sum of the generation rate of electrons and negative ions), it typically becomes saturated with further increased applied voltage [69], since the generation rate of charged species sets a limit to the maximum current. At V_{dc}< –1.6 kV, a saturated current density of approximately 3.4 μA/cm^2 was observed in the flame without seeding particles. The local peak in current density, between –1.6 <V_{dc}< –1.2 kV, was attributed to the larger surface area of the unstable flame, which fluctuated radially and axially in a random manner (Fig. 4.2 inset). The current saturated at about 5.3 μA/cm^2 when positive voltages were applied to the flame (at ~ 1.4 kV). The difference in the saturated current

density due to polarity implies that ion generation in the flame depends on the direction of the electric field with respect to the fuel-oxidizer flow.

With seeding particles, when V_{dc} < 1.3 kV, less than 5% difference was observed from the saturated currents without seeding; however, when V_{dc} > 1.3 kV, the current density continued to increase well above the saturation point of the flame without seeding particles. Similar to the local peak in current density, this may be explained by the increased flame surface area of the unstable flame, shown in Fig. 4.1b at V_{dc} = 2.4 kV. (Recall that the current density is calculated based on the projected flame area to a horizontal plane.)

Explaining this unexpected effect of the seed particles on flame characteristics with applied DC is beyond the scope of this study; but it would be an interesting avenue for future study. However, considering this effect, only negative applied voltage is considered in this investigation of the flow field with seeding particles.

4.3.2 Flow visualization and ionic wind

The Mie scattering images in Fig. 4.3 illustrate the pathlines of the seed particles using a sheet beam of Ar-ion laser for the propane nonpremixed flame (0.1 s exposure time). With no applied electric field (a), the pathlines of the flame clearly show a typical counterflow field with a stagnation plane at the center. As noted previously, the yellow luminosity near the stagnation plane represents thermal radiation from the seeding

particles, and the luminous blue zone is slightly below the stagnation plane toward the fuel (cathode) nozzle.

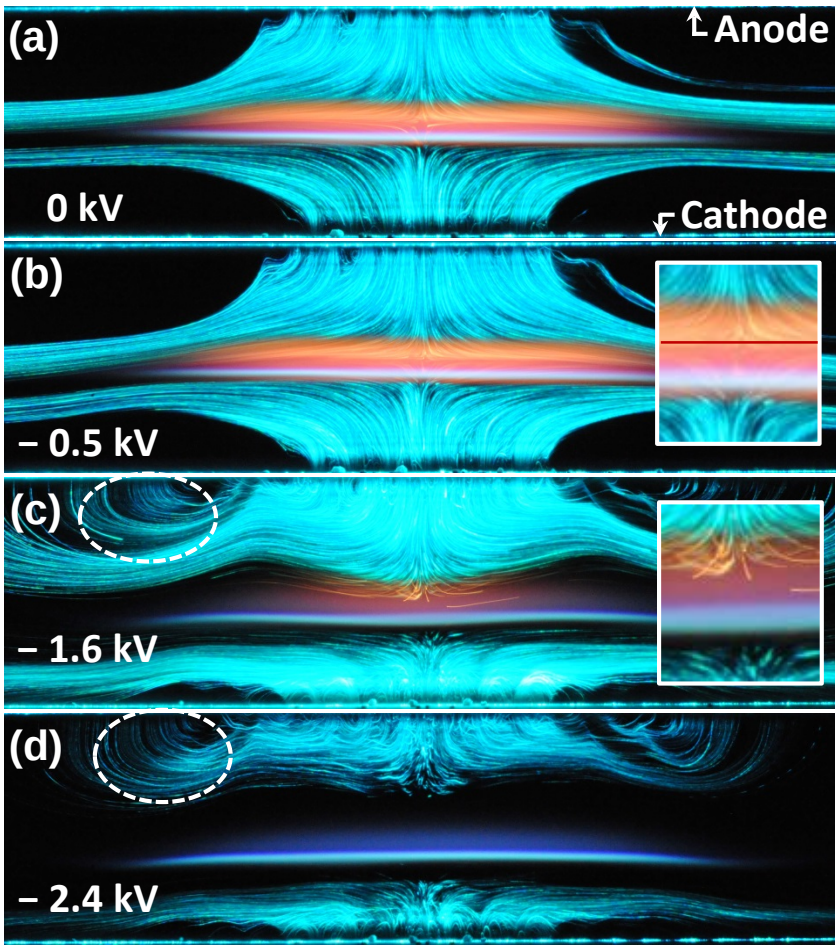

Figure 4.3 Mie scattering images showing the pathlines of seeding particles with flame luminosities for selected applied voltages of propane flames at Z_{st} = 0.5: (a) 0 kV, (b) −0.5 kV, (c) −1.6 kV, and (d) −2.4 kV.

At V_{dc} = –0.5 kV (Fig. 4.3b), no change in flame position or flow pattern was observable from those of the baseline flame, with the exception of a region which was radially farther from the edge of the flame, where the pathlines bend slightly toward the cathode (lower nozzle). This may be attributed to a net body force (Lorentz force), acting on a flow volume because there are more positive than negative ions. However, any effects of electric fields on the flow field and the flame at this point seem to be weak because no noticeable modifications up to V_{dc} = –1.1 kV were observed in the sub-saturated regime.

After the unstable regime, a drastic change was observed in the flow field, where the flame re-stabilized at V_{dc} = –1.6 kV (Fig. 4.3c) and relocated toward the cathode (fuel). A dark region, with no scattering signal from seeding particles in the proximity of the flame, became evident and expanded toward both the cathode and anode as the voltage reached V_{dc} = –2.4 kV (Fig. 4.3d). This dark zone was attributed to a bidirectional ionic wind blowing both up and downwards from the flame and caused by the relative movements of the ions--positive ions toward the cathode and negative ions toward the anode. However, because seed particles may also be charged, and therefore influenced by the electric field, as mentioned previously, care must be taken to validate that bidirectional ionic winds are present.

For example, the pathlines in the dashed ovals in Figs. 4.3c and d deflect vertically toward the anode; although TiO_2 particles are generally non-conductive, this behavior could imply the presence of seeding particles that have been charged by electron and ion attachment [130]. Charged seeding particles are affected not only by flow motion but also

by the Lorentz force acting on them. Even in the central region of nozzle exits, deflected pathlines were observed pointing back toward the nozzles at $V_{dc} = -2.4$ kV, as seen by comparing Figs. 4.3a or b. Several other types of seeding particles were tested, such as diamond, olive oil mists, and di-ethyl-hexyl-sebacat ($C_{26}H_{50}O_4$), but all demonstrated the interference of this electrostatic effect. Thus, there is no guarantee that the pathlines in Fig. 4.3 represent related flow fields exclusively.

To determine whether the flow fields were caused by electric fields alone, it was necessary to visualize the dark zone, which required that particles be seeded into it. In place of TiO_2 particles, titanium tetraisopropoxide (TTIP) was used in an effort to create a reactive Mie scattering of the dark zone. This approach was unsuccessful because TTIP reacted with water vapor to form particles even before reaching the flame zone. A forced seeding approach was adoped next, in which TiO_2 particles were injected through a small quartz tube, as described in the experimental section. However, insertion of the tube and the nitrogen flow used to carry seeding particles disturbed the original flow field; thus only qualitative visualization was available to confirm the flow pattern in this zone.

The quartz tube carrying seeding particles was inserted near the burner axis, perpendicular to the Ar-ion laser sheet beam, which illuminated a vertical cross-section at the burner center (Fig. 4.4a). With the nonpremixed propane flame at $V_{dc} = -2.4$ kV, when the tube was located above the luminous blue flame, all seeding particles drifted upwards (Fig. 4.4b), but when the tube was positioned 0.8 mm lower, closer to the flame, particle movements were clearly identifiable in both directions (Fig. 4.4c). Meanwhile, when the tube was moved 0.8 mm further lower, slightly below the flame, seeding

particles only moved downward (Fig. 4.4d). The relative distance between the positions of the tube in the respective images (b to d) was chosen to be 0.8 mm, equivalent to the inner diameter of the tube. This indicated that the coexisting region of both positive and negative ions be approximately 0.4 mm from the visible luminous blue flame front toward the oxidizer.

Finally, Fig. 4.4e clearly demonstrates double-stagnation planes caused by a bidirectional ionic wind. This image superimposed two separate images; 1) a multi-exposed image of scattered laser from seeding particles injected from the small tube by horizontally translating it, and 2) a scattering image of seeding particles from both nozzles, removing the inserted small tube. The formation of two stagnation planes by the bidirectional ionic wind was identified as two interfaces between the particles from the nozzles and those injected by the small inserted tube.

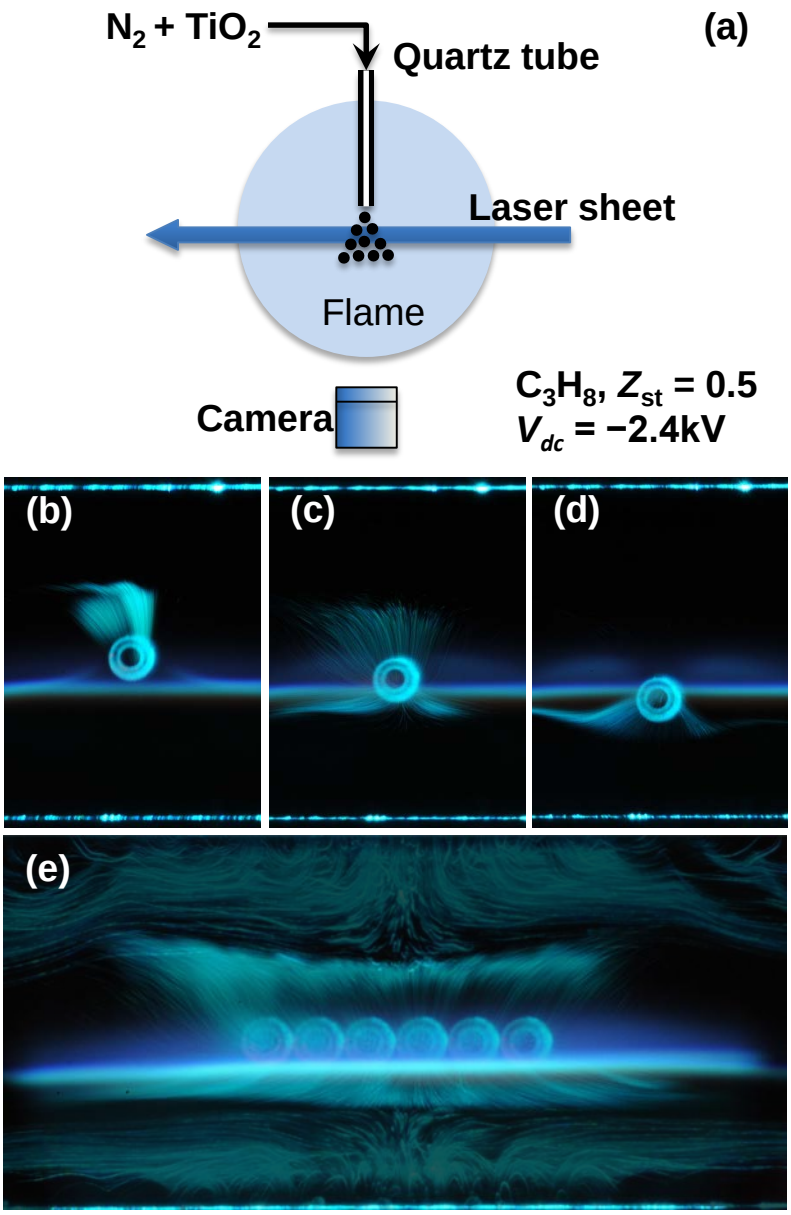

Figure 4.4 Flow visualization in the dark zone by inserting a quartz tube to inject seeding particles into a reaction zone containing a vertical sheet laser: (a) perpendicular configuration of seeding jet and laser, (b) seeding above a luminous blue flame, (c) seeding near the flame, (d) seeding below the flame, and (e) multi-exposure image together with seeding particles from the nozzles. (b), (c), and (d) were 0.8 mm apart.

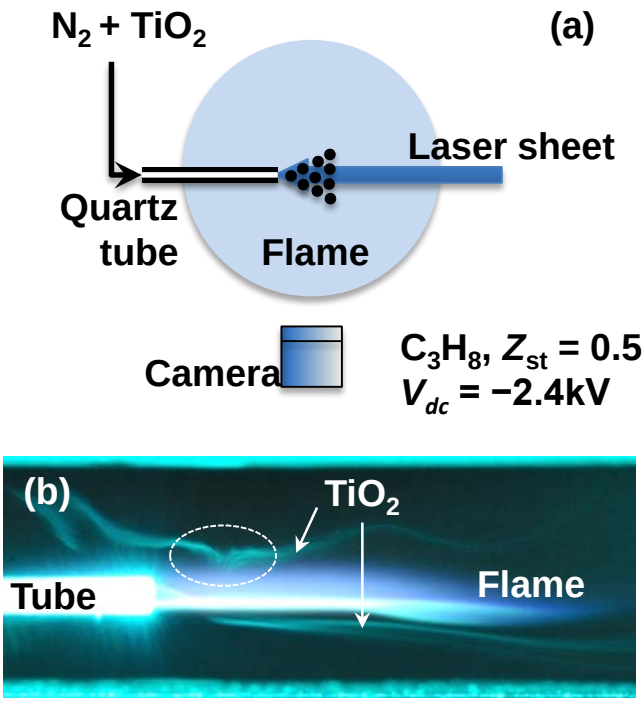

Figure 4.5 Flow visualization in the dark zone by inserting a quartz tube to inject seeding particles into the reaction zone with a vertical sheet laser: (a) parallel configuration of seeding jet and the laser and (b) pathline visualization.

To further clarify the bidirectional ionic wind, the tube was adjusted to be parallel to the laser sheet and fixed in the same vertical position as in Fig. 4.4c (as shown in Fig. 4.5a). The pathlines in Fig. 4.5b, separating above and below from the flame, evidence the existence of the bidirectional ionic wind. Another flow separation presents as two opposing radial pathlines inside the dashed oval in Fig. 4.5b, implying that a stagnation plane exists against the oxidizer stream injecting from the upper nozzle. Therefore, it can be confirmed that the dark zone is a result of the bidirectional ionic wind blowing from the reaction zone toward both the cathode and the anode.

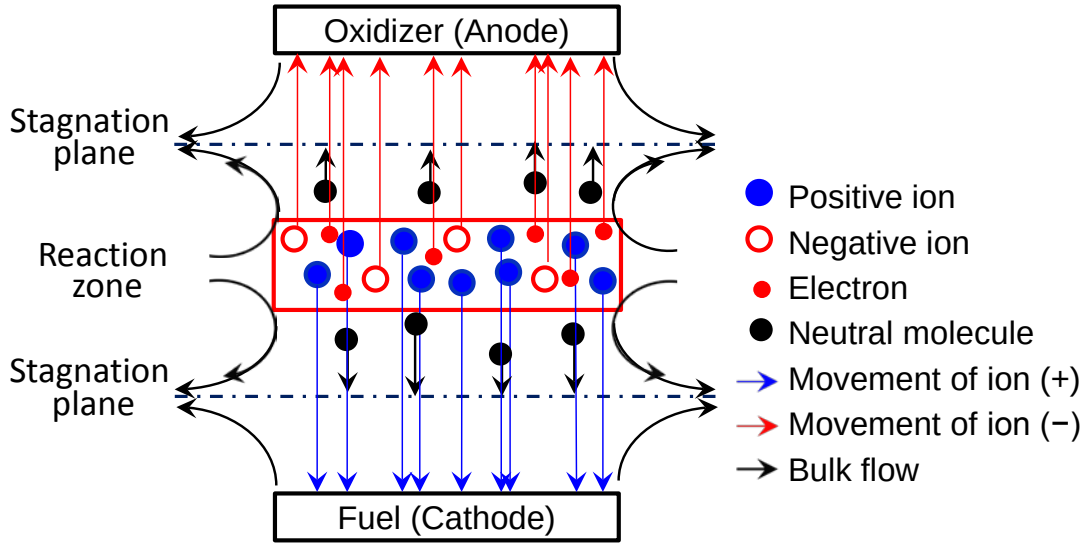

Figure 4.6 Schematic of flow modification due to ionic wind.

Figure 4.6 schematically displays a mechanism for the flow modification shown in Fig. 4.4e. Positive ions, such as H_3O^+, $C_3H_3^+$, CH_3^+, and CHO^+; negative ions, such as O_2^-, OH^-, O^-, CHO_2^-, CHO_3^-, and CO_3^-, and electrons, are present in the hydrocarbon flame zone [87-89]. When these charged particles were subjected to an electric field (lower potential to the lower nozzle), positive ions accelerated toward the cathode and negatively charged particles (negative ions and electrons), accelerated toward the anode. The momentum transfer from the accelerated ions to neutral molecules generated a bulk flow motion (ionic wind). Although the negligibly small mass of electrons negated their direct contribution to the ionic wind, their attachment to other species (particularly oxygen containing species), increased the number of negative ions.

As a result, a reaction zone became a source of flows in both up and downward directions. To satisfy overall mass conservation, there must be a radially entrained flow

to the reaction zone, as depicted in Fig. 4.6. This ionic wind in both directions created a new stagnation plane with a corresponding main counterstream. Thus, a double-stagnant flow field with bidirectional ionic wind from the reaction zone was found to be a typical pattern at relatively high voltage in the counterflow burner, as shown in Figs. 4.4 and 4.6.

This drastic modification in flow field caused significant changes to the stoichiometric axial location and strain rate at the flame, factors that are important for characterizing a nonpremixed flame in a counterflow burner. Note that related variations in OH radicals and sooting characteristics were previously reported in Chapter 3. A numerical approach, including detailed chemi-ionization and the body force due to an electric field, is needed in the future to further investigate the effect of flow field modifications on flame characteristics.

4.3.3 Flow separation and response of the ion current

Movement of charged species under an electric field creates both an electric current (Fig. 4.2) and a bidirectional ionic wind. To understand the phenomenological relationship between these two, the axial positions of a luminous blue flame and stagnation plane(s) were co-plotted (as measured from the lower nozzle), together with the measured electric current for the propane flame in Fig. 4.7.

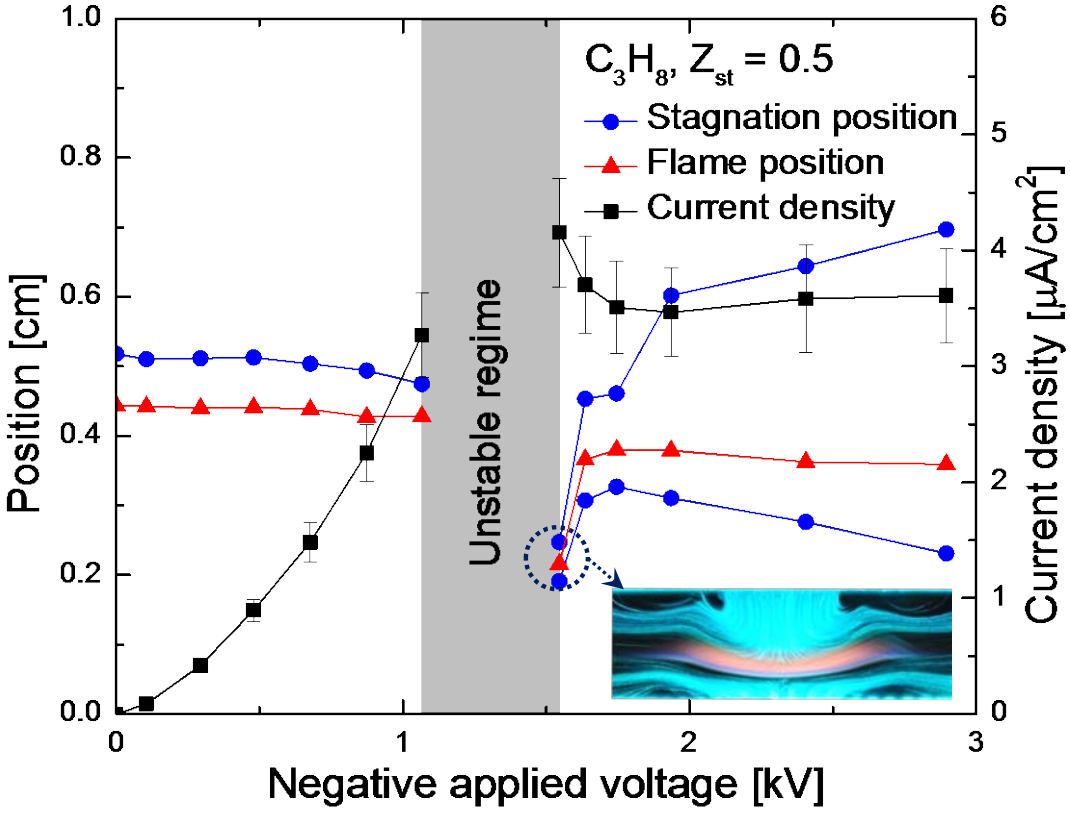

Figure 4.7 Axial locations of the flame and the stagnation plane(s) and current density for a propane flame with a negatively applied voltage at Z_{st} = 0.5. Inset indicates a flame and flow field at V_{dc} = 1.55 kV.

Figure 4.7 shows that when $|V_{dc}| < 0.5$ kV, flame and stagnation plane locations were unaffected by the applied voltage, behavior that is consistent with observations in various flame configurations under an electric field [34, 42, 75], where threshold voltages are necessary in order to have an effect on a flame. Although the flame position changed slightly when $-1.2 < V_{dc} < -0.5$ kV, the stagnation plane began to move toward the fuel nozzle. After the unstable regime, the flame remained briefly at about 2 mm above the

fuel nozzle at V_{dc} = −1.55 kV. The flame was convex toward the fuel nozzle and two separated stagnation planes existed above and below it (inset of Fig. 4.7). The flame quickly restabilized at its new position at around 3.8 mm from the nozzle, when the negative voltage increased slightly and the flame adopted a near-planar shape (Fig. 4.3c). In the flame restabilization regime, both upper and lower stagnation planes moved away from the flame with increasing negative voltage. This indicates that the velocity of the ionic wind (momentum) was increased due to increased field intensity because the terminal velocity of ions was proportional to the field intensity ($\sim \mu E$), as previously discussed. Note that the restabilized flame reasonably maintained its location regardless of voltage.

By comparing the onset of flow separation with the trend of the measured current density, it noted that, in the saturated regime, when the flame restabilized in a new position at $|V_{dc}| > 1.6$ kV, current density also remained stable (saturated regime). The conclusion was that the unstable regime was the result of a hydrodynamic instability caused by a competition between the main jet streams and ionic wind. As voltage increased (increasing ionic wind velocity), flow separation occurred, resulting in a double-stagnant flow configuration. This in turn caused the flame to re-stabilize and the current density to reach saturation.

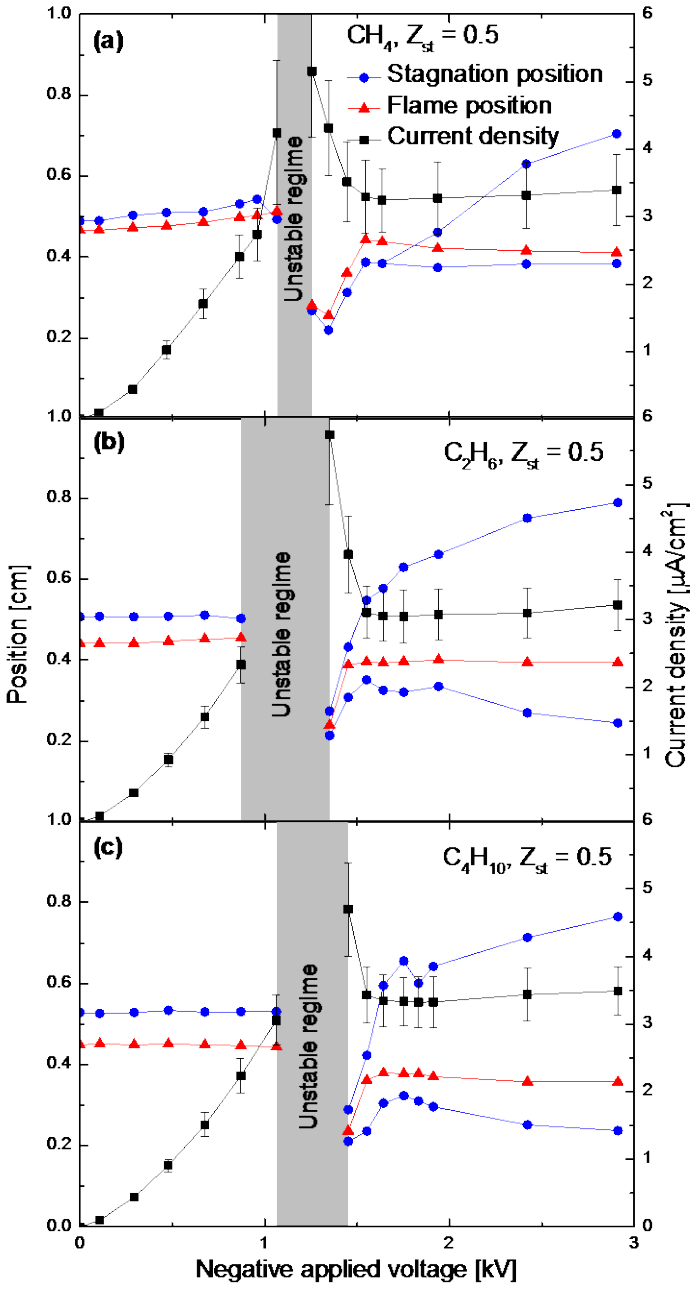

Figure 4.8 Axial locations of the flame and the stagnation plane(s) and current density for (a) methane, (b) ethane, and (c) n-butane flames with Z_{st} = 0.5 at a negatively applied voltage.

Still to be resolved, is an understanding of the underlying causality between flow separation and saturated current density or evidence to suggest these two events take place independently at a similar voltage. To investigate the potential for a relationship between the two, methane, ethane, and n-butane flames were tested. Jet velocity was held constant at 20 cm/s and all flames were located near the central stagnation plane (Z_{st} = 0.5), similar to propane (Table 4.1). Saturated current densities for all fuels tested were between 3.1 and 3.6 μA/cm^2 (Fig. 4.8), similar to that of the propane flame. Figure 4.8 demonstrates that the voltage range of the unstable regime varies with the fuel, implying a fuel-dependent factor. Overall, the current saturation and flow separation of ethane and n-butane flames immediately after the unstable regime (V_{dc} = –1.35 kV and V_{dc} = –1.45 kV, respectively), were similar to those of the propane flame. The flow separation of the methane flame exhibited late onset at V_{dc} = –1.9 kV after the end of its unstable regime (V_{dc} = –1.26 kV), indicating a lack of connection between current saturation and flow separation. To provide a complete explanation of related physical mechanisms between fuel-dependent flame re-stabilization and steady flow separation, detailed studies of multi-dimensional simulations with up-to-date chemi-ionization will be necessary in the future.

To summarize these behaviors in terms of mean electric field intensity, $E = V_{dc}/L$, and strain rate, $\sigma = 2U_j/L$; various strain rates, σ = 20, 40, and 80 s^{-1}, were examined for two different L (1 and 1.5 cm), as shown in Table 4.1. The baseline composition—$C_3H_8/O_2/N_2$ system with Z_{st} = 0.5—was considered.

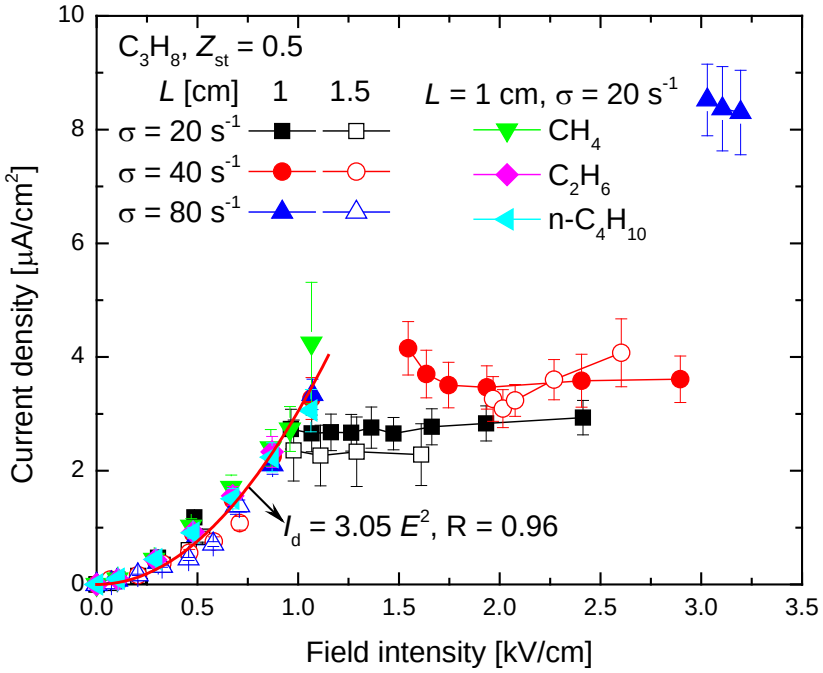

Figure 4.9 Electric current responses of flames with various strain rates (σ = 20, 40, and 80 s^{-1}), and separation distances (L = 1 and 1.5 cm) for a propane mixture. For the sub-saturated regime, other tested fuels (methane, ethane, and n-butane) in Fig. 4.8 were also included for comparison. Note that negative DC was applied to the lower (fuel) nozzle and field intensity = V_{dc}/L.

Figure 4.9 shows the trends of current density with increasing field intensity for various L and σ. For the sub-saturated regime, the data for other tested fuels shown in Fig. 4.8 were also included. As illustrated in the figure, the measured current densities show good agreement, displaying quadratic increase with the mean electric field intensity, regardless of fuel, strain rate, and the burner separation. A general correlation

of the current density (I_d) in counterflow, nonpremixed flames can be expressed as I_d = 3.05(nA/V-cm)E^2 with a correlation coefficient R = 0.96, when a flame initially stabilizes at the center of the gap. This global trend is consistent with previous theoretical studies [69] reporting that current density in the sub-saturated regime is controlled by electric field intensity (~E^2), irrespective of the concentrations of charge carriers. Noting that, however, this should differ by a relative location of flame between two electrodes [79].

Meanwhile, the saturated current density increased with more strain rate. Corresponding saturated current densities were ~2.6, ~3.6 and ~8.3 μA/cm^2 for σ = 20, 40, and 80 s^{-1}, respectively. Noting that a saturated regime for σ = 80 s^{-1} at L = 1.5 cm could not be observed due to an electrical breakdown (arcing). A critical field intensity for a saturation of current density increased as the strain rate became higher; but due to the unstable nature of flames near the critical moment, a quantitative comparison could not be performed. Because a saturated current density was limited by a rate of charge production, increased saturated current density caused by greater strain rates indicated an enhanced rate of charge production in the unit volume. This dependence of current density on strain rate should be explained with detailed numerical calculations.

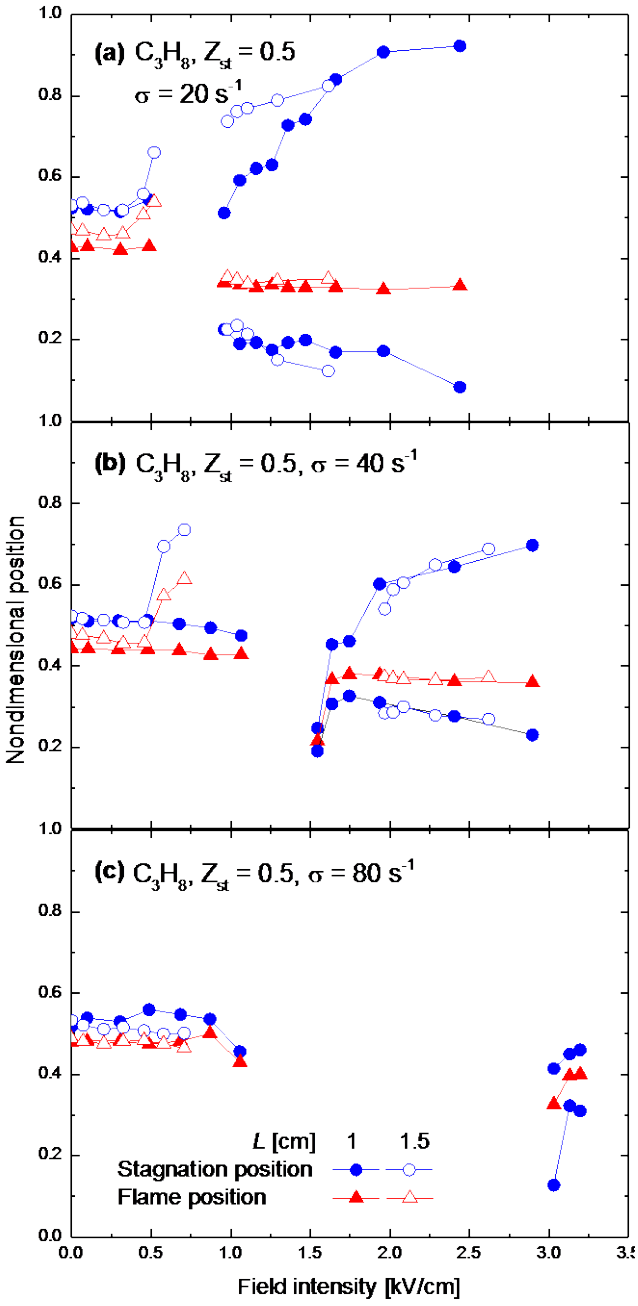

Figure 4.10 Characteristics of nondimensional positions (x/L) of flames and stagnation planes along the field intensity (V_{dc}/L), with propane flames for various strain rates (a) 20, (b) 40, and 80 s^{-1}at Z_{st} = 0.5 and L = 1 and 1.5 cm. (Note that a negative DC was applied to the lower fuel nozzle.)

Nondimensional positions of flames and stagnation planes, which were normalized by the separation distance (L), were also analyzed for each strain rate; their results were illustrated in Fig. 4.10 with respect to the mean electric field intensity. General behaviors were similar to the baseline condition (Fig. 4.7), showing less sensitivity to E in the sub-saturated regime followed by a certain range of the unstable flame and in the saturated regime restabilization of a flame position, which was accompanied by a modified flow field with double stagnation planes. Although there was some deviation in flame position, and a stagnation plane at L = 1.5 cm for σ= 20 and 40 s^{-1} in the sub-saturation regime, the flow and flame behaviors can be characterized in terms of nondimensional positions and E for each strain rate. It is evident that stronger E is required for a higher strain rate in order to obtain comparable effects of electric fields on flow and flame behaviors.

4.3.4 Semi-quantitative measurement of the flow field

The experiments described above were conducted with Z_{st}= 0.5; all tested flames were located near the stagnation plane, where the axial flow velocity was very small. This design maximized the effect of the bidirectional ionic wind on a flow field.

Difficulties in seeding particles into the flame prevented quantitative measurements using PIV in the dark zone. To quantify an entire flow field in the presence of the bidirectional ionic wind, a qualitative flow structure was considered first. Figure 4.11 shows a schematic of flow velocities in the counterflow burner. An original flow field was assumed as a simple linear velocity profile (blue line), with a stagnation plane at the

center and uniform bidirectional ionic wind profiles (red line), blowing from the flame toward both nozzles. A modified velocity profile (green line) is a vector sum of these two components. Note that the value is positive in the cathode to anode direction and negative in the anode to cathode direction. Figure 4.11a represents the qualitative flow field, when the flame is located at the stagnation plane (Z_{st} = 0.5), as discussed previously, where the modified flow field is double stagnant.

Because the location of the flame and the magnitude of the ionic wind determine the pattern of flow modification, if the flame is sufficiently relocated toward the anode and the original velocity profile is maintained (Fig. 4.11b with $Z_{st} \ll 0.5$), a shift of the stagnation plane without flow separation may occur. Discontinuity in a modified velocity at the flame is due to the uniform step assumption of ionic wind. Based on this simple prediction, which states that there will be no flow separation with a sufficiently small Z_{st}, in order to effectively seed the particles into a flame zone under the effect of ionic wind, it was necessary to move the flame farther from the stagnation plane.

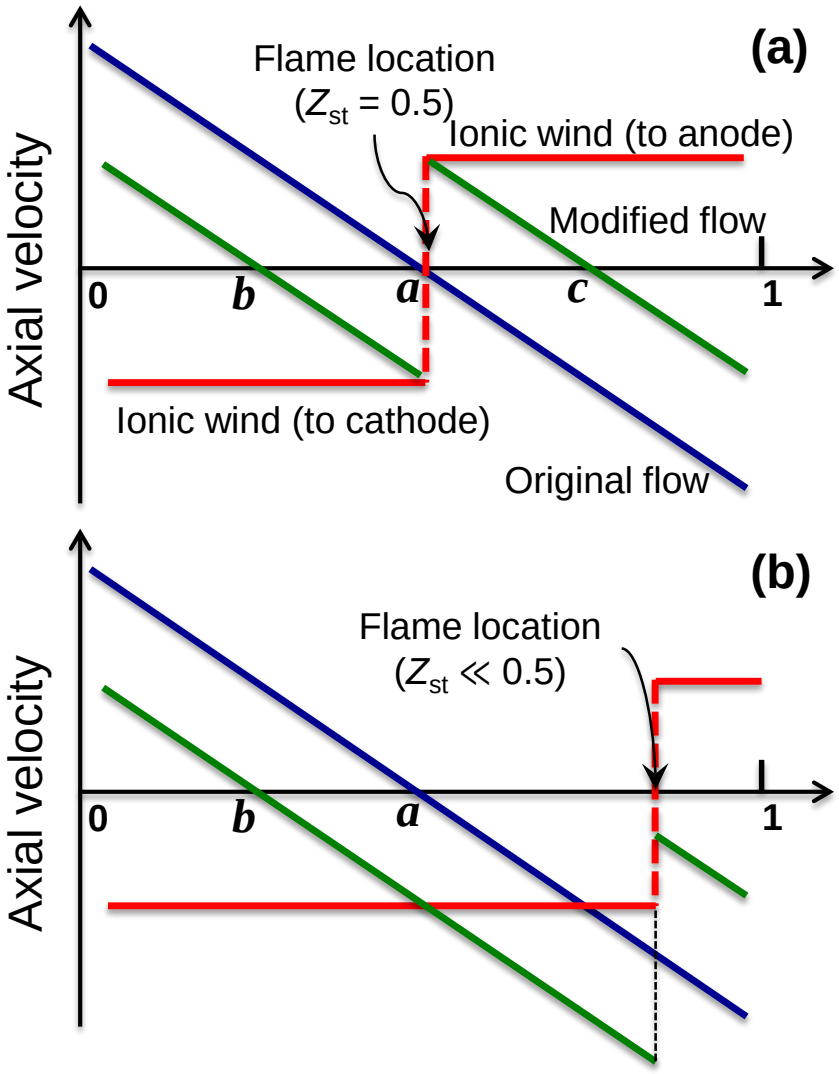

a: original stagnation plane
b, c: new stagnation planes
Modified flow (G) = Original flow (B) + Ionic wind (R)

Figure 4.11 Schematic of flow modification with a bidirectional ionic wind in a counterflow geometry: (a) Z_{st} = 0.5 and (b) $Z_{st} \ll 0.5$.

Thus, the methane flame was moved toward the anode by changing Z_{st}= 0.07, while maintaining the flame temperature corresponding with Z_{st}= 0.5 (conditions in Table 5.1).

Note that the propane flame continued to exhibit flow separation at Z_{st} = 0.08. Figure 4.12a shows the pathlines of seeding particles from both nozzles with no electric field. There is an obvious upward relocation of the flame above the stagnation plane. Note that because a sooting flame forms at this flow and under these mixture conditions, the luminous yellow zone is indicative of thermal radiation from both seeding and soot particles.

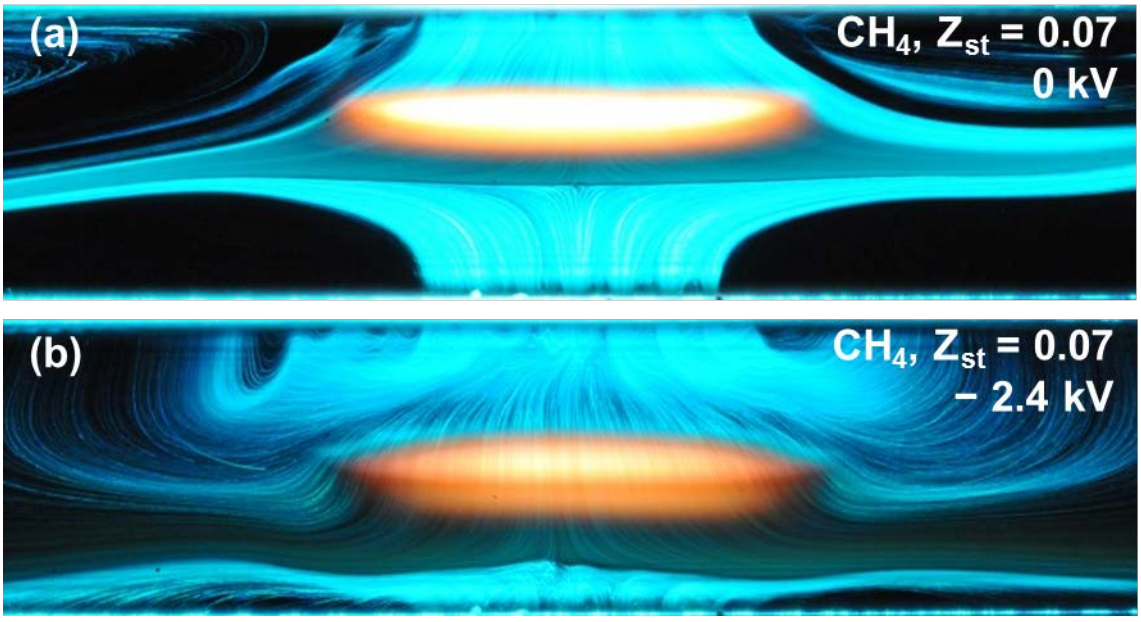

Figure 4.12 Visualization of flame luminosity and particle pathlines for methane flames at Z_{st} = 0.07 with (a) no electric field and (b) V_{dc} = −2.4 kV.

At V_{dc} = – 2.4 kV (Fig. 4.12b), both the flame and the stagnation plane moved down toward the cathode. Here, only one stagnation plane was observed, demonstrating an absence of flow separation, as schematically predicted in Fig. 4.11b. The upward ionic momentum may decelerate the unburned oxidizer stream above the flame, while the downward ionic momentum pushes the stagnation plane closer to the fuel stream.

Near the anode, where the radial location was greatest, most of the pathlines were deflected toward the upper nozzle, driven by the electrostatic force on charged seeding particles. This explains why velocity could not be quantified using PIV. However, because the seeding particles permitted visualization of a full flow field, we attempted to quantitatively determine axial velocity along the centerline.

Figure 4.13 illustrates the results from the PIV of the axial velocity along the flow axis atV_{dc} = 0 and –2.4 kV, corresponding to those in Fig. 4.11. The data near the burner exits (~ 1mm) was excluded because of uncertainties arising from a reflection of the laser beam and a wake by the perforated plates. At V_{dc} = 0, a monotonic decrease in the velocity of the fuel stream toward the stagnation plane was found, while the velocity increased at the oxidizer end due to thermal expansion by the flame. A clear shift of the stagnation plane from 4 mm to 2 mm above the cathode was evident atV_{dc} = –2.4 kV, and a deceleration of the oxidizer stream in an axial location of 4–9 mm above the cathode also confirmed the existence of an upward ionic wind, as explained previously. , Due to a non-uniform ionic wind velocity, this had the potential to significantly decrease velocity near the flame, unlike the assumption in Fig. 4.11.

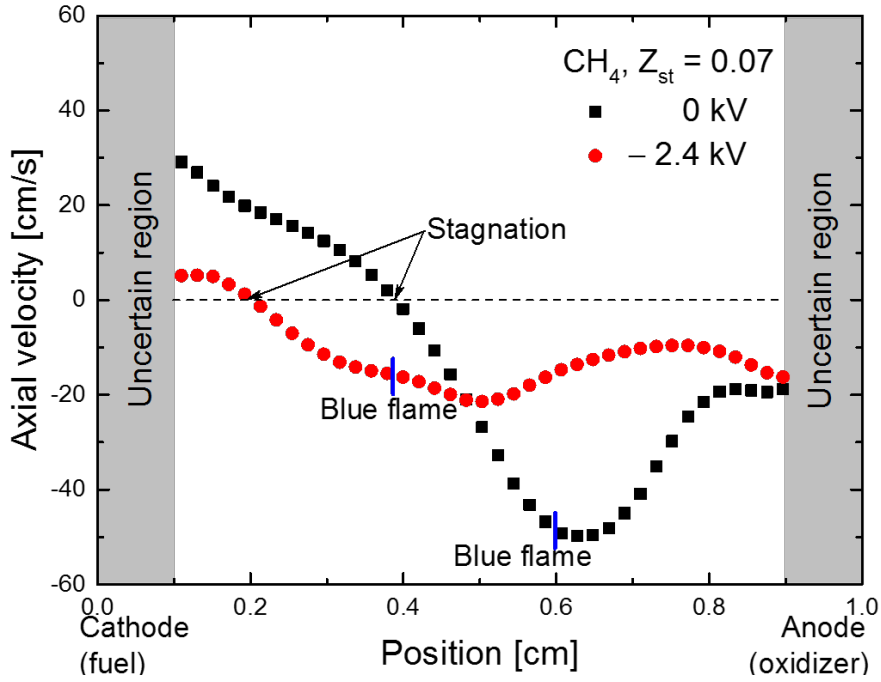

Figure 4.13 Results of a PIV of axial velocity along the flow axis for methane flames at Z_{st} = 0.07 with V_{dc} = 0 and −2.4 kV.

PIV results are presented in Fig. 4.14 only for the zones with seeding particles, even though there was a dark zone for the baseline flame at V_{dc} = –2.4 kV (Fig. 4.3d). The axial velocity profile along the flow axis at V_{dc} = 0 clearly shows a typical velocity pattern in a counterflow geometry; velocity increased near a thermal expansion region caused by a flame and dropped quickly to form a stagnation plane. For the case at V_{dc} = –2.4 kV, two separated stagnation points can be clearly identified, as conceptually predicted in Fig. 4.11a. To fully understand these flow fields, a comprehensive simulation with detailed chemi-ionization will be necessary. Note that to obtain ionic wind in a

simulation, at least a two-dimensional domain must be used to generate the necessary balance of flow in the momentum equation.

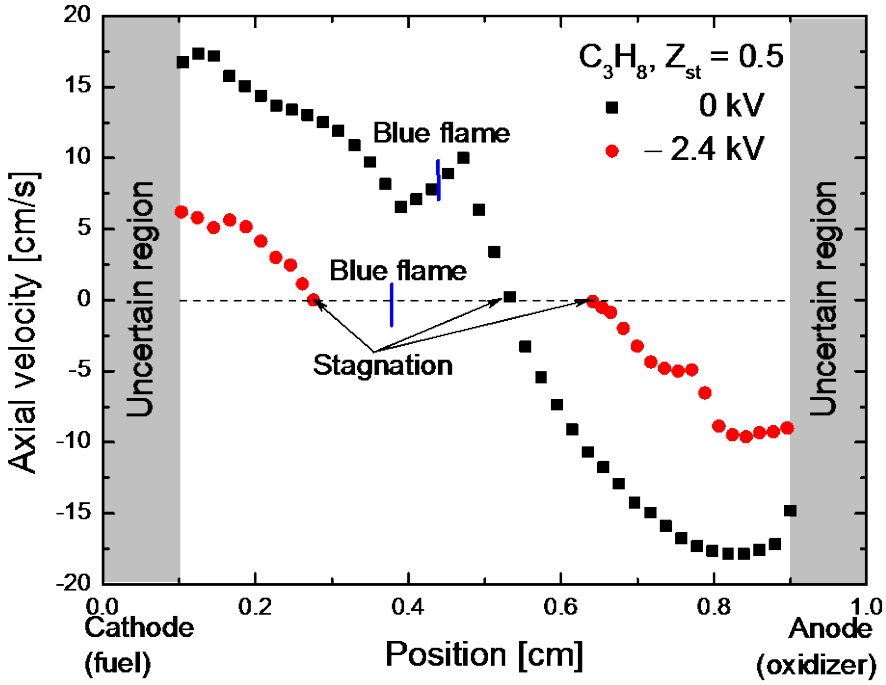

Figure 4.14 Results of a PIV of axial velocity along the flow axis for propane flames at Z_{st} = 0.5 with V_{dc} = 0 and −2.4 kV.

4.4 Summary

The effects of DC electric fields on nonpremixed counterflow flames, emphasizing flow modifications caused by bidirectional ionic wind, were experimentally investigated. An external electric field separated positive and negative ions away from the reaction zone toward the cathode and the anode, respectively, creating a bidirectional ionic wind. A complete flow field was successfully visualized, including the existence of the bidirectional ionic wind; drastic flow separation was found at the reaction zone, resulting in a double-stagnant flow field when the flame was located near an original stagnation plane. However, when the flame was relocated toward the anode, increased momentum pushed the original stagnation plane toward the cathode and no flow separation was observed.

It was also found that an overshot of measured electric current density occurred due to an ionic-wind-induced hydrodynamic instability, this was followed by a restabilization of the flame toward the cathode and a saturation of the current density. Restabilization appeared to have a relationship with flow separation; however, investigation failed to detect consistency between the tested fuels. Investigation into the related causalities, and a detailed flame structure with a double-stagnant flow field, should be presented in a comprehensive simulation including ion-chemistry and ionic wind.

Chapter 5

STUDY OF A DC ELECTRIC FIELD ON FLAME AND FLOW IN PREMIXED BUNSEN FLAME

5.1 Background

In Chapter 4, an ionic wind with a nonpremixed flame in a counterflow burner applying a DC electric field was successfully visualized. As a result, it was found that ionic wind blew in both directions toward a cathode and an anode due to the respective movement of positive and negative ions. Therefore the present study aims to visualize and understand a flow field modification in a premixed flame in a Bunsen burner. When an electric field is applied in a radial direction, a pre-existing baseline flow field (which has a negligible radial velocity component), may show significantly discernable modification in the radial direction. With this motivation, methane/air premixed flame with two parallel electrodes was studied experimentally by applying DC electric field emphasizing visualization of ionic wind. The detailed characteristics of the flame and ionic wind are discussed in this chapter.

5.2 Experimental conditions

The experimental setup consisted of a fuel nozzle, a power supply, and flow visualization systems, as shown in Fig. 5.1. A quartz tube with 0.8-cm inner diameter and 1.0-cm outer diameter was used as the fuel nozzle to avoid interference with externally applied electric fields. To apply electric fields to a flame stabilized on the rim of the tube, two disk-shaped electrodes were placed at locations radially apart from the axis of the tube, with a separation distance of 6.0 cm. The tube was located at the center of the gap between electrodes. The disk-shaped electrode was made from stainless steel mesh screen, so that electrically-driven flow could freely penetrate.

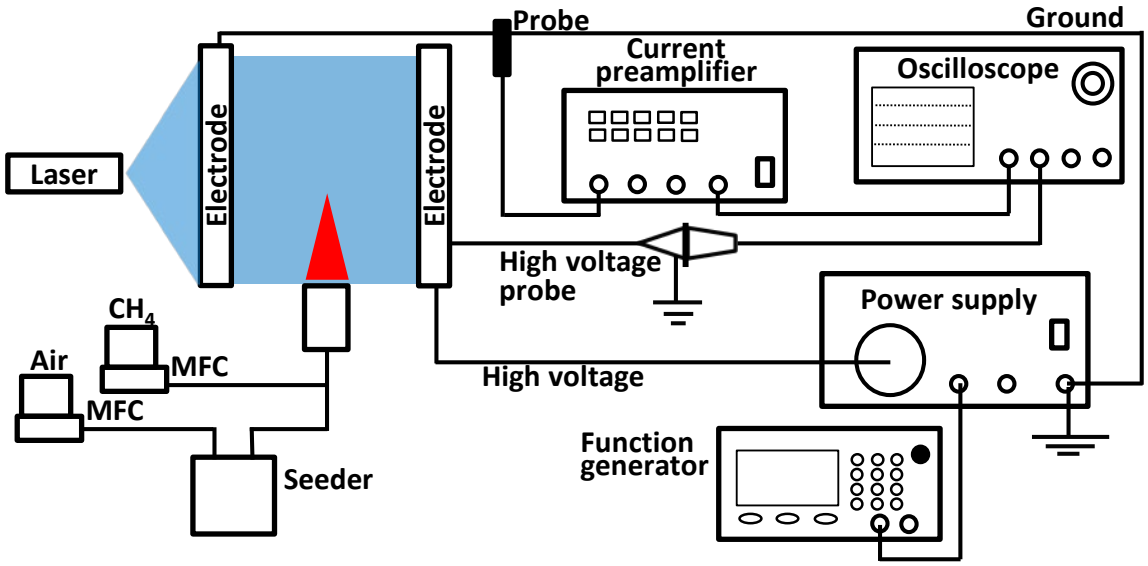

Figure 5.1 Experimental setup for premixed Bunsen flame under DC electric field.

A mixture of methane (CH_4), and air with an equivalent ratio of 1.0 was used to form a premixed flame. A flow rate of the mixture was 30 cm^3/s, so that a mean jet velocity became 60 cm/s, higher than a laminar burning velocity (~ 40 cm/s), in order to avoid flashback. The flow rates of gases were maintained using mass flow controllers (MKS, 11779A).

A power amplifier applied a high voltage to the disk-shaped mesh electrode located on the side, and the amount of the applied voltage, V_{dc} (up to ±10.0 kV). The other electrode was grounded, so that an orthogonal electric field to the main direction of the mixture jet could be applied.

For flow visualization and quantification, a Mie scattering of seeding particles and a particle image velocimetry (PIV) were adopted, respectively. Note that there was a slit (3-mm width and 55-mm height) at the center of each mesh-electrode to accommodate an access of a sheet beam. By controlling exposure time of the camera, flow field visualization, with appropriate lengths of pathlines, could be obtained.

5.3 Result and discussion

5.3.1 Overall response of flames with electrical current

Figure 5.2 shows the variation of premixed Bunsen flame at selected applied voltages. As shown in a baseline flame with no electric field, a typical Bunsen flame exhibiting an axisymmetric conical shape was observed. When $V_{dc} = -5$ kV was applied, the tip of the flame moved slightly to the right, indicating a slanted conical shape toward

a cathode (lower potential); however a base of flame attached to the nozzle rim seemed to be unaffected. As increased voltage was applied, at −10 kV, a distortion of the flame became pronounced. When positive voltages were applied to the high voltage electrode, it was found that the flame tip moved to the ground electrode--to a lower potential side--as in cases with negative applied voltages. As illustrated in Fig. 5.2, the flame morphology at V_{dc} = 5 and 10 kV was a mirror image of that of V_{dc} = −5 and −10 kV, respectively.

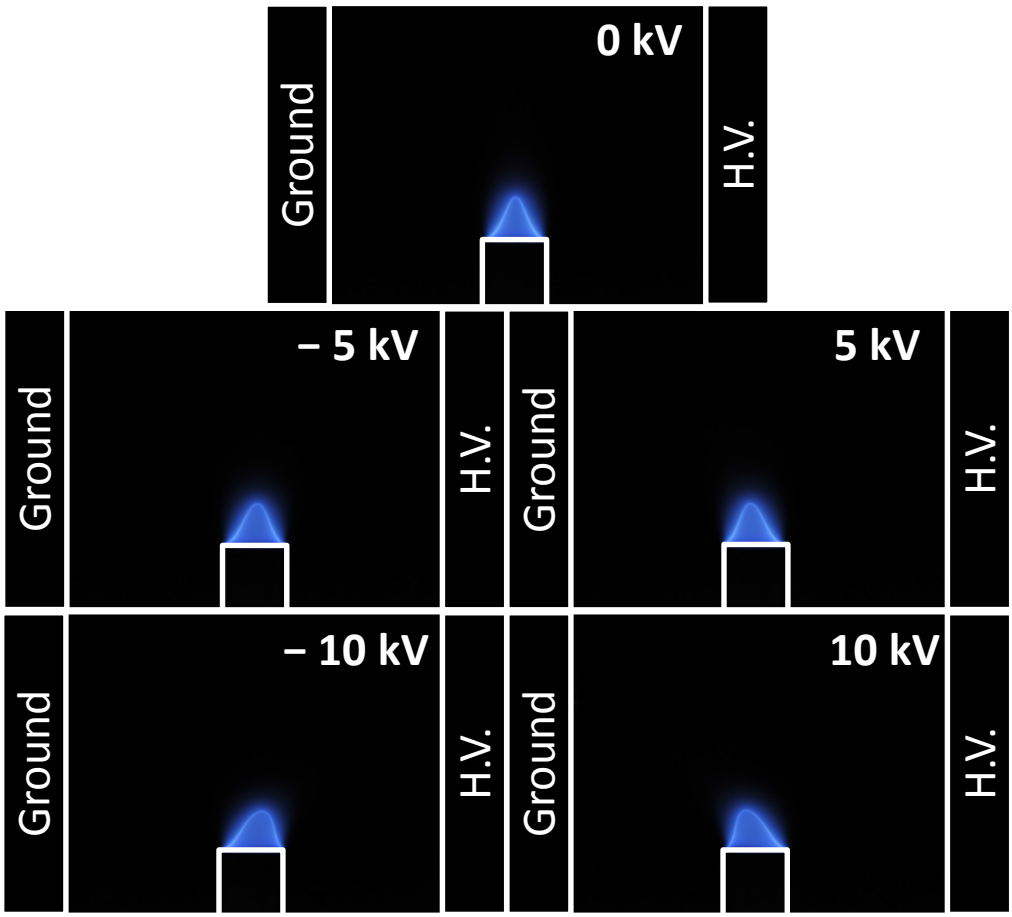

Figure 5.2 Variation of premixed Bunsen flame with equivalent ratio 1 at selected applied voltages (V_{dc} =−10, −5, 5, 10 kV), and no electric field.

Once again, the number of positive charges balanced the negative charges in a reaction zone of a hydrocarbon fuel. The positively charged substances were positive ions, while the negatively charged substances consisted of negative ions and electrons, so that the number of positive ions was greater than that of the negative ions. Because the effect of electrons having negligible mass on electrical body force is rarely expected, a net electric body force subjected to a flame zone can be conceived as it acts on positively charged reaction volume. Thus, as in Fig. 5.2, the flames that slanted toward the cathode (lower potential) with the external DC field can be explained; this is consistent with previous studies [17, 35], and with Chapters 3 and 4.

An electric current, I, in the flame represents flow of electric charges due to external electric fields. Investigating voltage-current characteristics in a flame with increased V_{dc}, two distinct regimes--sub-saturated and saturated regimes--can be found. In a sub-saturated regime, the electrical current rapidly increases, showing $I \sim V_{dc}^{2}$, up to a certain voltage; then the electric current becomes insensitive to further increased V_{dc}, resulting in a saturation of the electric current. This saturated behavior of the current is understood to be the result of a finite rate of ion generation in a flame, so that when the external potential is high enough to pull out all the generated charge carriers, the rate of ion generation simply limits the electric current which follows.

The electric current is a primary response of charge carriers generated by a flame under the influence of external electric fields, and it should be closely related to modified flame characteristics because it is a result of electric body force acting on a flame, and a movement ion is accompanied by a bulk flow motion. In this regard, flame responses due

to electric fields are compared with electric current behavior in Chapter 4, as well as in previous studies [75]. It was reported that in a counterflow burner (or downward in a small nonpremixed flame), a flame shape or a flame location was affected very little by external electric fields when an applied voltage was at the sub-saturated regime, and a drastic change of flame was observed in the saturated regime. Because a relationship between the electric current and flame behavior with an external electric field can be different for burner configurations or flame types, it is necessary to investigate the electric current to understand flame response in the present setup.

Figure 5.3 shows an electric current with applied voltage up to ±10 kV in the present methane-air premixed Bunsen flame. For both positive and negative potential to the high voltage electrode, the measured electric current increased in the tested range of V_{dc}, illustrating a quadratic increase in the current along V_{dc}, as curve-fitted in the figure. The electric current was well measured and found to be symmetric with respect to the polarity of the applied voltage, indicating good agreement with a modeling [79]. A saturated regime could not be found in the test range, indicating that the applied voltage was lower than critical to reach current saturation. Unlike previously tested flames, this flame exhibited modification in shape and location, even in the sub-saturated regime. Since a detailed mechanism of flame location does not clarify whether it is a burner configuration (counterflow or jet-flow), or a flame type (diffusion or premixed flame), this should be investigated in the future.

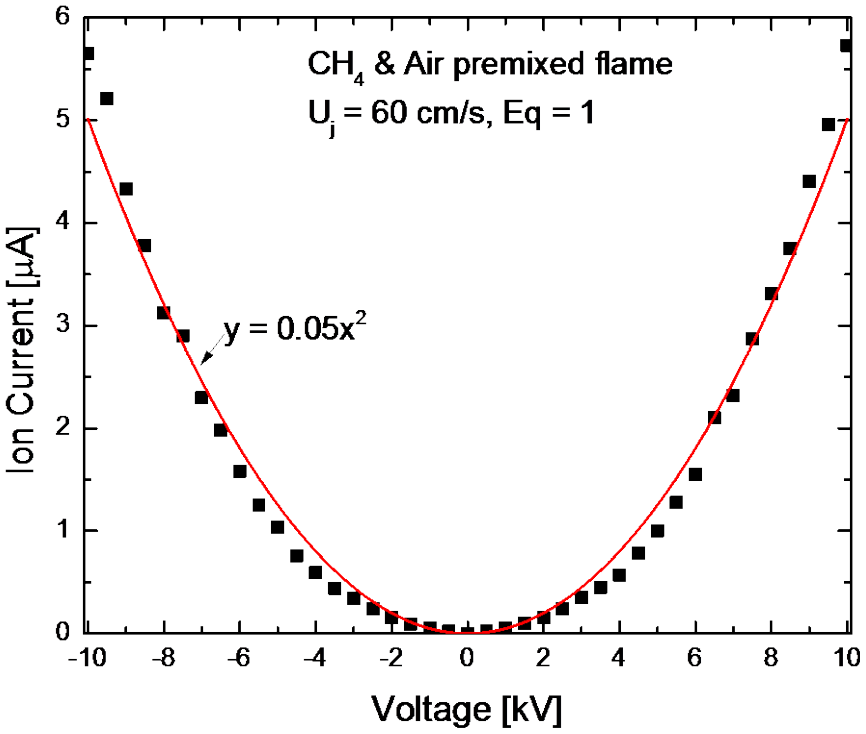

Figure 5.3. Voltage-current characteristics in methane-air premixed Bunsen flame with applied voltage to ±10 kV.

5.3.2 Ionic wind in jet flame

As shown in Fig. 5.2 and discussed in the previous section (5.3.1), it is clear that a flame under the influence of an electric field relocates toward a lower potential side. In previous studies this has sometimes been explained as a result of ionic wind due to overall outnumbered positive ions. In Chapter 4 ionic wind was identified as blowing toward both electrodes, particularly after a saturated regime of electric current in a counterflow diffusion flame. It was referred to as a bidirectional ionic wind because of the difference in the moving directions of ions in electric field due to their polarities.

Positive and negative ions, which are forced to move toward a cathode (lower potential), and anode (higher potential), respectively, transfer the momentum gained from the Lorentz force to colliding molecules, resulting in bidirectional ionic wind. In this premixed Bunsen flame, flow visualization was conducted using an Mie scattering method to determine the characteristics of a modified flow field caused by ionic wind.

Figure 5.4 illustrates Mie scattering images. The pathlines of seeding particles from the nozzle were identified as blue trajectories illuminated by the Ar-ion laser. For the flame with no electric field, a typical flow pattern with a premixed Bunsen flame was revealed. In a non-reacting cold flow, pathlines should move straight upward from the nozzle exit. However, the pathlines with the flame showed a bulge following the widest region of a reddish luminous zone. This was due to a thermal expansion of flow after the flame front; detailed flow characteristics across a premixed Bunsen flame can be found in a previous study [131]. Note that the reddish color is caused by a thermal radiation from the seeding particles when they pass through a hot reaction zone.

When DC was applied to the high voltage electrode, V_{dc} = ± 5kV f (Fig. 5.4), it is notable that the particles spread to both electrodes, while the flame slanted toward a low potential electrode. The modified movement of seeding particles can be considered a result of a bidirectional ionic wind. Because the particles moved to both electrodes, indicating flow pathlines, electrostatic charging of the seeding particles and their reaction to the electric field cannot be a major reason for the occurrence—it is impossible for seeding particles to be charged as negatively in a half domain and positively in the remainder.

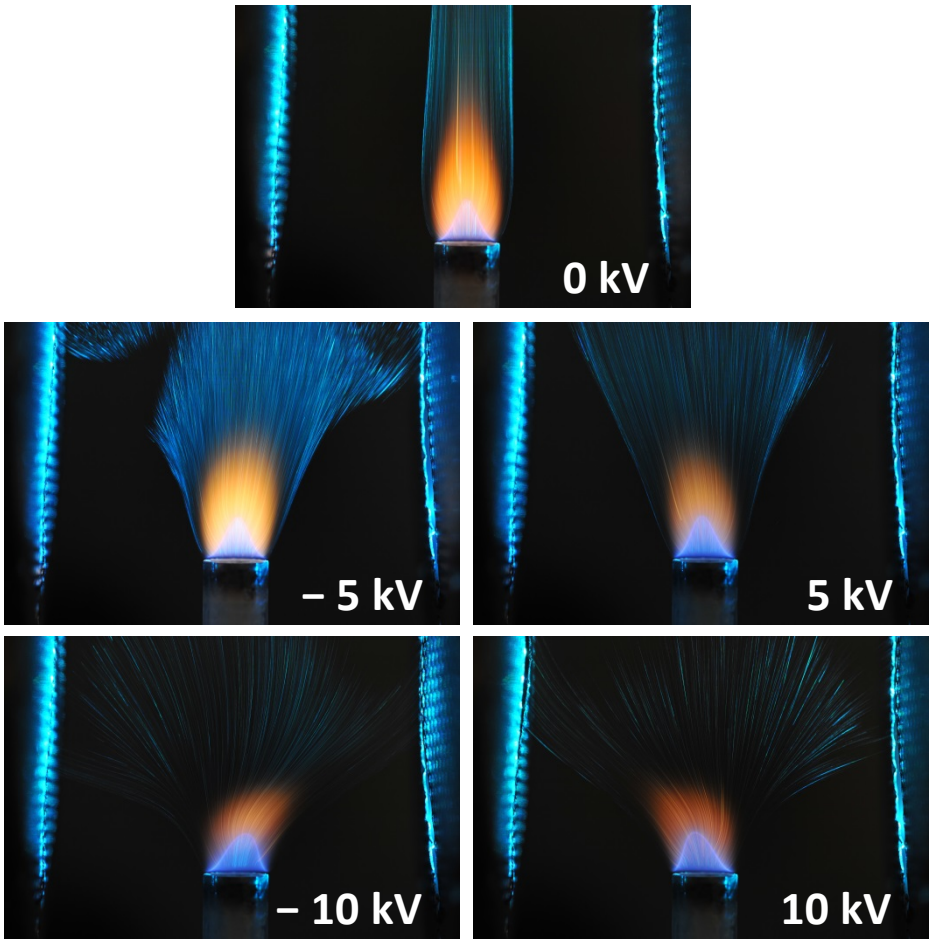

Figure 5.4. Mie scattering images of premixed Bunsen flame with equivalent ratio 1 at selected applied voltages (V_{dc} =−10, −5, 5, 10 kV) and no electric field.

For further increased applied voltage at ± 10 kV, the spread angle was expanded compared to the cases of V_{dc} = ± 5kV. Since ionic wind is related to an ion drift velocity expressed as $u_d = \mu E$, where μis an ion mobility and E is an electric field intensity, the

horizontal movements of the particles were influenced by the intensity of electric field, and thus by the applied voltage.

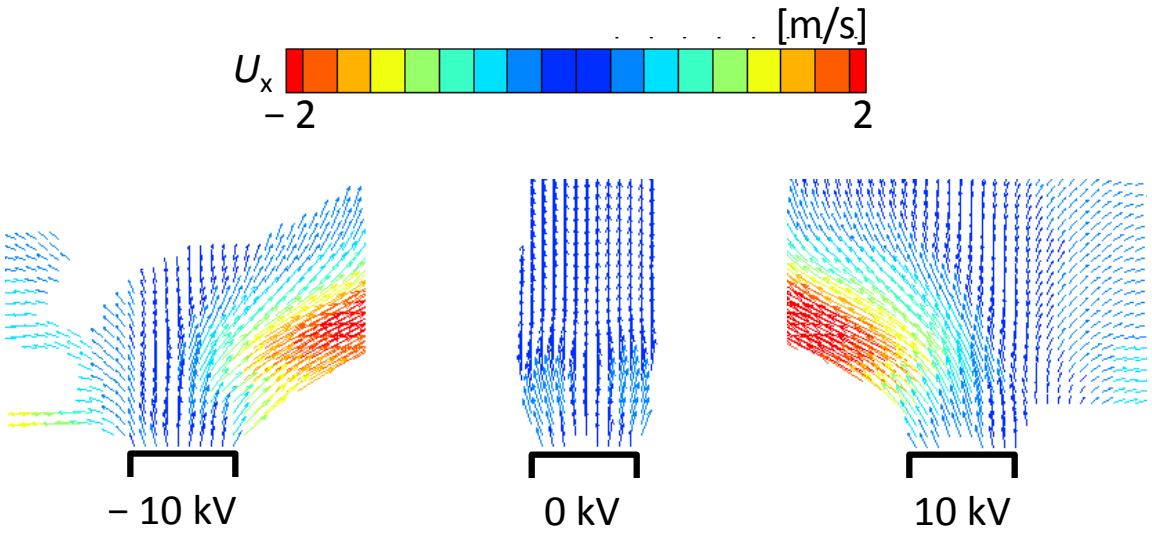

Figure 5.5. Results of a PIV of 2 dimension for premixed Bunsen flame with equivalent ratio 1 at V_{dc} =−10, 0, and 10 kV.

To quantitatively compare with the two velocities of radial components, U_x, which blow from flame to cathode and anode in bidirectional ionic wind, -- PIV measurements were conducted showing two dimensional images at V_{dc} = ± 10kV and no electric field (Fig. 5.5). With no electric field, the radial velocity was nearly zero, showing blue color in the legend; axial velocity only existed upwardly from the nozzle exit. As previously mentioned, a slight variation of radial velocity was observed in front of the flame, due to a thermal expansion of flow showing sky blue color.

When a DC field was applied to the high voltage electrode, V_{dc} = ± 10kV, the radial velocities headed toward both electrodes, consistent with the results of Mie scattering in Fig. 5.4. However, in comparison to the two velocities at opposing directions, the ionic wind from flame to cathode was much faster than flame to anode. Even though the ionic wind exists as bidirectional, the compositions of the two velocities are significantly different. Because positive ions outnumber negative ions in hydrocarbon flame, ionic wind toward the cathode can be stronger than the other. To understand the detailed mechanism, numerical simulation investigating electron attachment and ionic wind with ion chemistry should be conducted in the near future.

5.4 Summary

The effect of DC electric fields on premixed Bunsen flames with two parallel electrodes was investigated, with emphasis on flame and flow behavior. When exposed to the DC field, the tip of the flame moved toward the cathode showing a slanted conical shape. This is because positive ions are more abundant than negative ions in the reaction zone of hydrocarbon flames; therefore the flame tends to go toward the cathode due to the Lorentz force acting on positive ions.

In Chapter 4, the drastic movement of flame and the generation of bidirectional ionic wind can be observed within the saturated regime of an electric current. In the Bunsen flames, however, the flame tip responded to relatively low voltages belonging to the sub-saturated regime. To determine the response of different flames to regimes of

electric current, it will be necessary to check burner configurations, or flame type, in the future.

For flow visualization by Mie scattering, bidirectional ionic wind can be observed from a flame to two electrodes (anode and cathode). Two velocities of radial components with opposite directions were measured by PIV. It was demonstrated that the radial velocity of ionic wind from flame to cathode was much faster than from flame to anode because positive ions outnumber negative ions in the reaction zone of hydrocarbon flames.

Chapter 6

RESPONSE OF FLAMES AND FLOW TO AC ELECTRIC FIELD

6.1 Background

When a flame is exposed to a direct current (DC) electric field, positive ions, negative ions, and electrons via chemi-ionization [87-89] are subjected to the Lorentz force. As such, the positive and negative ions move toward a cathode and an anode, respectively, with a drift velocity. As a consequence of momentum transfer to neutral molecules during this migration of ions, bidirectional ionic wind blowing from the reaction zone to both electrodes was observed in Chapters 4 and 5. Similar concepts of bi-ionic wind have been introduced to explain the blowoff behavior of premixed Bunsen flames exposed to an alternating current (AC) electric field [68]. Based on the importance of ionic wind, most related studies have used the concept of ionic wind as a hypothetical explanation for the observed phenomenological results. In Chapter 3 it was speculated that a reduction in soot formation with an applied DC electric field was caused by ionic wind-driven flow field modification. An enhancement of combustion speeds in outwardly propagating premixed flames using an applied AC electric field was hypothesized to be

the result of ionic wind-driven hydrodynamic instability and/or a modification of the transport property [42].

A common assumption about applied AC electric fields is that the ionic wind can be neglected at relatively high frequencies because the flame produced above a certain AC frequency is visibly steady. However, the location of a nonpremixed flame depends on the transport of mass and heat, which are greatly affected by an internal redistribution process due to the ionic wind, and the flame zone that consistently generates ions is under the dynamic effect of the electric field, as shown in Chapter 4. Thus, it is difficult to rule out the effect of ionic wind, even when the flame is visibly steady.

Based on our previous study of DC electric fields on nonpremixed flames (Chapter 4), here the effect of applied AC electric fields on counterflow nonpremixed flames has been experimentally investigated. Specifically, the flow field, the voltage-current (V–I) behavior, and the flame location have been analyzed in terms of applied voltage and frequency. Detailed characterizations of bidirectional ionic wind and the dynamic responses of flames are discussed.

6.2 Experimental conditions

All mean jet velocities (U_j) for the fuel, oxidizer, and nitrogen sheath were identical. Two global strain rates ($\sigma = 2U_j/L$= 40 and 80 s^{-1}) of the cold streams were tested for separation distance (L) of 10 and 20 mm. To stabilize the diffusion flame, responses were guaranteed near the stagnation plane (the center of the gap in this

experiment), where the axial velocity was reasonably small and AC polarity had a negligible effect on the electric current (Chapter 4). The stoichiometric mixture fraction, Z_{st}, was fixed at 0.5. Experimental conditions are given in Table 6.1.

Metallic perforated plates (hole density = 79/cm^2, hole dia. = 0.8 mm) were placed on the exits of the nozzles to ensure reasonably uniform electric fields in the gap between the nozzles (Fig 2.3b). The tested applied voltage, V_{ac}, was up to 2.4 kV(rms), with various AC frequencies ($1 \leq f_{ac} \leq 1000$ Hz).

Table 6.1 Conditions for experiment of AC electric field

Stoichiometric mixture composition	Initial mole fractions		L [mm]	σ [s^{-1}]
(C_3H_8 / O_2 / N_2)	X_F	X_{O2}		
1 / 5 / 12	0.111	0.566	10	**40**[*]
				80
			20	40
				80
1 / 5 / 24	0.066	0.335	10	40

[*] Baseline condition

6.3 Results and discussion

6.3.1 Overall response of flames

Figure 6.1 shows typical flames in the baseline condition (exposure time 0.1s) atV_{ac} = 2.0 kV with various frequencies, f_{ac} = 10, 100, and 1000Hz, for comparison to the flame without an applied AC electric field. A discernable oscillating response to the AC electric field was found at f_{ac} = 10Hz, whereas there was no visible difference compared to the flame without the applied AC electric field at increased frequencies of 100 and 1000 Hz.

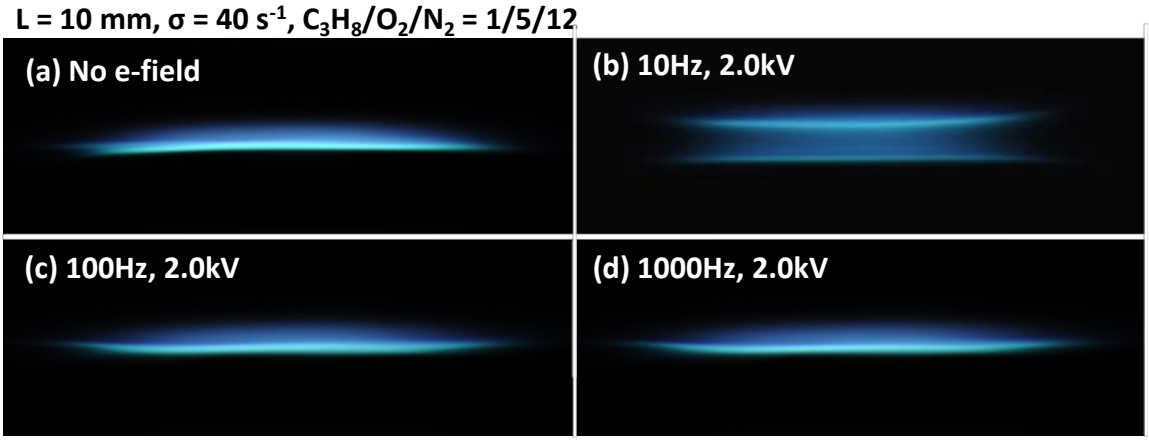

Figure 6.1 Flames in the baseline condition (a) without AC and for (b) f_{ac} = 10, (c) 100, and (d) 1000 Hz at fixed V_{ac} = 2.0 kV.

As reported in Chapters 3 and 4, nonpremixed flames tend to relocate toward the cathode with an applied DC electric field. This is believed to be caused by electric body force to the reaction zone, where ions and electrons are consistently generated. Because positive ions outnumber negative ions in the reaction zone, and electrons have negligible mass and three orders of magnitude higher mobility, the net electric body force acting on the reaction zone (flame) is directed to the cathode. Although the combined effect of this net body force on the flame and modified transport processes caused by the bidirectional ionic wind determine the new position of the flame, all observations with DC electric fields showed a relocation of the flame toward the cathode. In this regard, the periodic oscillation of the flame with the frequency of f_{ac}= 10 Hz in Fig. 5.1b can be explained from the change in the polarity of the AC electric field; the somewhat insensitive flame positions with increased f_a are discussed in Section 6.3.2.

To support this explanation, the OH radicals of an oscillating flame were visualized at f_{ac} = 10 Hz and V_{ac} = 2.4 kV (Fig. 6.2). Noting that V_{ac} = 2.4 kV (rms) indicates 3.4 kV in peak value, ±3.4 kV (DC) was applied to the lower nozzle for comparison. In Fig. 6.2, the left and right images represent corresponding half images with DC and AC electric fields, respectively. Clearly, there is little difference between the applied DC and AC electric fields in the OH images when the flame with AC reached its upper and lower peaks during a cycle of oscillation. This indicates that the oscillatory motion of the flame was caused by the polarity change.

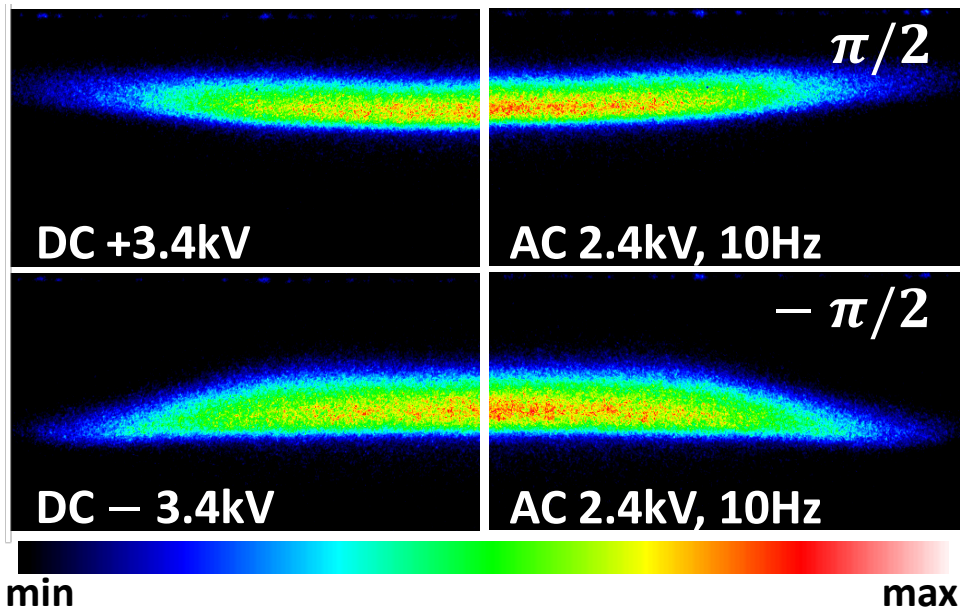

Figure 6.2 Comparison of OH radicals between DC and AC at f_{ac} = 10 Hz.

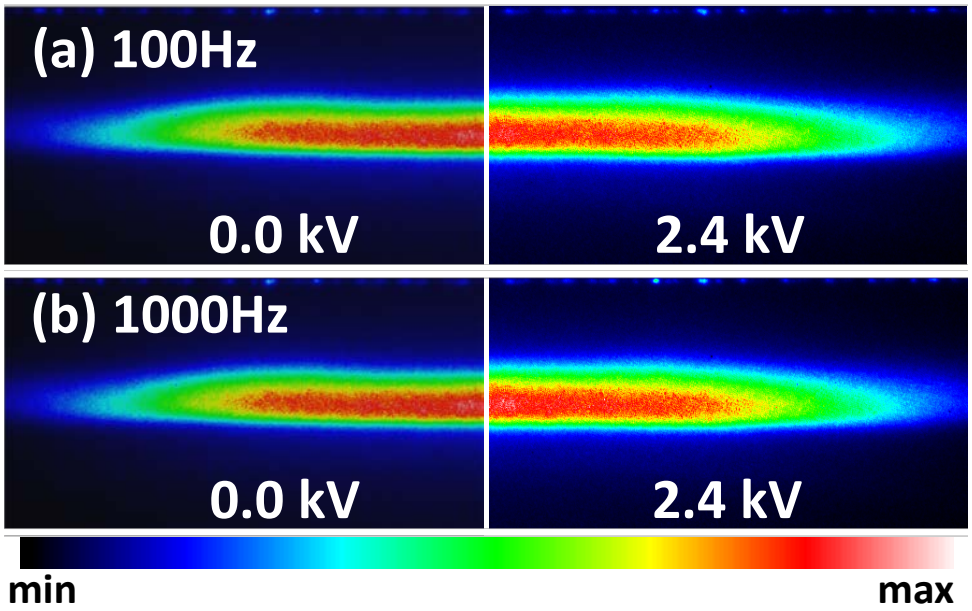

Figure 6.3 Comparison of OH radicals with AC at (a) 100 and (b) 1000 Hz.

For flames with higher f_a and negligible oscillation, OH PLIF images for V_{ac} = 2.4 kV at (a) f_{ac} = 100 and (b) 1000 Hz in Fig. 6.3 exhibit less affected OH zones in general compared to flames without AC.

To investigate the connection between observed flame behaviors and the regime of electrical responses, the electric currents of the baseline condition were measured by increasing V_{ac} at f_{ac} = 10, 100, and 1000 Hz, respectively. Figure 6.4a compares the measured electric current in rms values with that of the same flame with a negative DC electric field in Fig. 4.7 of Chapter 4. Note that to obtain current density, the measured current was divided by the flame area (luminous blue zone), projected to the electrode. Due to the fluctuating nature of f_{ac} = 10 Hz, the current density exhibited great uncertainty, which comes from a variation in the flame area during one cycle rather than from the current fluctuation. This follows a reasonably similar trend as the negative DC electric field in general, while a more rapid increase in the current occurs in the sub-saturated regime, particularly for $0.6 < V_{ac} < 1.0$ kV. Although unstable flames have been observed, resulting in indeterminate current behavior in the range of $1.1 < V_{ac} < 1.5$ kV for the DC electric field, similar unstable behavior was not found for the AC electric field in the tested range of f_{ac}. The unsteady nature of the flame caused by the AC electric field might minimize the instability related to the DC case. In conjunction with the OH images in Fig. 6.2, the data in Fig. 6.4 indicate that the overall flame characteristics and the electrical current response when f_{ac} = 10 Hz were very similar as in the case with the DC electric field.

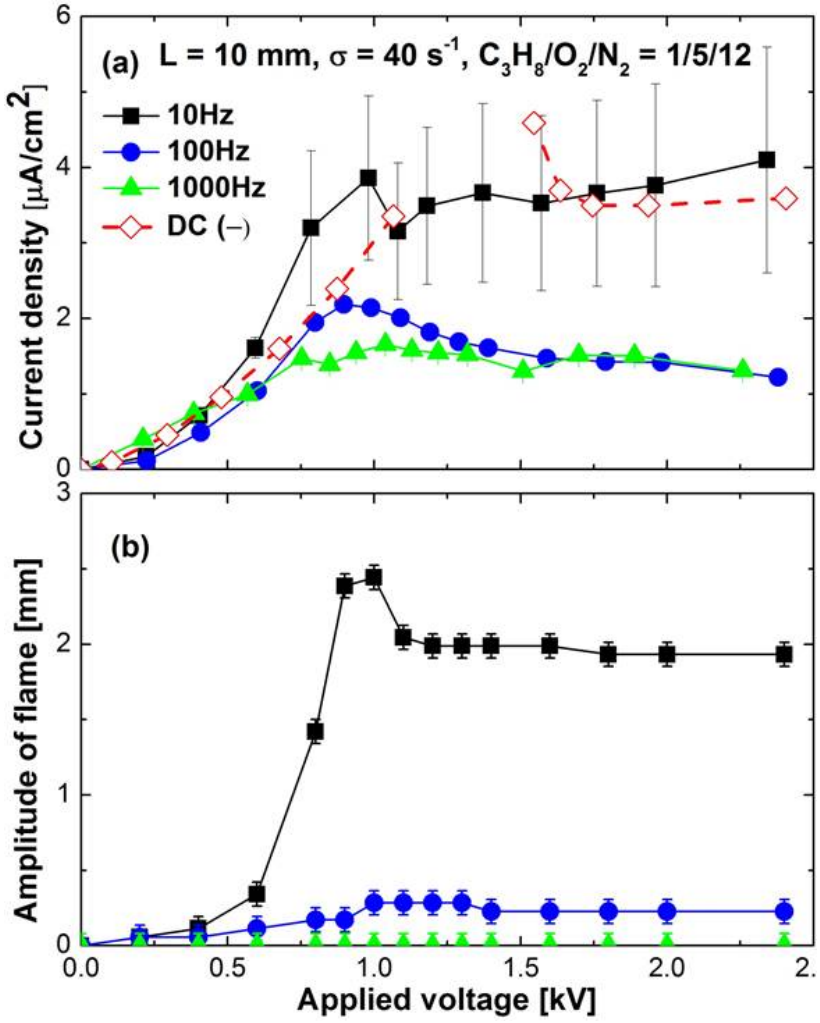

Figure 6.4 Response of (a) electric current density and (b) amplitude of flame oscillation with applied voltage at f_{ac} = 10, 100 and 1000 Hz.

As f_{ac} grows (100 and 1000 Hz), the increasing rate of current in the sub-saturated regime decreased, showing a trend similar to the case with the DC electric field. The saturated current, which should be proportional to the charge generation rate in a flame, dropped significantly, from ~3.5 to ~1.7 μA/cm^2, indicating either that the charge generation deteriorated or the number of migrating charges to the electrodes was reduced.

Given that the OH images in Fig. 6.3 show negligible dependence on f_{ac}, speculating that this drop comes from a reduction in the charge generation in the flame may not be a reasonable conclusion. Thus, the potential increase in charge recombination (neutralization) due to frequent collisions caused by the polarity change in the AC electric field might be responsible for the reduction in the migrating charges to the electrodes.

To clarify the oscillating behavior of the flames to the voltage, the amplitude of the flame oscillation (identified as the location of the luminous blue zone in Fig. 6.4b) was plotted for easy comparison to the trend of the electric current. Interestingly, when the current was saturated over a certain voltage, the amplitude of the flame oscillation also reached a certain level for f_{ac} = 10 and 100 Hz, while f_{ac} = 1000 Hz showed no significant oscillation up to 2.5 kV. At f_{ac} = 10 Hz, the amplitude of the flame oscillation was relatively insensitive to low applied voltage (< 0.5 kV); it increased sharply when applied voltage approached critical voltage for the current saturation. However, based on a hypothesis that dictates that flame oscillation should be the result of the dynamic response of charged species in the flame zone to the electric body force, the invariant oscillation amplitude--even when the voltage was increased in the saturation regime--indicated that there may have been a constraint. This will be discussed in section 6.3.2 and 6.3.3.

6.3.2 Temporal behaviors of oscillating flames

To further clarify flame behavior with an applied AC electric field, temporal variations are shown during one cycle in Fig. 6.5a at f_{ac}= 10 Hz with various V_{ac} for the baseline condition. Although the expected flame behavior would be up-and-down movement from the original position of the flame without an AC electric field driven by the polarity change, only upwardly displaced flame movements were observed in the sub-saturated regime (V_{ac} = 0.6 and 0.9 kV), where two humps (the second greater than the first) were observed. In the saturated regime (V_{ac} = 1.1, 1.5, and 2.0 kV), the flames swung around the original position, but the peaks of positive displacement were greater than those of negative displacement. When V_a increased, the positive and negative peaks did not change, indicating the presence of constraints, possibly due to mass diffusion, which can limit the flame location. As depicted in Fig. 6.5a, there is a phase delay from the applied voltage, which is around $\pi/4$ (~13 ms), indicating close conjunction with the characteristic induction time of a collision (~14 ms) estimated via molecular kinetic theory [26].

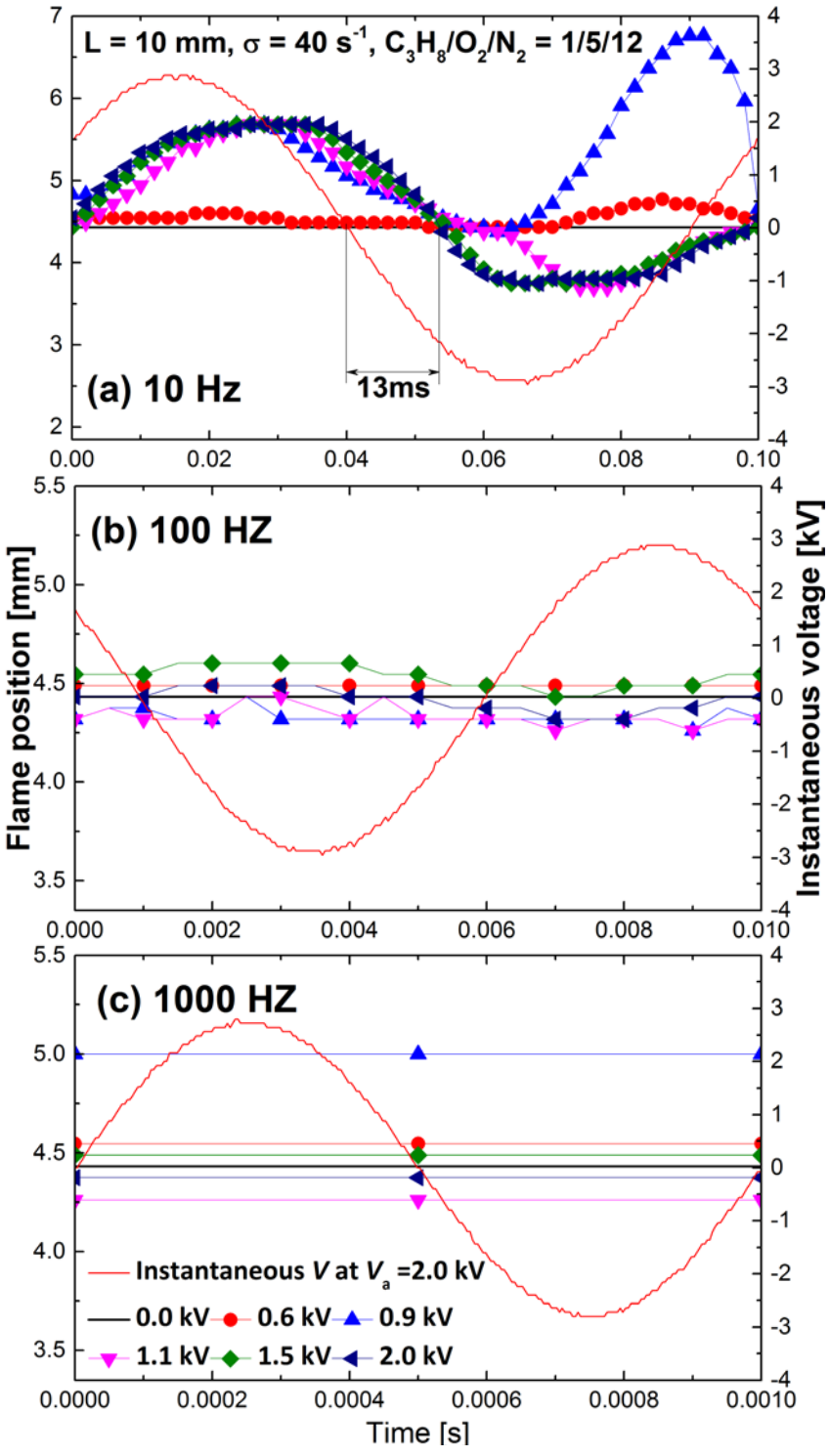

Figure 6.5 Temporal flame behavior and typical voltage waveforms for various V_{ac} at (a) f_{ac} = 10, (b) 100, and (c) 1000 Hz.

At f_{ac} = 100 Hz in Fig. 6.5b, a simple relocation of the flame position toward the upper nozzle occurs at V_{ac} = 0.6kV. With increased V_{ac}, oscillations having very small amplitudes (~0.2 mm) were observed. However, the mean flame position shifted toward the lower nozzle at V_{ac} = 1.1 and 2.0kV and toward the upper nozzle at V_{ac} = 0.6, 0.9 and 1.5kV. Finally, no discernible flame oscillation was observed at f_{ac} = 1000 Hz (Fig. 6.5c), while the relocation of the mean flame position was identified as consistent with the cases of 100Hz, except for 0.9kV. These observations indicate the difficulties experienced in conceptual modeling approaches, because a dynamic system (described as electric body force acting on ions in a reaction zone), has varying mass and ion number density over time, and its motion is constrained by a feasible flame location determined by the transport of mass and heat (for nonpremixed flames), or the velocity balance (for premixed flames). It was noted that a recent model of flame behavior with an AC electric field [85] may require modification in order to predict the present result.

6.3.3 Flame dynamics in electric body force

Motivated by the steady oscillating motion in the saturated regime, regardless of V_{ac} (i.e. constant amplitude of the flame oscillation for a given frequency (Fig. 6.4)), the oscillating amplitudes of the various flames was investigated by varying f_{ac} (Table 6.1). For L = 10 and 20 mm, the required applied voltages were 2.4 and 4.8 kV, respectively, to apply the same field intensities (E=V_{ac}/L) and ensure that the flames were in the saturated regime.

Figure 6.6 shows amplitudes normalized by each L with the applied frequency in log scales. Assuming that a dynamic response of a flame to the electric field may result in a first-order approximation of the constant mean displacement speed of a flame during a cycle (similar to the terminal velocity of charged species ($\sim\mu E$) for the ionic wind), the amplitude of the flame oscillation (the traveling distance of the flame) should be proportional to f_{ac}^{-1}. Thus, the solid line in Fig. 6.6 indicates the predicted trend of the amplitude with a constant mean flame displacement speed.

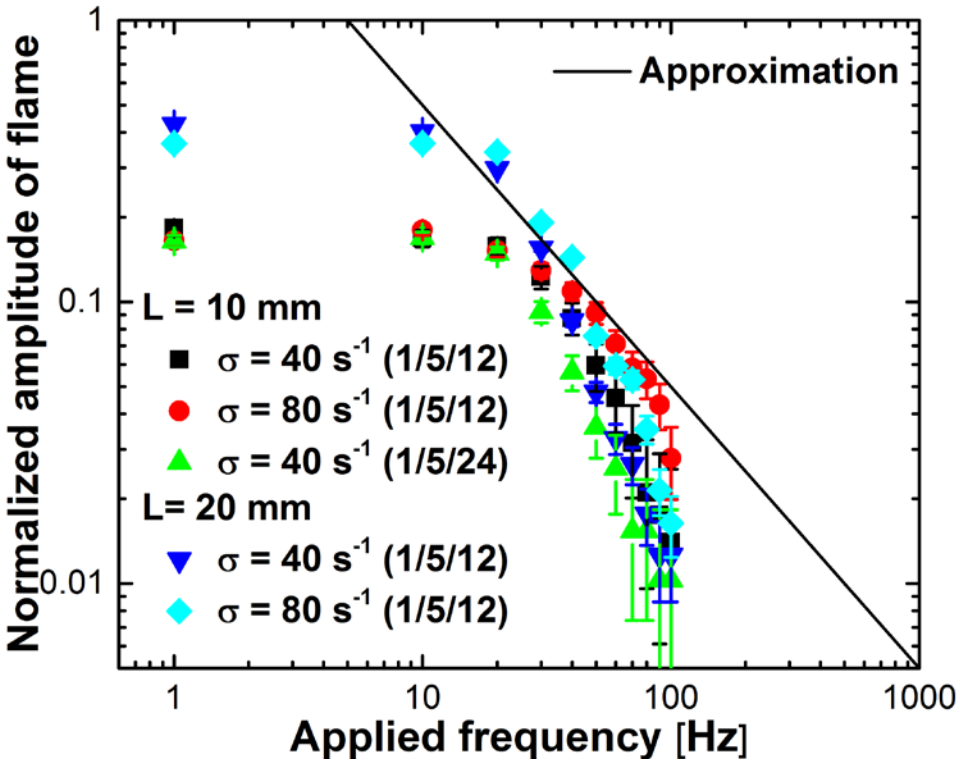

Figure 6.6 Normalized amplitude of flame oscillation in relation to applied frequency.

The dynamic response of nonpremixed flames can be divided into two distinct regimes: 1) the transport limit regime and 2) the oscillating decaying regime. As previously mentioned, the peak location of an oscillating motion with low frequency (e.g., f_{ac} = 10 Hz) is the same as the displaced location with a DC electric field (Fig. 6.2), and it seems to be limited by other factors (Fig. 6.5a), so that the amplitude is constrained up to ~20 Hz (Fig. 6.6), while there is no similarity in the gap distance. The maximum normalized amplitude with L = 10 mm is around 0.2, but it reaches ~0.4 at L = 20 mm, even with the same mixture and the same strain rate. However, because the gap distance divides the various test conditions into two pairs with similar maximum normalized amplitude, regardless of strain rate and nitrogen dilution, the absolute values of the amplitudes and deducible cyclic mean flame displacement speeds of nonpremixed flames should be closely related to the geometrical configuration and to the related transport characteristics that determine the location of a nonpremixed flame.

However, for f_{ac} increased beyond this transport limit regime, there is much faster decay than determined by the reference line, indicating that the cyclic mean flame displacement speed decreases as the frequency increases. This behavior may be attributed to the increased charge neutralization for higher f_{ac}, mentioned previously, or it may have a feature comparable to a simple dynamic oscillatory system (mass, damper, and spring), of which the response to external harmonic excitation similarly decays with increased frequency depending on the ratios of these three factors. As Fig. 6.6 implies, it should be difficult to model this system due to the strong dependence on geometrical factors. Although previous studies reported critical time scales over which ionic wind generation should be ignored [26, 68], our results indicate that the oscillatory movement of a

nonpremixed flame is more likely to decay monotonically rather than exhibiting a critical frequency. A discussion concerning ionic wind is included in the next section.

6.3.4 Flow visualization and bidirectional ionic wind

In Chapter 4, a bidirectional ionic wind was generated mostly in the saturated regime. This wind caused significant modification in the flow, leading to a double-stagnant flow configuration. Although Drews *et al.* [69] observed somewhat steady ionic wind motion, even under an AC electric field in a jet flame, Mie scattering visualization of the flow field was conducted here to clarify the effect of an AC electric field on a bidirectional ionic wind in the counterflow configuration.

Figure 6.7 shows the pathlines of seeding particles ejected from the nozzles at (a) f_{ac} = 100 and (b) 1000 Hz with selected V_{ac} for the baseline condition (0.1s exposure time). In the flame without an AC electric field, reddish luminosity caused by radiation from the seeding particles appeared at the stagnation plane, indicating that the main heat release reaction occurred at the stagnation plane based on Z_{st} = 0.5, although the luminous blue zone was located slightly into the fuel stream. The overall flow fields with both frequencies were not affected when V_{ac} = 0.7 kV, implying that the relatively low voltage in the sub-saturated regime had minimal impact on the flame or the flow, which is consistent with the DC applied field (Chapter 4).

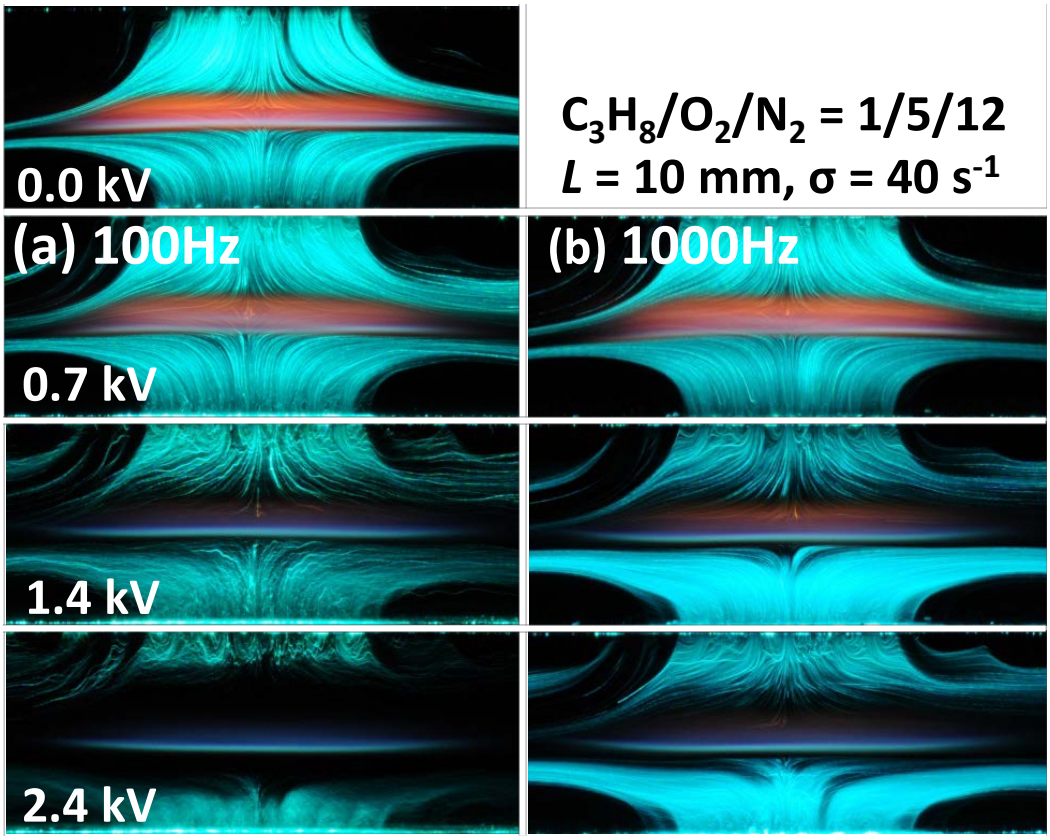

Figure 6.7 Flow visualization for selected applied voltages at (a) 100 and (b) 1000 Hz.

However, at V_{ac} = 1.4 kV in the saturated regime, drastic modification of the flow field created double-stagnation planes at both frequencies, which was the result of the bidirectional ionic wind blowing from the reaction zones to both electrodes. A dark zone created in the proximity of the flame exhibited somewhat steady behavior at these frequencies. It has been reported that maximum ion velocity is O (10^2) cm/s, depending on field intensity, E [17, 21]; and ionic wind can be expected for applied frequencies up to 100 kHz [69]. When the applied voltage was increased to V_{ac} = 2.4 kV, the dark zones became broader because the intensity of the ionic wind was proportional to the applied

voltage ($\sim \mu E$). The broadening of the dark zone at 1000 Hz was weaker than that at 100 Hz, which may be the result of increased charge neutralization caused by the higher rate of polarity change and the characteristic flow induction time with molecular collisions [68].

A temporal variation in the ionic wind is important in low-frequency ranges. High-speed images were used here, with scattered seeding particles at V_{ac}= 2.4 kV and f_{ac} = 10 Hz in the saturated regime, to determine the baseline condition. Figure 6.8 illustrates four distinct, instantaneous flow patterns for f_{ac} = 10 Hz during a cycle of ionic wind oscillation (from $-\pi$ to π). Note that--like the delayed flame oscillation phase with respect to the applied voltage (Fig. 6.5)--development of the ionic wind also exhibited phase delays. The edges of groups of scattered particles (indicating that new stagnation planes were created in response to the bidirectional ionic wind), oscillated strongly, in accordance with the electric field direction. When the dark zone was minimized the flame sat near the center of the gap, whereas when the dark zone was maximized, the flame moved toward the upper and lower nozzles. At f_{ac} = 100Hz, a pulsating oscillation of the free stream, synchronized with the f_{ac} with small variation in the dark zone, was observed. No discernable oscillation in the dark zone could be found at f_{ac}= 1000 Hz.

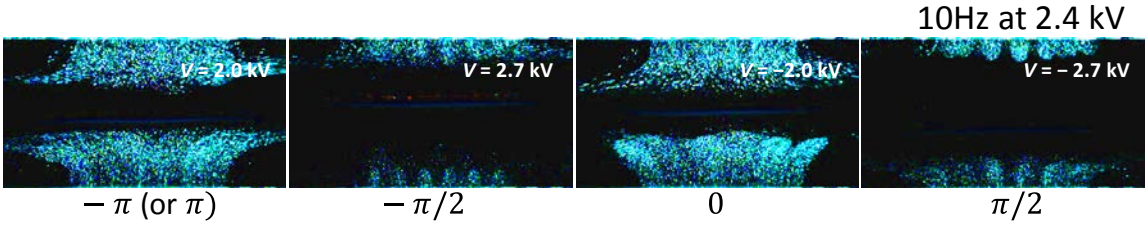

Figure 6.8 Temporal variation of Mie scattering images for oscillating flame at f_{ac} = 10 and V_{ac}= 2.4 kV.

To understand the dependence of bidirectional ionic wind on f_{ac}, normalized dark zone thicknesses were measured, which are indicative of the influence of the bidirectional ionic wind for various f_{ac} in selected flames at different L and σ at E = 2.4 kV/cm, as shown in Fig. 6.9. For low f_{ac} with an oscillating dark zone (< 200 Hz), only the maximum thickness is displayed for the sake of simplicity. Unlike the flame's oscillatory motion, thickness decreased somewhat slowly with increasing applied frequency, illustrating reasonable scaling with the gap distance. Therefore, based on either the visible flame motion or theoretical flow induction times, it is not practical to assume that the effect of ionic wind on a flame is negligible.

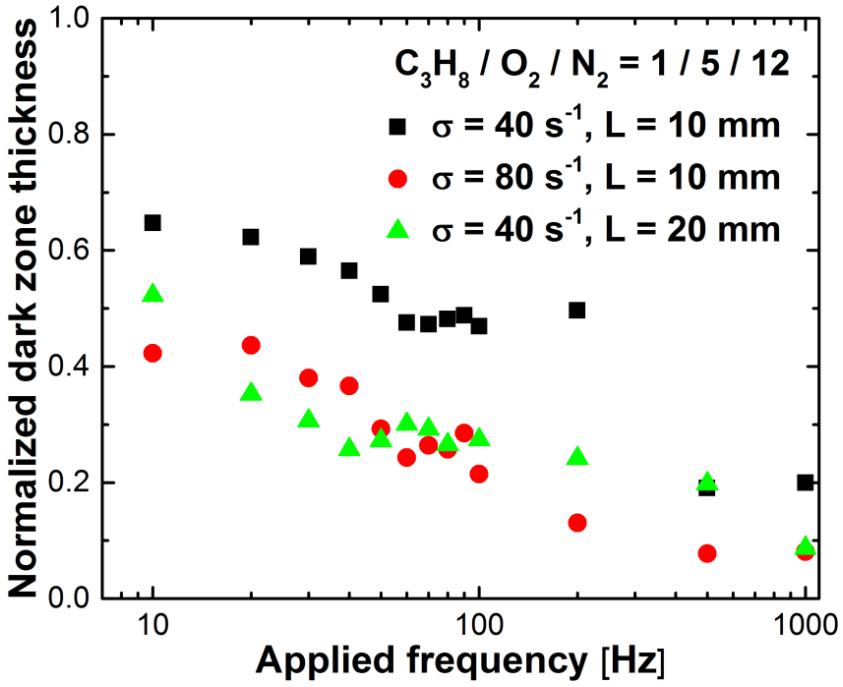

Figure 6.9 Normalized dark zone thickness in relation to applied frequency.

Normalized dark zone thicknesses at L= 20mm with σ = 40 s^{-1} showed good agreement with thicknesses at L= 10mm with σ = 80 s^{-1}, indicating a parametric similarity in jet velocity (U_{jet} = 40 cm/s). Because the stagnation plane should be determined by the momentum theorem between the ionic wind and the jet flow, and the ionic wind velocity should be similar among the flames tested due to identical field intensity, thickness should be related to velocity, rather than strain rate.

6.6 Summary

Various effects of AC electric fields on counterflow nonpremixed flames were experimentally investigated. The dynamic response of nonpremixed flames could be divided into two distinct regimes: i) the transport limit regime at lower frequencies (< ~20Hz), and ii) the oscillatory decaying regime at higher frequencies. When a bidirectional ionic wind was generated, a relatively low voltage in the sub-saturated regime did not affect the overall flow field; whereas a higher voltage in the saturated regime produced drastic modification in the flowfield-created double-stagnation planes, similar to observations with a DC electric field. Unlike the oscillatory motion of the flame, the thickness of the dark zone under bidirectional ionic wind decreased somewhat slowly, with increasing applied frequency up to 1000Hz. Based on the visibly steady flame motion, it is therefore not practical to assume that ionic wind effects are negligible at certain high AC frequencies.

It should be mentioned that although the origin of charged particle movement is caused solely by the microscopic electric body force to each charged molecule, the respective effects of such movements on a flame's dynamic motion--and on the generation of bulk flow motion--are quite different. An indirect and measurable parameter--that being the electric current--should be closely related to the motion of the flame and flow. Conceptual modeling approaches and comprehensive multi-dimensional simulations with ion-chemistry, as well as the accumulation of fundamental data in experiments, are all essential to a thorough explanation of flame dynamics.

Chapter 7

CONCLUSION

The effects of DC and AC electric fields on nonpremixed counterflow flames have been extensively studied, investigating the detailed effects of electric current with applied voltage, modifications of flame structure and flow field caused by external electric fields. To determine the results, laser diagnostics, current measurement, and direct photographs using digital and high speed camera were used with the electric fields. To investigate ionic wind motions in different configurations—typically in a sub-saturated regime and in a jet flame--a supplementary experiment using a premixed Bunsen flame was conducted applying DC. The main contributions of this thesis are summarized in the results, as follows.

1) Two distinct types of flames--SFO and SF--were experimentally studied for their structure and soot formation characteristics under electric fields. When negative electric fields were applied to the fuel nozzle, both SFO and SF flames moved toward the lower potential side (the fuel nozzle for instance); they restabilized after experiencing an unstable regime with increased applied voltage. The movement of flame under an electric field can be understood as the Lorentz force acting on outnumbered positive ions in the flames. A reduced reddish

luminosity was observed in the restabilized flames after a certain applied voltage. Based on the qualitative measurements of soot particles using PLII, no noticeable sooting limits (defined as onset conditions of soot formation in terms of initial mass fractions of oxygen and fuel in the main jets), were found when $V_{dc} = -2$ kV was applied to the fuel nozzle. Qualitative measurements of PAHs using PLIF supported the suppressed soot formation, demonstrating significant reduction in their fluorescent signal. In parallel, applied electric fields influenced OH radical distributions, which exhibited wider and thicker than flames with no electric field, indicating that there should be a significant change in flame structure caused by ionic wind with electric fields.

2) The investigation of flow field is essential to understanding the effect of electric field on ionic wind and its consequential influence on a flame structure in a nonpremixed counterflow flame. In this regard, the flow fields of nonpremixed propane flames affected by DC electric fields were visualized using the Mie scattering method. A flow field without an electric field, or with the application of a relative low voltage ($|V_a| < 1.2$ kV), (which fell in a sub-saturated regime in terms of electric current), showed a typical flow pattern for a counterflow configuration with a stagnation plane at the center. However, a drastic change in the flow field could be observed by applying a relatively high voltage ($|V_a| > 1.55$ kV) in a saturated regime of electric current. In the saturated regime, double stagnant flow fields were found, caused by bidirectional ionic wind blowing from a flame to both electrodes (nozzles); flame relocation toward a lower potential electrode could be partly attributed to this newly-settled flow pattern.

Both positive and negative ions in the reaction zone of a flame could generate a bulk flow motion in opposite directions, so that the existence of bidirectional ionic wind could be understood in a nonpremixed counterflow flame. Drastic modification in the flow field can influence variations in soot formation and OH radical distribution because of the change in the stoichiometric location and strain rate at the flame; these are important factors to characterize nonpremixed counterflow flames. Restabilization of a flame was uniformly observed for all tested fuels (methane, propane, ethane, and n-butane), and flow separation (indicated by double stagnant flow fields) occurred in each saturated regime, giving the appearance of a close relation between these two events (flame restabilization and forming double stagnant flow). However, clarification for this fuel dependency should be prepared in the near future; and to fully understand these flow fields, a numerical simulation with detailed ion-chemistry and ionic wind will be necessary.

3) In a nonpremixed counterflow flame, ionic wind did not appear to be effective when applied voltage was in a sub-saturated regime, which could be attributed partially to the directions of ionic wind exactly against the main jets. To clarify the nature of ionic wind in a different configuration—typically in a sub-saturated regime--a premixed Bunsen flame was tested by placing two parallel electrodes vertically, so that a main jet axis was perpendicular to the applied electric field lines. A shift of the flame front applying the DC was consistent with that of a nonpremixed counterflow flame, demonstrating flame movement due to the Lorentz force acting on positive ions. The tip of the flame moved toward the

lower electric potential side, resulting in a slanted conical shape. Flow visualization using Mie scattering revealed bidirectional ionic wind from the flame to both electrodes, indicating an increased radial component of velocity. In addition, PIV measurements showed that a created radial velocity caused by positive ions (i.e. toward a lower electric potential side), was much faster than the velocity toward other electrodes; this could be attributed to outnumbered positive ions in the reaction zone. Another notable observation was that the modification of flame shape and the generation of bidirectional ionic wind were found even in a sub-saturated regime, unlike the behavior in the counterflow flame. Since a detailed explanation of burner configurations or flame types is not available, these studies should be addressed in future work.

4) When an AC electric field was applied to a flame, it was generally believed that the ionic wind would be negligible in a higher frequency; this was based on an observation of a steady flame which seemed to be affected by AC. However, there is no evidence to guarantee such a hypothesis. For this reason, the dynamic response of the flame and the generation of ionic wind were investigated by applying an AC electric field to nonpremixed counterflow flames. Two distinctive regimes--a transport limit regime at lower frequencies ($f_{ac} < 20$Hz), and an oscillatory decaying regime at higher frequencies ($20\ \text{Hz} \leq f_{ac} \leq 100$Hz)--could be observed in relatively high voltage in the saturated regime. Through flow visualization, a drastic flow modification was found showing double stagnation planes due to bidirectional ionic wind, which is similar to the result with a DC. The thickness of the dark zone decreased with an increase in applied

frequency to 1000Hz. This implies that ionic wind can be generated at even a visibly steady flame; thus the effect of ionic wind cannot be negligible under AC electric fields.

Overall, it was determined that the effects of bidirectional ionic wind by DC or AC electric field can significantly affect the characteristics of nonpremixed counterflow flame, including the strain rate and the axial location of stoichiometry. As noted previously, to fully comprehend the physicochemical mechanisms on flame characteristics by the application of an electric field, a comprehensive simulation is necessary in the near future, including detailed ion chemistry and a multi-dimensional approach. In-depth studies on premixed counterflow flames and nonpremixed jet flames would also be valuable for building a solid understanding of the fundamental mechanisms and filling the gaps in the present knowledge

REFERENCES

[1] D.A. Lashof, D.R. Ahuja, Relative contributions of greenhouse gas emissions to global warming, *Nature*, 344 (1990) 529-531.

[2] G.D. Scholes, G.R. Fleming, A. Olaya-Castro, R. van Grondelle, Lessons from nature about solar light harvesting, *Nat Chem*, 3 (2011) 763-774.

[3] T.B. Johansson, Renewable energy: sources for fuels and electricity, Island Press, 1993.

[4] M.Z. Jacobson, M.A. Delucchi, Providing all global energy with wind, water, and solar power, Part I: Technologies, energy resources, quantities and areas of infrastructure, and materials, *Energy Policy*, 39 (2011) 1154-1169.

[5] M.A. Delucchi, M.Z. Jacobson, Providing all global energy with wind, water, and solar power, Part II: Reliability, system and transmission costs, and policies, *Energy Policy*, 39 (2011) 1170-1190.

[6] K. Kohse-Höinghaus, P. Oßwald, T.A. Cool, T. Kasper, N. Hansen, F. Qi, C.K. Westbrook, P.R. Westmoreland, Biofuel combustion chemistry: from ethanol to biodiesel, *Angewandte Chemie International Edition*, 49 (2010) 3572-3597.

[7] T.M. Vu, J. Park, O.B. Kwon, D.S. Bae, J.H. Yun, S.I. Keel, Effects of diluents on cellular instabilities in outwardly propagating spherical syngas–air premixed flames, Int'l Journal of Hydrogen Energy, 35 (2010) 3868-3880.

[8] R.D. Reitz, Directions in internal combustion engine research, *Combustion and Flame*, 160 (2013) 1-8.

[9] Y. Ju, W. Sun, Plasma assisted combustion: Progress, challenges, and opportunities, *Combustion and Flame*, 162 (2015) 529-532.

[10] A.Y. Starikovskii, Plasma supported combustion, *Proceedings of the Combustion Institute*, 30 (2005) 2405-2417.

[11] A. Starikovskiy, N. Aleksandrov, Plasma-assisted ignition and combustion, *Progress in Energy and Combustion Science*, 39 (2013) 61-110.

[12] J. Lawton, F.J. Weinberg, Electrical aspects of combustion, *Clarendon Press Oxford*, 1969.

[13] D. Boothman, J. Lawton, S.J. Melinek, F. Weinberg, Rates of ion generation in flames, *Symposium (International) on Combustion*, 12 (1969) 969-978.

[14] R.J. Bowser, F.J. Weinberg, The effect of direct electric fields on normal burning velocity, *Combustion and Flame*, 18 (1972) 296-300.

[15] R.J. Bowser, F.J. Weinberg, Chemi-ionisation during pyrolysis, *Combustion and Flame*, 27 (1976) 21-32.

[16] S.K. Dayal, T.P. Pandya, Optical study of counterflow diffusion flames in transverse electric fields, *Combustion and Flame*, 19 (1972) 113-116.

[17] J. Lawton, P.J. Mayo, F.J. Weinberg, Electrical Control of Gas Flows in Combustion Processes, *Proceeding of The Royal Society*, A303 (1968) 275-298.

[18] J. Lawton, F. Weinberg, Maximum ion currents from flames and the maximum practical effects of applied electric fields, *Proceedings of the Royal Society of London. Series A. Mathematical and Physical Sciences*, 277 (1964) 468-497.

[19] P. Mayo, F. Weinberg, On the size, charge and number-rate of formation of carbon particles in flames subjected to electric fields, *Proceedings of the Royal Society of London. A. Mathematical and Physical Sciences*, 319 (1970) 351-371.

[20] T. Pandya, F. Weinberg, The structure of flat, counter-flow diffusion flames, *Proceedings of the Royal Society of London. Series A. Mathematical and Physical Sciences*, 279 (1964) 544-561.

[21] K.G. Payne, F.J. Weinberg, Mesurements on field-induced ion flows from plane flames, *Symposium (International) on Combustion*, 8 (1961) 207-217.

[22] F.J. Weinberg, Advanced combustion methods, *Academic Press*, London, 1986.

[23] F.J. Weinberg, D. Dunn-Rankin, F.B. Carleton, S. Karnani, C. Markides, M. Zhai, Electrical aspects of flame quenching, *Proceedings of the Combustion Institute*, 34 (2013) 3295-3301.

[24] J. Cancian, B.A.V. Bennett, M.B. Colket, M.D. Smooke, Prediction of electron and ion concentrations in low-pressure premixed acetylene and ethylene flames, *Combustion Theory and Modelling*, 17 (2013) 294-315.

[25] M.S. Cha, S.M. Lee, K.T. Kim, S.H. Chung, Soot suppression by nonthermal plasma in coflow jet diffusion flames using a dielectric barrier discharge, *Combustion and Flame*, 141 (2005) 438-447.

[26] M. Kono, F.B. Carleton, A.R. Jones, F.J. Weinberg, The effect of nonsteady electric fields on sooting flames, *Combustion and Flame*, 78 (1989) 357-364.

[27] M. Kono, K. Iinuma, S. Kumagai, The effect of dc to 10 MHz electric field on flame luminosity and carbon formation, *Symposium (International) on Combustion*, 18 (1981) 1167-1174.

[28] M.M. Maricq, Size and charge of soot particles in rich premixed ethylene flames, *Combustion and Flame*, 137 (2004) 340-350.

[29] H. Ohisa, I. Kimura, H. Horisawa, Control of soot emission of a turbulent diffusion flame by DC or AC corona discharges, *Combustion and Flame*, 116 (1999) 653-661.

[30] M. Saito, T. Arai, M. Arai, Control of soot emitted from acetylene diffusion flames by applying an electric field, *Combustion and Flame*, 119 (1999) 356-366.

[31] A. Vatazhin, D. Golentsov, V. Likhter, Soot Extraction from a Laminar Hydrocarbon Flame by Means of an Electric Field, *Fluid Dynamics*, 40 (2005) 172-178.

[32] Y. Wang, G.J. Nathan, Z.T. Alwahabi, K.D. King, K. Ho, Q. Yao, Effect of a uniform electric field on soot in laminar premixed ethylene/air flames, *Combustion and Flame*, 157 (2010) 1308-1315.

[33] L. Xie, T. Kishi, M. Kono, Investigation on the effect of electric fields on soot formation and flame structure of diffusion flames, *Symposium (International) on Combustion*, 24 (1992) 1059-1066.

[34] Y. Xiong, M.S. Cha, S.H. Chung, AC electric field induced vortex in laminar coflow diffusion flames, *Proceedings of the Combustion Institute*, 35 (2015) 3513-3520.

[35] E. Place, F. Weinberg, Electrical control of flame carbon, *Proceedings of the Royal Society of London. Series A. Mathematical and Physical Sciences*, 289 (1966) 192-205.

[36] E.R. Place, F.J. Weinberg, The nucleation of flame carbon by ions and the effect of electric fields, *Symposium (International) on Combustion*, 11 (1967) 245-255.

[37] D.R. Hardesty, F.J. Weinberg, Electrical control of particulate pollutants from flames, *Symposium (International) on Combustion*, 14 (1973) 907-918.

[38] M. Saito, M. Sato, K. Sawada, Variation of flame shape and soot emission by applying electric field, *Journal of Electrostatics*, 39 (1997) 305-311.

[39] M. Zake, I. Barmina, D. Turlajs, Electric field control of polluting emissions from a propane flame, *Global Nest: The Int'l. Jorunal*, 3 (2001) 95-108.

[40] E.V. Vega, S.S. Shin, K.Y. Lee, NO emission of oxygen-enriched CH4/O2/N2 premixed flames under electric field, *Fuel*, 86 (2007) 512-519.

[41] J. Botha, D. Spalding, The laminar flame speed of propane/air mixtures with heat extraction from the flame, *Proceedings of the Royal Society of London. Series A. Mathematical and Physical Sciences*, 225 (1954) 71-96.

[42] M.S. Cha, Y. Lee, Premixed Combustion Under Electric Field in a Constant Volume Chamber, *IEEE Transactions on Plasma Science*, 40 (2012) 3131-3138.

[43] S. Marcum, B. Ganguly, Electric-field-induced flame speed modification, *Combustion and Flame*, 143 (2005) 27-36.

[44] X.W. Meng, X.M. Wu, C. Kang, A.D. Tang, Z.Q. Gao, Effects of Direct-Current (DC) Electric Fields on Flame Propagation and Combustion Characteristics of Premixed $CH_4/O_2/N_2$ Flames, *Energy & Fuels*, 26 (2012) 6612-6620.

[45] A. Tang, X. Meng, Z. Zhou, R. Zhou, X. Wu, Effect of non-uniform electric field on spherical flame characteristics, Ranshao Kexue Yu Jishu, *Journal of Combustion Science and Technology*, 19 (2013) 275-280.

[46] S.H. Won, M.S. Cha, C.S. Park, S.H. Chung, Effect of electric fields on reattachment and propagation speed of tribrachial flames in laminar coflow jets, *Proceedings of the Combustion Institute*, 31 (2007) 963-970.

[47] S.H. Won, S.K. Ryu, M.K. Kim, M.S. Cha, S.H. Chung, Effect of electric fields on the propagation speed of tribrachial flames in coflow jets, *Combustion and Flame*, 152 (2008) 496-506.

[48] E.M. Guénault, R.V. Wheeler, XXVII.—The propagation of flame in electric fields. Part I. Distortion of the flame surface, *Journal of the Chemical Society* (Resumed), (1931) 195-199.

[49] E. Guenault, R. Wheeler, 423. The propagation of flame in electric fields. Part II. The effects of transverse fields, *Journal of the Chemical Society* (Resumed), (1932) 2788-2793.

[50] H.C. Jaggers, A. von Engel, The effect of electric fields on the burning velocity of various flames, *Combustion and Flame*, 16 (1971) 275-285.

[51] M.K. Kim, S.H. Chung, O. Fujita, Effect of AC electric fields on flame spread over electrical wire, *Proceedings of the Combustion Institute*, 33 (2011) 1145-1151.

[52] S.J. Lim, M. Kim, J. Park, O. Fujita, S. Chung, Flame spread over electrical wire with AC electric fields: Internal circulation, fuel vapor-jet, spread rate acceleration, and molten insulator dripping, *Combustion and Flame*, 162 (2015) 1167-1175.

[53] J.D.B.J. van den Boom, A.A. Konnov, A.M.H.H. Verhasselt, V.N. Kornilov, L.P.H. de Goey, H. Nijmeijer, The effect of a DC electric field on the laminar burning velocity of premixed methane/air flames, *Proceedings of the Combustion Institute*, 32 (2009) 1237-1244.

[54] A. Starikowskii, M. Skoblin, T. Hammer, Influence of weak electric fields on the flame structure, *Gas Discharges and Their Applications*, 17th International Conference, (2008), pp. 629-632.

[55] T.M. Vu, S.H. Won, T. Ombrello, M.S. Cha, Stability enhancement of ozone-assisted laminar premixed Bunsen flames in nitrogen co-flow, *Combustion and Flame*, 161 (2014) 917-926.

[56] M. Belhi, P. Domingo, P. Vervisch, Direct numerical simulation of the effect of an electric field on flame stability, *Combustion and Flame*, 157 (2010) 2286-2297.

[57] Y. Gan, Y. Luo, M. Wang, Y. Shi, Y. Yan, Effect of alternating electric fields on the behaviour of small-scale laminar diffusion flames, *Applied Thermal Engineering*, 89 (2015) 306-315.

[58] A. Sakhrieh, G. Lins, F. Dinkelacker, T. Hammer, A. Leipertz, D.W. Branston, The influence of pressure on the control of premixed turbulent flames using an electric field, *Combustion and Flame*, 143 (2005) 313-322.

[59] L. Sang Min, P. Cheol Soo, C. Min Suk, C. Suk Ho, Effect of electric fields on the liftoff of nonpremixed turbulent jet flames, Plasma Science, *IEEE Transactions on*, 33 (2005) 1703-1709.

[60] H.F. Calcote, R.N. Pease, Electrical Properties of Flames. BurnerFlames in Longitudinal Electric Fields, Industrial & Engineering Chemistry, 43 (1951) 2726-2731.

[61] R. Noorani, R. Holmes, Effects of electric fields on the blowoff limits of a methane-air flame, *AIAA Journal*, 23 (1985) 1452-1454.

[62] M.K. Kim, S.K. Ryu, S.H. Won, S.H. Chung, Electric fields effect on liftoff and blowoff of nonpremixed laminar jet flames in a coflow, *Combustion and Flame*, 157 (2010) 17-24.

[63] S.K. Ryu, Y.K. Kim, M.K. Kim, S.H. Won, S.H. Chung, Observation of multi-scale oscillation of laminar lifted flames with low-frequency AC electric fields, *Combustion and Flame*, 157 (2010) 25-32.

[64] A. Ata, J.S. Cowart, A. Vranos, B.M. Cetegen, Effects of direct current electric field on the blowoff characteristics of bluff-body stabilized conical premixed flames, *Combustion Science and Technology*, 177 (2005) 1291-1304.

[65] M.K. Kim, S.H. Chung, H.H. Kim, Effect of AC electric fields on the stabilization of premixed bunsen flames, *Proceedings of the Combustion Institute*, 33 (2011) 1137-1144.

[66] F. Carleton, F. Weinberg, Electric field-induced flame convection in the absence of gravity, *Nature*, 330 (1987) 635-636.

[67] M. Rickard, D. Dunn-Rankin, F. Weinberg, F. Carleton, Characterization of ionic wind velocity, *Journal of Electrostatics*, 63 (2005) 711-716.

[68] M.K. Kim, S.H. Chung, H.H. Kim, Effect of electric fields on the stabilization of premixed laminar bunsen flames at low AC frequency: Bi-ionic wind effect, *Combustion and Flame*, 159 (2012) 1151-1159.

[69] A.M. Drews, L. Cademartiri, M.L. Chemama, M.P. Brenner, G.M. Whitesides, K.J.M. Bishop, ac electric fields drive steady flows in flames, *Physical Review E*, 86 (2012) 036314.

[70] M.J. Papac, D. Dunn-Rankin, Canceling buoyancy of gaseous fuel flames in a gravitational environment using an ion-driven wind, *Annals of the New York Academy of Sciences*, 1077 (2006) 585-601.

[71] K. Payne, F. Weinberg, A preliminary investigation of field-induced ion movement in flame gases and its applications, *Proceedings of the Royal Society of London. Series A. Mathematical and Physical Sciences*, 250 (1959) 316-336.

[72] J. Lawton, P.J. Mayo, Factors influencing maximum ionic wind velocities, *Combustion and Flame*, 16 (1971) 253-263.

[73] K.G. Xu, Plasma sheath behavior and ionic wind effect in electric field modified flames, *Combustion and Flame*, 161 (2014) 1678-1686.

[74] J. Hu, B. Rivin, E. Sher, The effect of an electric field on the shape of co-flowing and candle-type methane–air flames, *Experimental Therm Fluid Sci.*, 21 (2000) 124-133.

[75] F. Borgatelli, D. Dunn-Rankin, Behavior of a small diffusion flame as an electrically active component in a high-voltage circuit, *Combustion and Flame*, 159 (2012) 210-220.

[76] S. Karnani, D. Dunn-Rankin, Detailed characterization of DC electric field effects on small non-premixed flames, *Combustion and Flame*, 162 (2015) 2865-2872.

[77] M.J. Papac, Electrical aspects of gaseous fuel flames for microgravity combustion and combustion control, *Ph.D Thesis*, 2005.

[78] J. Vinogradov, E. Sher, I. Rutkevich, M. Mond, Voltage-current characteristics of a flame-assisted unipolar corona, *Combustion and Flame*, 127 (2001) 2041-2050.

[79] Y. Xiong, D.G. Park, B.J. Lee, S.H. Chung, M.S. Cha, DC field response of one-dimensional flames using an ionized layer model, *Combustion and Flame*, 163 (2016) 317-325.

[80] N. Speelman, M. Kiefer, D. Markus, U. Maas, L. de Goey, J. van Oijen, Validation of a novel numerical model for the electric currents in burner-stabilized methane–air flames, *Proceedings of the Combustion Institute*, 35 (2015) 847-854.

[81] L.B.W. Peerlings, Manohar, V.N. Kornilov, P. de Goey, Flame ion generation rate as a measure of the flame thermo-acoustic response, *Combustion and Flame*, 160 (2013) 2490-2496.

[82] M.J. Papac, D. Dunn-Rankin, Modelling electric field driven convection in small combustion plasmas and surrounding gases, *Combustion Theory and Modelling*, 12 (2008) 23-44.

[83] K. Yamashita, S. Karnani, D. Dunn-Rankin, Numerical prediction of ion current from a small methane jet flame, *Combustion and Flame*, 156 (2009) 1227-1233.

[84] F. Bisetti, M. El Morsli, Calculation and analysis of the mobility and diffusion coefficient of thermal electrons in methane/air premixed flames, *Combustion and Flame*, 159 (2012) 3518-3521.

[85] C. Guerra-Garcia, M. Martinez-Sanchez, Counterflow nonpremixed flame DC displacement under AC electric field, *Combustion and Flame*, 162 (2015) 4254-4263.

[86] A. Patyal, D. Kyritsis, M. Matalon, Electric field effects in the presence of chemi-ionization on droplet burning, *Combustion and Flame*, 164 (2016) 99-110.

[87] J.M. Goodings, D.K. Bohme, C.-W. Ng, Detailed ion chemistry in methane ☐oxygen flames. I. Positive ions, *Combustion and Flame*, 36 (1979) 27-43.

[88] J.M. Goodings, D.K. Bohme, C.-W. Ng, Detailed ion chemistry in methane ☐oxygen flames. II. Negative ions, Combustion and Flame, 36 (1979) 45-62.

[89] A.B. Fialkov, Investigations on ions in flames, *Progress in Energy and Combustion Science*, 23 (1997) 399-528.

[90] H.F. Calcote, Ion production and recombination in flames, S*ymposium (International) on Combustion*, 8 (1961) 184-199.

[91] J. Prager, U. Riedel, J. Warnatz, Modeling ion chemistry and charged species diffusion in lean methane–oxygen flames, *Proceedings of the Combustion Institute*, 31 (2007) 1129-1137.

[92] F. Weinberg, F. Carleton, D. Dunn-Rankin, Electric field-controlled mesoscale burners, *Combustion and Flame*, 152 (2008) 186-193.

[93] R.J. Heinsohn, D.E. Wulfhorst, P.M. Becker, The effects of an electric field on an opposed-jet diffusion flame, *Combustion and Flame*, 11 (1967) 288-296.

[94] R.J. Heinsohn, S.V. Thillard, P.M. Becker, Temperature profiles of an opposed-jet diffusion flame subjected to an electric field, *Combustion and Flame*, 13 (1969) 442-445.

[95] F.L. Jones, P.M. Becker, R.J. Heinsohn, A mathematical model of the opposed-jet diffusion flame: Effect of an electric field on concentration and temperature profiles, *Combustion and Flame*, 19 (1972) 351-362.

[96] E. Sher, G. Pinhasi, A. Pokryvailo, R. Bar-On, Extinction of pool flames by means of a DC electric field, *Combustion and Flame*, 94 (1993) 244-252.

[97] L. Sun, G. Lins, T. Hammer, Interaction of a low-pressure flat flame with an electric field, in: *Proceedings of the European Combustion Meeting*, Louvain-La-Neuve, 2005.

[98] F. Altendorfner, J. Kuhl, L. Zigan, A. Leipertz, Study of the influence of electric fields on flames using planar LIF and PIV techniques, *Proceedings of the Combustion Institute*, 33 (2011) 3195-3201.

[99] J. Kuhl, G. Jovicic, L. Zigan, A. Leipertz, Transient electric field response of laminar premixed flames, *Proceedings of the Combustion Institute*, 34 (2013) 3303-3310.

[100] J. Schmidt, B. Ganguly, Effect of pulsed, sub-breakdown applied electric field on propane/air flame through simultaneous OH/acetone PLIF, *Combustion and Flame*, 160 (2013) 2820-2826.

[101] M. Matalon, Intrinsic Flame Instabilities in Premixed and Nonpremixed Combustion, *Annual Review of Fluid Mechanics*, 39 (2007) 163-191.

[102] H. Tsuji, Counterflow diffusion flames, *Progress in Energy and Combustion Science*, 8 (1982) 93-119.

[103] A. Liñán, The asymptotic structure of counterflow diffusion flames for large activation energies, *Acta Astronautica*, 1 (1974) 1007-1039.

[104] K.T. Kang, J.Y. Hwang, S.H. Chung, W. Lee, Soot zone structure and sooting limit in diffusion flames: Comparison of counterflow and co-flow flames, *Combustion and Flame*, 109 (1997) 266-281.

[105] U. Niemann, K. Seshadri, F.A. Williams, Accuracies of laminar counterflow flame experiments, *Combustion and Flame*, 162 (2015) 1540-1549.

[106] D.G. Park, J.H. Yun, J. Park, S.I. Keel, A study on flame extinction characteristics along a C-curve, *Energy & Fuels*, 23 (2009) 4236-4244.

[107] Y.H. Chung, D.G. Park, J. Park, O.B. Kwon, J.H. Yun, S.I. Keel, Role of the outer-edge flame on flame extinction in nitrogen-diluted non-premixed counterflow flames with finite burner diameters, *Fuel*, 105 (2013) 540-550.

[108] X. Li, L. Jia, T. Onishi, P. Grajetzki, H. Nakamura, T. Tezuka, S. Hasegawa, K. Maruta, Study on stretch extinction limits of CH4/CO2 versus high temperature O2/CO2 counterflow non-premixed flames, *Combustion and Flame*, 161 (2014) 1526-1536.

[109] P.H. Joo, Y. Wang, A. Raj, S.H. Chung, Sooting limit in counterflow diffusion flames of ethylene/propane fuels and implication to threshold soot index, *Proceedings of the Combustion Institute*, 34 (2013) 1803-1809.

[110] Y. Wang, A. Raj, S.H. Chung, A PAH growth mechanism and synergistic effect on PAH formation in counterflow diffusion flames, *Combustion and Flame*, 160 (2013) 1667-1676.

[111] Y. Wang, S.H. Chung, Effect of strain rate on sooting limits in counterflow diffusion flames of gaseous hydrocarbon fuels: Sooting temperature index and sooting sensitivity index, *Combustion and Flame*, 161 (2014) 1224-1234.

[112] C.M. Vagelopoulos, F.N. Egolfopoulos, C.K. Law, Further considerations on the determination of laminar flame speeds with the counterflow twin-flame technique, *Symposium (International) on Combustion*, 25 (1994) 1341-1347.

[113] C.M. Vagelopoulos, F.N. Egolfopoulos, Direct experimental determination of laminar flame speeds, Symposium (International) on Combustion, 27 (1998) 513-519.

[114] M.-V. Tran, M.S. Cha, Correction of edge-flame propagation speed in a counterflow, annular slot burner, *Combustion and Flame*, 162 (2016) 4671-4672.

[115] K.C. Smyth, C.R. Shaddix, D.A. Everest, Aspects of soot dynamics as revealed by measurements of broadband fluorescence and flame luminosity in flickering diffusion flames, C*ombustion and Flame*, 111 (1997) 185-207.

[116] S.M. Lee, S.S. Yoon, S.H. Chung, Synergistic effect on soot formation in counterflow diffusion flames of ethylene–propane mixtures with benzene addition, *Combustion and Flame*, 136 (2004) 493-500.

[117] B. Quay, T.W. Lee, T. Ni, R.J. Santoro, Spatially resolved measurements of soot volume fraction using laser-induced incandescence, *Combustion and Flame*, 97 (1994) 384-392.

[118] K. Lee, Y. Han, W. Lee, J. Chung, C. Lee, Quantitative measurements of soot particles in a laminar diffusion flame using a LII/LIS technique, *Measurement Science and Technology*, 16 (2005) 519.

[119] B. Castellani, E. Morini, M. Filipponi, A. Nicolini, M. Palombo, F. Cotana, F. Rossi, Comparative analysis of monitoring devices for particulate content in exhaust gases, *Sustainability*, 6 (2014) 4287-4307.

[120] A. Melling, Tracer particles and seeding for particle image velocimetry, *Measurement Science and Technology*, 8 (1997) 1406.

[121] R.D. Keane, R.J. Adrian, Theory of cross-correlation analysis of PIV images, *Applied Scientific Research*, 49 (1992) 191-215.

[122] B. Shukla, M. Koshi, A novel route for PAH growth in HACA based mechanisms, *Combustion and Flame*, 159 (2012) 3589-3596.

[123] B. Shukla, M. Koshi, Comparative study on the growth mechanisms of PAHs, *Combustion and Flame*, 158 (2011) 369-375.

[124] E. Paganini, G. Mariotti, S. Gasperetti, C. Vallebona, L. Predolin, E. Muré, V. Palleschi, A. Salvetti, E. Tognoni, Multi-diagnostic approach to characterize the onset of formation of nanoparticles in a premixed laminar ethylene/air flame, *Spectrochimica Acta Part B: Atomic Spectroscopy*, 63 (2008) 191-201.

[125] J.Y. Hwang, S.H. Chung, Growth of soot particles in counterflow diffusion flames of ethylene, *Combustion and Flame*, 125 (2001) 752-762.

[126] M.S. Cha, P.D. Ronney, Propagation rates of nonpremixed edge flames, *Combustion and Flame*, 146 (2006) 312-328.

[127] N. Peters, Turbulent combustion, Cambridge University Press, 2000.

[128] A.E. Lutz, R.J. Kee, J.F. Grcar, F.M. Rupley, OPPDIF : A Fortran Program for Computing Opposed-flow Diffusion Flames, SAND96-8243 Sandia National Laboratories, (1997).

[129] H. Wang, X. You, A.V. Joshi, S.G. Davis, A. Laskin, F. Eqolfopoulos, C.K. Law, USC Mech Version II. High-Temperature Combustion Reaction Model of H2/CO/C1-C4 Compounds., in, http://ignis.usc.edu/USC_Mech_II.htm, May 2007.

[130] J.S. Chang, A.J. Kelly, J.M. Crowley, Handbook of Electrostatic Processes, Taylor & Francis, 1995.

[131] T.M. Vu, M.S. Cha, B.J. Lee, S.H. Chung, Tip opening of premixed bunsen flames: Extinction with negative stretch and local Karlovitz number, *Combustion and Flame*, 162 (2015) 1614-1621.

PUBLISHED PAPERS and PAPERS IN PREPARATION

1) **D.G. Park**, S.H. Chung, M.S. Cha, Visualization of ionic wind in premixed bunsen flame with DC electric field, *Journal of Visualization*, in preparation to submit.

2) **D.G. Park**, S.H. Chung, M.S. Cha, Dynamic and electric current responses of counterflow nonpremixed flames to AC electric field, *Combustion and Flame*, (2016) in preparation to submit.

3) G.T. Kim, **D.G. Park**, M.S. Cha, J. Park, S.H. Chung, Flow instability in laminar jets driven by AC electric fields, Proceedings of the Combustion Institute, (2016) Accepted.

4) **D.G. Park**, S.H. Chung, M.S. Cha, Bidirectional ionic wind in nonpremixed counterflow flames with DC electric fields, *Combustion and Flame*, (2016) Accepted.

5) Y. Xiong, **D.G. Park**, B.J. Lee, S.H. Chung, M.S. Cha, DC field response of one-dimensional flames using an ionized layer model, *Combustion and Flame*, 163 (2016) 317-325.

6) **D.G. Park**, B.C. Choi, M.S. Cha, S.H. Chung, Soot reduction under DC electric fields in counterflow non-premixed laminar ethylene flame, *Combustion Science and Technology*, 186 (2014) 644-656.

7) Y.H. Chung, **D.G. Park**, J. Park, O.B. Kwon, J.H. Yun, S.I. Keel, Role of the outer-edge flame on flame extinction in nitrogen-diluted non-premixed counterflow flames with finite burner diameters, *Fuel*, 105 (2013) 540-550.